STRUCTURAL AND ELECTROCHEMICAL STUDIES OF SILICON- AND CARBON-BASED MATERIALS FOR LI-ION BATTERY APPLICATIONS

by

Mahdi A. Al-Maghrabi

Submitted in partial fulfilment of the requirements

for the degree of Doctor of Philosophy

at

Dalhousie University

Halifax, Nova Scotia

December 2013

Dedication

To my Father

To my Mother

And to, my beloved son Mohammad and daughter Jana

Table of Contents

List of Tables

List of Figures

Abstract

Four topics are presented in this thesis. Firstly, a new design for a combinatorial electrochemical cell plate based on circuit board technology is described. The new combinatorial cell plate was tested using sputtered silicon and capacity as a function of mass was determined. The measured specific capacity was 3580 mAh/g, which corresponds to $Li_{15}Si_4$ stoichiometry. The irreversible capacity was measured to be less than 2% of the reversible capacity. This design reduced the spurious capacity that came from the lead pattern of the old plate.

Second, the role of oxygen content on the electrochemical properties of sputtered $Si_{1-x}O_x$ was investigated. All the prepared thin film samples had an amorphous or nanostructured nature. The measured specific capacity (first charge) suggests that $Si_{1-x}O_x$ is made up of amorphous silicon that reacts reversibly with lithium, and SiO_2 that forms inactive Li_4SiO_4 after the first lithiation. The current study shows that the irreversible capacity is directly proportional to the oxygen content. This study indicates clearly that in order to produce material with high capacity, oxygen should be minimized to reduce Li consumption during Li_4SiO_4 formation. However, the Si:O ratio should be optimized to get a reasonable active: inactive ratio.

Third, a systematic study to investigate the effect of the addition of carbon on the electrochemical performance of the Sn-Si binary is reported. This study involved the preparation and investigation of three pseudobinary libraries. The addition of carbon was found to inhibit the aggregation of tin and reduce the two-phase coexistence regions as evidenced by smooth differential capacity plots. This was reflected in the improved electrochemical performance such as reversible capacity and cycleability.

Fourth, an investigation of carbon-rich alloys of $Fe_{1-x}C_x$ is reported. Both x-ray diffraction and ^{57}Fe Mössbauer spectroscopy were employed to get insight into the structural properties of this system. X-ray diffraction revealed the amorphous or nanostructured nature of all samples with different Fe:C ratios. The distribution of hyperfine parameters extracted from the Mössbauer analysis shows the existence of two components suggesting that Fe exists in two distinct sites: (1) Fe surrounded with Fe neighbors and (2) Fe surrounded with C neighbors. The asymmetric environment was found more pronounced as carbon content increases in the films. This was reflected by high quadrupole splitting in excess of 1.0 mm/s.

List of Abbreviations Used

AC	alternating current
AFM	atomic force microscopy
Ar	argon gas
c	speed of light
d	interplanar spacing
DEC	diethyl carbonate
δ	isomer and centre shift
Δ	quadrupole splitting
$\mathrm{d}Q/\mathrm{d}V$	differential capacity
e	elementary charge
E_γ	γ-ray transition energy
E_R	recoil energy
EC	ethylene carbonate
EDS	energy-dispersive spectroscopy
EMF	electromotive force
FWHM	full width at half maximum
F	Faraday's constant
λ	wavelength
H	magnetic field
M	metal
M	mass
m	molar mass
ME	Mössbauer effect
n	order of reflection, number of moles
Ni-Mh	nickel-metal hydride
P	pressure
Q	theoretical specific capacity
SEM	scanning electron microscopy

L	crystalline region size
T	temperature
θ	angle
μ	chemical potential
V	potential, volume
v	velocity
XRD	x-ray diffraction
WDS	wavelength-dispersive spectroscopy

Acknowledgment

My supervisor, Dr Richard Dunlap is the person whom I would like to thank first and foremost. I thank him for giving me the opportunity to pursue my graduate studies at Dalhousie University and for his guidance and patience.

Thanks to my committee members. Thanks to Dr Jeff Dahn for his invaluable suggestions and input throughout my research. I am so grateful to Professor Dahn who let me have access to his labs and equipments and above all his time.

Thanks to Dr Harm Rotermund for reading my thesis and great feedback and suggestions.

Many people have helped me throughout the years I have spent at Dalhousie. Special thanks will go to Dr Mark Obrovac, Dr Tim Hatchard, Dr Robbie Sanderson, John Thorne, and all of the Dahn group members

I am so grateful to the Royal Commission for Jubail and Yanbu for their finical support that allows me to pursue my graduate studies.

Unlimited thanks go to my son Mohammad, and my daughter Jana. They provide me with emotional and moral support during the course of my work. All loves go to them

My Dad and Mom: THANK YOU.

Chapter 1:

Introduction

1.1 Background

Modern societies have an ever-increasing demand to develop energy storage devices with high energy and high power density to be used, for example, in portable devices, computing systems, and electric vehicles. Therefore, there are growing initiatives for the development of low-cost, clean energy storage devices. Batteries are electrochemical devices that store electricity in the form of chemical energy. In batteries, the main idea is that electric energy can be obtained from chemical energy through electrochemical oxidation and reduction processes [1].

Batteries can be primary (non-rechargeable) or secondary (rechargeable). In terms of rechargeable batteries, Lithium ion batteries (Li-ion) are the most popular energy storage device and power the vast majority of portable devices such as cell phones and laptops. Li-ion batteries offer numerous advantages over the other available conventional batteries, such as nickel-cadmium (Ni-Cd) and nickel-metal hydride (Ni-MH). These advantages include high energy density, a high operating voltage, long charge-discharge cycle life, low self-discharge rate, no memory effect, and a broad temperature range of operation [2]. However, Li-ion batteries have certain issues including longer charging times, thermal runaway and high cost [3]. A considerable amount of the current research on Li-ion batteries focuses on improving the power and energy density and cycle life. A crucial part of this process is the development of new materials for the negative electrodes.

Silicon (Si) has been extensively studied during the last two decades because of its high theoretical capacity (3578 mAh/g) and appropriate lithiation potential.

Moreover, Si is the second most abundant element on earth and can be found naturally in different forms. However, crystalline Si anodes suffer from capacity fading caused by pulverization resulting from large volume expansion that occurs during Li insertion and extraction [4]. This thesis will focus mainly on Si-based negative electrode materials as possible replacements for graphite.

1.2 Structure and Operation of Li-ion Batteries

The Li-ion battery consists of two or more cells. Depending on the specific application requirement, these cells can be connected in parallel or series, or a combination of these two. Each cell consists of a positive electrode and a negative electrode and these are immersed in an electrolyte, which is composed of Li salts (e.g. $LiPF_6$) dissolved in a mixture of organic solvents (e.g. ethylene carbonate and diethyl carbonate). An electrolyte-permeable separator made from microporous material (e.g. polypropylene) is inserted between the two electrodes to separate them physically and prevent short circuits, while allowing Li ions to pass from one electrode to the other when the external circuit is completed. In 1991, Sony announced a Li-ion battery which was made up of carbonaceous material (coated on copper foil) as a negative electrode and lithium cobalt oxide ($LiCoO_2$) (coated on aluminum foils) as a positive electrode [5]. These batteries operate on the “rocking chair" principle, in which the Li-ions move back and forth between the two electrodes, through the electrolyte, reversibly during charging and discharging [6].

Figure 1.1 depicts a schematic representation of a Li-ion cell showing its main components. During discharge, Li ions are de-intercalated from the negative electrode and migrate through the electrolyte and are intercalated into the positive electrode, as it is more energetically favorable for the Li atoms to be in the positive electrode than in the negative electrode. The movement of Li ions is accompanied by the movement of electrons from the negative electrode to the current collector. These electrons flow through the closed external circuit performing useful work.

The cell can be charged by forcing a current in the opposite direction using an externally applied electromotive force (EMF) across the cell. The voltage of Li-ion cell is related to the difference in the chemical potential of Li atoms at the positive electrode (cathode) and negative electrode (anode) as follows [7]:

$$V_{cell} = -\frac{\left(\mu_{Li}^{cathode} - \mu_{Li}^{anode}\right)}{e} \qquad (1.1)$$

where e is the electronic charge and μ is the chemical potential of a Li atom in the cathode or anode as indicated.

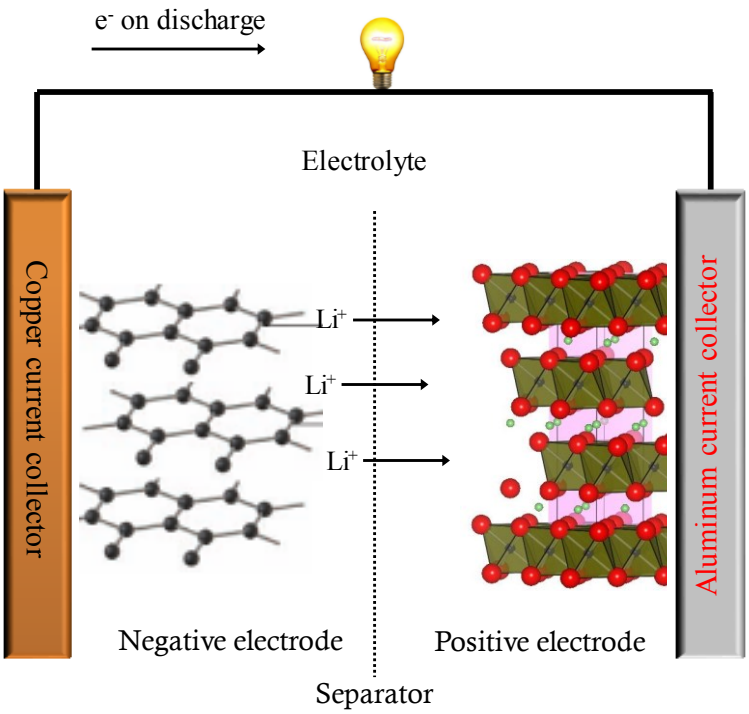

Figure 1.1: A schematic representation of Li-ion cell showing various components. The cell is being discharged [2].

Performance of the negative and positive electrodes is generally given in terms of capacity per unit mass, referred to as gravimetric capacity (mAh/g), or per unit volume, referred to as volumetric capacity (mAh/cc) of the electrode material. The capacity is the total number of ampere-hours that can be delivered by a fully charged electrode under specified conditions of discharge [1]. Developing electrodes with excellent rate capabilities, high capacities, long cycle life, reasonable cost, and safety will enhance the growing market of Li-ion batteries for high power applications.

1.3 Review of Negative Electrode Materials

Li has low density, high reduction potential, and can provide high capacity (3860 mAh/g). These features make Li-based batteries the most compact way for storing electrical energy. In these cells, Li atoms are reversibly inserted between, and extracted from, atomic layers of the positive electrode materials. In 1972 Exxon developed a Li battery based on titanium disulfide (TiS_2) as the positive electrode and Li metal as the negative electrode [8]. Following this, different Li-based rechargeable batteries using Li-metal have appeared [9-12]. However, the early attempts at using Li-metal as the negative electrode were hindered as Li-metal negative electrodes tend to form dendrites after a number of cycles [13-14]. These changes in the surface morphology of Li can puncture the separator and short-circuit the cell. Moreover, at elevated temperature dendrites were found to increase reactivity with the electrolyte solution. As a result of these safety concerns associated with cells containing Li-metal negative electrodes, attempts were made to develop alternative negative electrode materials.

Different trials have been made to replace the metallic Li with insertion materials to be used as a negative electrode. Work by Murphy et al. [12] and Lazzari et al. [6] as an example, led to the so-called “rocking chair” concept. The

reversible intercalation of Li into C and graphite was demonstrated by Besenhard [15].

The first commercial Li-ion battery was released by Sony in 1991 [5]. It had graphite and $LiCoO_2$ as negative and positive electrodes, respectively. Since then, carbon and/or graphite has been employed extensively as a negative electrode material in Li-ion batteries due to their low cost, long cycle life, appropriate voltage, stability, abundance, and excellent conductivity. Li atoms can be intercalated between graphite layers, reaching the stoichiometry LiC_6 corresponding to 372 mAh/g (800 mAh/cc). More details of Li insertion into graphite can be found in reference [16]. Various carbon materials for use in Li-ion batteries were investigated by Dahn et al. [17-18]. Subramanian et al. [19] proposed an amorphous sputtered film of carbon with thickness of 1.1 μm as a potential candidate to deliver high capacities with excellent coulombic efficiencies (987 mAh/g and columbic efficiency of 82%). These features were attributed to the low surface area of the deposited film. However, a slow rate of C/5 was used during their experiment. Generally, the use of C negative electrodes has alleviated the above-mentioned problems associated with using a Li-metal negative electrode. Nevertheless, graphite electrodes have some drawbacks including electrolyte decomposition and irreversible capacity [20], the high cost of artificial graphite, and Li plating on the graphite electrode at a high charging rate, which leads to thermal instability [21]. A C-coating on the surface of graphite was found to reduce the irreversible capacity and hence improve the coulombic efficiency of these electrodes [22]. However, the above mentioned drawbacks of C in addition to the growing demands for higher energy density storage devices have motivated researchers to consider alternatives for graphite.

A $Li_{4/3}Ti_{5/3}O_4$ (LTO) material has been introduced as a negative electrode material, where Li insertion happens via intercalation and de-intercalation. It has a stable structure which yields stable cycling [23]. However, one of the drawbacks of this material is its voltage (1.5V versus. Li/Li^+), which prohibits using this material

in some applications that demand more energy than power [24]. The recent results obtained on LTO are reviewed in reference [25].

Poizot et al. [26] reported electrochemical performance of transition metal oxides as a negative electrode. Following their findings, other metal oxides, including iron oxide [27-29], cobalt oxide [30-31], and nickel oxide [32-33], were considered. However, these oxides have high average potentials, which in turn limits their use in high-energy density applications.

It has been demonstrated that at room temperature Li reacts reversibly with different metals such as aluminum (Al), zinc (Zn), tin (Sn), platinum (Pt), and antimony (Sb) [35] where this alloying process occurs according to:

$$x\mathrm{Li}^{+} + x\mathrm{e}^{-} + \mathrm{M} \Leftrightarrow \mathrm{Li}_x\mathrm{M} \qquad (1.2)$$

Table 1.1 gives the specific capacities (gravimetric and volumetric) of several active materials [36]. The most interesting features of these metals are (i) high theoretical capacity and (ii) moderate redox potential versus Li. The latter feature reduces the safety concern with Li deposition that occurs with graphite and also contributes to the overall cell voltage and the energy density.

Table 1.1: Theoretical room-temperature capacities of some elements that can react with Li reversibly [36]. Volumetric capacity (lithiated) refers to the volumetric capacity of the most lithiated phases as given in the table.

Element	Gravimetric capacity	Volumetric capacity	Volumetric capacity (Lithiated)	Lithiated phase
Si	3580 mAh/g	8483 mAh/cc	2300 mAh/cc	$Li_{15}Si_4$
Sn	992 mAh/g	7200 mAh/cc	2100 mAh/cc	$Li_{22}Sn_5$
Al	992 mAh/g	2680 mAh/cc	1400 mAh/cc	LiAl
Bi	385 mAh/g	3773 mAh/cc	1650 mAh/cc	Li_3Bi

In 1975, Antula et al. [37] reported that as Li alloys with Si, an intermetallic phase is formed. Sharma and Seefurth [38] reported the formation of Li–Si alloys at high temperature (400–500˚C). Later, in 1981, Boukamp et al. [4] observed different phases of Li-Si in good agreement with the Li-Si equilibrium phase diagram that shows multiple Li-Si phases [39].

At room temperature, it has been reported that crystalline Si becomes amorphous during the lithiation process [40]. This phenomenon was confirmed by an *in situ* x-ray experiment which shows a decrease and disappearance of the crystalline Si peaks during the first Li insertion [41]. However, as the highly lithiated amorphous Si is discharged below 50 mV versus Li, crystalline $Li_{15}Si_4$ is formed rather than $Li_{22}Si_5$ ($Li_{15}Si_4$ phase is not in the equilibrium phase diagram, however) [42]. This phase offers a theoretical capacity of 3580 mAh/g, in agreement with most of the literature ([43] as an example). During charge, the $Li_{15}Si_4$ crystalline phase is converted into amorphous Si in addition to the crystalline phase. This is reflected as a broad peak in the differential capacity plots indicating the existence of two-phase regions. Interestingly, the lithiated Si becomes amorphous after the first charge [41, 42]. The formation of the $Li_{15}Si_4$ phase was confirmed using an *in situ* x-ray diffraction experiment by Hatchard and Dahn [44]. Obrovac and Christensen [42] reported the effect of the lower cut-off potential on the formation of the $Li_{15}Si_4$ crystalline phase. They found that a cell discharged to 0.0 V showed a change of slope of the voltage curve that indicated the existence of a two-phase region during charging. This two-phase region was not observed in the voltage curve for samples that cycled above 50 mV.

It has been demonstrated that the insertion and extraction of Li ions in the pure crystalline Si is not structurally benign [36] and up to a 280% volume change can occur as Si is lithiated. As Si is lithiated and one crystalline phase is converted to another, stress takes place at the boundaries between these phases. These stresses

can pulverize the active particles and cause loss of electrical contact among the particles, causing capacity fade and low Coulombic efficiency during the first cycle. Therefore, during the last two decades there has been extensive research to address the volume expansion and capacity fade of Si and Si-based negative electrode. Several approaches have been exploited to suppress the volume expansion; one is to make a composite which consists of active Si particles that are dispersed in an electrochemically inert or relatively inactive matrix. One role of the inactive matrix is to withstand the stresses resulting from volume expansion which enhances the mechanical stability of the electrode material. The other role of the inactive matrix is to inhibit the aggregation and clustering of the active particles [45]. The matrix, however, must possess good ionic and electronic conductivity. The matrix can be a metal or alloy [46] or an oxide such as Li_2O [47]. The active-inactive concept was introduced by Huggins [48] and Yang et al. [49], which was followed by the production of a negative electrode based on tin-based convertible oxides by the Fuji Company [50]. An irreversible capacity, as high as 50%, was observed after the first cycle [51]. Lithiation of tin oxide composites was further investigated by Courtney et al. [52] by *in situ* x-ray diffraction experiments. They found that as SnO_2 is lithiated, Sn and Li_2O are formed. However, the Li that is consumed to form Li_2O cannot be recovered, which explains the origin of the irreversible capacity. Mao et al. [45] reported the effect of small grain size on the electrochemical performance of a Sn-based composite anode. One potential drawback of the inactive matrix is the possibility of slowing down the diffusion of Li ions or electron transfer resulting in a lower capacity than that expected theoretically [53] and this imposes constraints on the selection of the inactive element. Todd et al. [54] surveyed different transition metals with Sn using sputtering. They showed that amorphous or nanostructured samples have superior electrochemical performance compared to the crystalline samples. Based on an active-inactive approach, Sony commercialized the Sn-Co-C negative electrode in 2006.

Along the lines of the active-inactive approach, SiO was also investigated as a potential negative electrode material. When SiO is lithiated in the first cycle, Li_2O and other different silicates such as Li_4SiO_4 are formed in addition to the active Si particles that can reversibly react with Li. Both Li_2O and Li_4SiO_4 work to buffer the volume expansion that occurs [55]. Kim and co-worker employed the active-inactive concept and achieved stable reversible capacities for amorphous Si particles that were dispersed in the nanocrystalline matrices of TiB_2 [56] and TiN [56] and C [57].

The positive impact of carbon addition has been reported [58]. The improved performance of $Ni_{20}Si_{80}$ alloys was attributed to the enhancement of both the ionic and electronic conductivity and the buffering effect of the carbon matrix. Higher carbon content improves the cycleability but on the other hand reduces the overall specific capacity and increases the irreversible capacity [59].

Reducing the active particle size which is dispersed within an inactive matrix has also shown improved cycling performance [60]. A ball-milled SnSb/C composite has shown good cycleability up to 300 cycles [22]. In spite of the improved performance of nanosized particles, they have several drawbacks including large surface area, expensive production, and difficulty in handling.

Another possible approach that was employed to minimize the drawback of volume expansion of Si is the use of amorphous Si thin film. The Dahn group demonstrated the advantage of using amorphous alloys as negative electrode materials. A study reported by Beaulieu et al. [61] has shown that amorphous thin films of Si-Sn alloys expand and contracted homogenously and reversibly with less pulverization and better cycling. A similar observation was reported by Maranchi et al. [62]. The interesting results reported by Beaulieu et al. [61], motivated different research groups to initiate studies of similar amorphous Si-based materials. A reversible capacity of about 1700 mAh/g was reported by Graetz et al. [63] for amorphous Si thin films deposited on a Cu substrate. The effect of thickness of thin films on the electrochemical performance was reported by Maranchi et al. [62]. It

was found that the cycleability of amorphous Si films decreases considerably as a function of the film thickness. These results were confirmed by the finding of Hatchard and Dahn [44]. Beaulieu et al. [61] reported reversible volume changes in sputtered Si-Sn films [64] and provided insight into the nature of the electrochemical reaction of Li with sputtered amorphous Si-Sn films [65,66]. The behavior of amorphous Si thin films deposited on a Cu substrate using the magnetron sputtering technique was reported [67]. Electrodes exhibited a high reversible capacity of 3134 mAh/g. The improved performance of the Si thin film was attributed to the adhesion strength between the Si thin film and the Cu foil. Hatchard et al. [68] have shown that amorphous sputtered thin films of $Si_{1-x-y}Al_xSn_y$ have superior electrochemical performance compared with similar crystalline samples.

1.4 Motivation of the Thesis

Li-ion batteries have been used successfully in numerous consumer electronic devices. The huge interest in utilizing Li-ion batteries in electric vehicles has led to research and development of a new generation of these batteries to meet the demand for higher energy and higher power.

The present work has been motivated by the high gravimetric and volumetric capacity that is exhibited by Si compared with other potential anode materials. However, the large capacity fade observed during the first few cycles has been considered a problem until this point in time. It is the main target of this study to minimize such volume changes upon cycling by synthesizing materials of an amorphous or nanostructured nature.

The promising electrochemical performance of amorphous or nanostructured material, in particular, for use as a negative electrode in Li-ion batteries has motivated the current project. Moreover, the interesting features of sputtered films have promoted the use of the combinatorial sputtering method to produce all the

samples in this project. This is a very powerful technique to search for new battery electrode materials as a large range of compositions can be produced simultaneously. The production of samples by this technique requires combinatorial testing techniques, so the first stage of this project was aimed at designing a new combinatorial cell plate to replace the conventional combinatorial cell plate. This objective was accomplished and is presented in Chapter 3.

Chapter 4 is devoted to a discussion of results on the $Si_{1-x}O_x$ system. This is a particularly attractive system from a cost standpoint.

Although Li-Si and Li-Sn alloys offer high theoretical capacity, they suffer from poor cycleability due to their volume changes. We chose to study the effect of C addition on the structural and electrochemical features of the Sn-Si binary. The selection of C was based on its good electrical conductivity and numerous previous reports of the potentially advantageous effects of carbon additions [69]. The results of the combinatorial investigations of the Sn-Si-C system undertaken during this thesis work are presented in Chapter 5.

The advantages of electrode materials that exhibit an amorphous or nanostructured nature is well known. However, experimental techniques such as x-ray diffraction are often limited in their ability to provide meaningful information about materials with such microstructures. Throughout the investigations presented in this thesis, the Mössbauer effect method has been employed because of its particular sensitivity to the local structure of disordered materials. Chapter 6 presents combinatorial Mössbauer effect studies of Fe–C in the C-rich portion of the phase diagram. This system is of particular interest for two reasons; (1) Fe is the most common and useful Mössbauer probe and (2) as indicated above, the addition of carbon to nanostructured electrode materials is often beneficial to their performance. However, to our knowledge there has been no Mössbauer effect studies of the C-rich portion of the Fe-C phase diagram reported previously. Thus, the present investigation has been motivated by the need for an understanding of the Mössbauer parameters of C-rich Fe–C alloys for the purpose of better interpreting

previous studies of Fe–C containing alloys [45] or new investigations which may follow from the results presented here as proposed in Chapter 7 of this thesis.

1.5 References

[1] T. Reddy and D. Linden, “Linden's Handbook of Batteries”, McGraw-Hill, New York (2011).

[2] M. Yoshio, R. Brodd, and A. Kozawa, “Lithium-ion Batteries Science and Technologies”, Springer, New York (2009).

[3] Z. Zhang and P. Ramadass, “Lithium-ion Battery Systems and Technology. Batteries for Sustainability”, Springer, Hoboken (2013).

[4] B. Boukamp, G. Lesh, and R. Huggins, “All−solid lithium electrodes with mixed−conductor matrix”, *J. Electrochem. Soc*. **128** (1981) 725-729.

[5] T. Nagaura and K. Tozawa, “Lithium ion rechargeable battery”, *Prog. Batteries Solar Cells* **9** (1990) 209-214.

[6] M. Lazzari and B. Scrosati, “A cyclable lithium organic electrolyte cell based on two intercalation electrodes*”, J. Electrochem. Soc*. **127** (1980) 773-774.

[7] M. Wakihara and O. Yamamoto, “Lithium ion batteries”, John Wiley & Sons, New York (2008).

[8] M. Whittingham, “Electrical energy storage and intercalation chemistry”, *Science* **192** (1976) 1126-1127.

[9] K. Brandt, “A 65 Ah rechargeable lithium molybdenum disulfide battery”, *J. Power Sources* **18** (1986) 117-125.

[10] D. Wilkinson, H. Blom, K. Brandt, and D. Wainwright, “Effects of physical constraints on Li cycleability”, *J. Power Sources* **36** (1991) 517-527.

[11] D. Fouchard and J. Taylor, “The molicel rechargeable lithium system: Multicell aspects”, *J. Power Sources* **21** (1987) 195-205.

[12] D. Murphy, F. Di Salvo, J. Carides, and J. Waszczak, “Topochemical reactions of rutile related structures with lithium”, *Mater. Res. Bull*. **13** (1978) 1395-1402.

[13] N. Goldenfeld, “Dynamics of dendritic growth”, *J. Power Sources* **26** (1989) 121-128.

[14] U. von Sacken, E. Nodwell, A. Sundher, and J. Dahn, "Comparative thermal stability of carbon intercalation anodes and lithium metal anodes for rechargeable lithium batteries", *J. Power Sources* **54** (1995) 240-245.

[15] J. Besenhard and H. Fritz, "Reversible electrochemical alloying of metals of main group V in organic Li^+-solutions", *Electrochim. Acta.* **20** (1975) 513-517.

[16] J. Dahn, "Phase diagram of Li_xC_6", *Physical Review B* **44** (1991) 9170-9177.

[17] J. Dahn, A. Sleigh, H. Shi, J. Reimers, Q. Zhong, and B. Way, "Dependence of the electrochemical intercalation of lithium in carbons on the crystal structure of the carbon", *Electrochim. Acta.* **38** (1993) 1179-1191.

[18] J. Dahn, T. Zheng, Y. Liu, and J. Xue, "Mechanisms for lithium insertion in carbonaceous materials", *Science* (1995) 590-593.

[19] V. Subramanian, T. Karabacak, C. Masarapu, R. Teki, T. Lu, and B. Wei, "Low hydrogen containing amorphous carbon films-Growth and electrochemical properties as lithium battery anodes", *J. Power Sources* **195** (2010) 2044-2049.

[20] J. Kim, W. Yoon, K. Yoo, G. Park, C. Lee, Y. Murakami, and D. Shindo, "Charge–discharge properties of surface-modified carbon by resin coating in Li-ion battery", *J. Power Sources* **104** (2002) 175-180.

[21] W. Lu, C. López, N. Liu, J. Vaughey, and A. Jansen,"Overcharge effect on morphology and structure of carbon electrodes for lithium-ion batteries", *J. Electrochem. Soc*. **159** (2012) A566-A570.

[22] Y. Park, H. Bang, S. Oh, Y. Sun, and S. Lee, "Effect of carbon coating on thermal stability of natural graphite spheres used as anode materials in lithium-ion batteries", *J. Power Sources* **190** (2009) 553-557.

[23] K. Zaghib, M. Dontigny, A. Guerfi, P. Charest, I. Rodrigues, A. Mauger, and C. Julien, "Safe and fast-charging Li-ion battery with long shelf life for power applications", *J. Power Sources* **196** (2011) 3949-3954.

[24] Y. Tang, L. Yang, Z. Qiu, and J. Huang, "Template-free synthesis of mesoporous spinel lithium titanate microspheres and their application in high-rate lithium ion batteries", *Journal of Materials Chemistry* **19** (2009) 5980-5984.

[25] K. Zaghib, A. Mauger, H. Groult, J. Goodenough, and C. Julien, "Advanced electrodes for high power Li-ion batteries", *Materials* **6** (2013) 1028-1049.

[26] P. Poizot, S. Laruelle, S. Grugeon, L. Dupont, and J. Tarascon, "Nano-sized transition-metal oxides as negative-electrode materials for lithium-ion batteries", *Nature* **407** (2000) 496-499.

[27] P. Taberna, S. Mitra, P. Poizot, P. Simon, and J. Tarascon, "High rate capabilities Fe_3O_4-based Cu nano-architectured electrodes for lithium-ion battery applications", *Nature Materials* **5** (2006) 567-573.

[28] J. Liu, Y. Li, H. Fan, Z. Zhu, J. Jiang, R. Ding, Y. Hu, and X. Huang, "Iron oxide-based nanotube arrays derived from sacrificial template-accelerated hydrolysis: Large-area design and reversible lithium storage", *Chemistry of Materials* **22** (2009) 212-217.

[29] M. Zhang, D. Lei, X. Yin, L. Chen, Q. Li, Y. Wang, and T. Wang, "Magnetite/graphene composites: Microwave irradiation synthesis and enhanced cycling and rate performances for lithium ion batteries", *J.Mater. Chem.* **20** (2010) 5538-5543.

[30] X. Lou, D. Deng, J. Lee, and L. Archer, "Thermal formation of mesoporous single-crystal Co_3O_4 nano-needles and their lithium storage properties", *Journal of Materials. Chemistry* **18** (2008) 4397-4401.

[31] B. Yu, J. Lee, J. Song, C. Park, C. Lee, and H. Sohn, "Nanostructured cobalt oxide-based composites for rechargeable Li-ion batteries", *Journal of Solid State Electrochemistry* **16** (2012) 2631-2638.

[32] X. Huang, J. Tu, X. Xia, X. Wang, J. Xiang, L. Zhang, and Y. Zhou, "Morphology effect on the electrochemical performance of NiO films as anodes for lithium ion batteries", *J. Power Sources*. **188** (2009) 588-591.

[33] M. Cheng and B. Hwang, "Mesoporous carbon-encapsulated NiO nanocomposite negative electrode materials for high-rate Li-ion battery", *J. Power Sources* **195** (2010) 4977-4983.

[34] M. Wuand Y. Lin, "Monodispersed macroporous architecture of nickel-oxide film as an anode material for thin-film lithium-ion batteries", *Electrochim. Acta*. **56** (2011) 2068-2073.

[35] A. Dey, "Electrochemical alloying of lithium in organic electrolytes", *J. Electrochem. Soc.* **118** (1971) 1547-1549.

[36] M. Winter and J. Besenhard, "Electrochemical lithiation of tin and tin-based intermetallics and composites", *Electrochim. Acta.* **45** (1999) 31-50.

[37] J. Antula and B. Becker, "Investigation of the cathodic reduction of lithium and arsenic ions on monocrystalline silicon by cyclic voltammetry", *J.Phys. Chem*. **79** (1975) 2470-2473.

[38] R. Sharma and R. Seefurth, "Thermodynamic properties of the Lithium-Silicon system", *J. Electrochem. Soc*. **123** (1976) 1763-1768.

[39] T. Massalski, H. Okamoto, P. Subramanian, and L. Kacprzak, "Binary alloy phase diagrams", ASM International, 1990.

[40] P. Limthongkul, Y. Jang, N. Dudney, and Y. Chiang, "Electrochemically-driven solid-state amorphization in lithium-silicon alloys and implications for lithium storage", *Acta. Materialia*. **51** (2003) 1103-1113.

[41] J. Li and J. Dahn, "An *in situ* x-ray diffraction study of the reaction of Li with crystalline Si", *J. Electrochem. Soc*. **154** (2007) A156-A161.

[42] M. Obrovac and L. Christensen, "Structural changes in silicon anodes during lithium insertion/extraction", *Electrochemical and Solid-State Letters* **7** (2004) A93-A96.

[43] M. Al-Maghrabi, N. van der Bosch, R. Sanderson, D. Stevens, R. Dunlap, and J. Dahn, "A new design for a combinatorial electrochemical cell plate and the inherent irreversible capacity of lithiated silicon", *Electrochemical and Solid-State Letters* **14** (2011) A42-A44.

[44] T. Hatchard and J. Dahn, "*In situ* XRD and electrochemical study of the reaction of lithium with amorphous silicon", *J. Electrochem. Soc.* **151** (2004) A838-A842.

[45] O. Mao, R. Turner, I. Courtney, B. Fredericksen, M. Buckett, L. Krause, and J. Dahn, "Active/Inactive nanocomposites as anodes for Li-Ion batteries", *Electrochemical and Solid-State Letters* **2** (1999) 3-5.

[46] T. Li, Y. Cao, X. Ai, and H. Yang, "Cycleable graphite/$FeSi_6$ alloy composite as a high capacity anode material for Li-ion batteries", *J. Power Sources* **184** (2008) 473-476.

[47] Y. Liu, Z. Wen, X. Wang, X. Yang, A. Hirano, N. Imanishi, and Y. Takeda, "Improvement of cycling stability of Si anode by mechanochemcial reduction and carbon coating", *J. Power Sources* **189** (2009) 480-484.

[48] R. Huggins, "Materials science principles related to alloys of potential use in rechargeable lithium cells", *J. Power Sources* **26** (1989) 109-120.

[49] J. Yang, M. Winter, and J. Besenhard, "Small particle size multiphase Li-alloy anodes for lithium-ion batteries", *Solid State Ionics* **90** (1996) 281-287.

[50] Y. Idota, T. Kubota, A. Matsufuji, Y. Maekawa, and T. Miyasaka, "Tin-based amorphous oxide: A high-capacity lithium-ion-storage material", *Science* **276** (1997) 1395-1397.

[51] R. Huggins, "Lithium alloy negative electrodes", *J.Power Sources* **81** (1999) 13-19.

[52] I. Courtney and J. Dahn, "Electrochemical and *in situ* x−ray diffraction studies of the reaction of lithium with tin oxide composites", *J. Electrochem. Soc*. **144** (1997) 2045-2052.

[53] M. Fleischauer, M. Obrovac, J. McGraw, R. Dunlap, J. Topple, and J. Dahn, "Al-M (M= Cr, Fe, Mn, Ni) thin-film negative electrode materials", *J. Electrochem. Soc.* **153** (2006) A484-A491.

[54] A. Todd, R. Mar, and J. Dahn, "Tin–transition metal–carbon systems for lithium-ion battery negative electrodes", *J. Electrochem. Soc*. **154** (2007) A597-A604.

[55] H. Takezawa, K. Iwamoto, S. Ito, and H. Yoshizawa, "Electrochemical behaviors of nonstoichiometric silicon suboxides (SiO_x) film prepared by reactive evaporation for lithium rechargeable batteries", *J. Power Sources* **244** (2013) 149-157

[56] I. Kim, G. Blomgren, and P. Kumta, "Nanostructured Si/TiB_2 composite anodes for Li-ion batteries", *Electrochemical and Solid-State Letters* **6** (2003) A157-A161.

[57] P. Patel, I. Kim, and P. Kumta, "Nanocomposites of silicon/titanium carbide synthesized using high-energy mechanical milling for use as anodes in lithium-ion batteries", *Materials Science and Engineering: B* **116** (2005) 347-352.

[58] H. Lee, Y. Kim, M. Hong, and S. Lee, "Carbon-coated $Ni_{20}Si_{80}$ alloy–graphite composite as an anode material for lithium-ion batteries", *J. Power Sources* **141** (2005) 159-162.

[59] J. Saint, M. Morcrette, D. Larcher, L. Laffont, S. Beattie, J. Pérès, D. Talaga, M. Couzi, and J. Tarascon, "Towards a fundamental understanding of the improved electrochemical performance of silicon–carbon composites", *Advanced Functional Materials* **17** (2007) 1765-1774.

[60] Q. Si, K. Hanai, N. Imanishi, M. Kubo, A. Hirano, Y. Takeda, and O. Yamamoto, "Highly reversible carbon–nano-silicon composite anodes for lithium rechargeable batteries", *J. Power Sources* **189** (2009) 761-765.

[61] L. Beaulieu, T. Hatchard, A. Bonakdarpour, M. Fleischauer, and J. Dahn, "Reaction of Li with alloy thin films studied by in situ AFM", *J. Electrochem. Soc.* **150** (2003) A1457-A1464.

[62] J. Maranchi, A. Hepp, and P. Kumta, "High capacity, reversible silicon thin-film anodes for lithium-ion batteries", *Electrochemical and Solid-State Letters* **6** (2003) A198-A201.

[63] J. Graetz, C. Ahn, R. Yazami, and B. Fultz, "Highly reversible lithium storage in nanostructured silicon", *Electrochemical and Solid-State Letters* **6** (2003) A194-A197.

[64] L. Beaulieu, K. Eberman, R. Turner, L. Krause, and J. Dahn, "Colossal reversible volume changes in lithium alloys", *Electrochemical and Solid-State Letters* **4** (2001) A137-A140.

[65] L. Beaulieu, K. Hewitt, R. Turner, A. Bonakdarpour, A. Abdo, L. Christensen, K. Eberman, L. Krause, and J. Dahn, "The electrochemical reaction of Li with amorphous Si-Sn alloys", *J. Electrochem. Soc*. **150** (2003) A149-A156.

[66] J. Li, A. Smith, R. Sanderson, T. Hatchard, R. Dunlap, and J. Dahn, "*In situ* ^{119}Sn Mossbauer effect study of the reaction of lithium with Si using a Sn probe*", J. Electrochem. Soc*. (2009) A283-290.

[67] L. Chen, J. Xie, H. Yu, and T. Wang, "An amorphous Si thin film anode with high capacity and long cycling life for lithium ion batteries", *J. Appl. Electrochem*. **39** (2009) 1157-1162.

[68] T. Hatchard, J. Topple, M. Fleischauer, and J. Dahn, "Electrochemical performance of SiAlSn films prepared by combinatorial sputtering", *Electrochemical and Solid-State Letters.***6** (2003) A129-A132.

[69] J. Thorne, R. Sanderson, J. Dahn, and R. Dunlap, "Combinatorial study of the Sn–Cu–C system for Li-ion battery negative electrode materials", *J. Electrochem. Soc.* **157** (2010) A1085-A1091.

Chapter 2:

Experimental Techniques

2.1 Combinatorial Materials Science Methods

2.1.1 Background

Over the last few decades there has been a huge interest in the development of advanced materials for technological applications. Traditionally, in order to discover new materials the researcher would produce and test samples on a one-by-one basis. Such an approach is time-consuming and provided motivation for the development of more efficient production and characterization processes. High-throughput experiments allow the synthesis and characterization of large arrays of different materials simultaneously, leading to the identification of promising materials. The extensive use of combinatorial techniques was first adapted in pharmaceutical research [1-2]. In materials research, combinatorial techniques were presented by Kennedy et al. [3] in 1965. In 1970, Hanak [4] used the sputtering method to prepare a composition-spread of metal alloys. Despite some early success using the combinatorial method, this approach was hindered by the lack of appropriate complementary tools, such as rapid characterization methods.

In the 1990's, Xiang et al. [5] used the combinatorial method in materials science. Using a sputtering method, they produced thin films of cuprate superconductors. The sputtered compositions were obtained using a shadow masks. Since then combinatorial methods have been used to search for a wide range of materials in different fields. In 1998, the application of the combinatorial method in electrochemical research was reported by Reddington et al. [6].

The first application of the combinatorial method in Li-ion battery research was introduced by Yanase et al. [7]. This method was further developed here at Dalhousie University by Dahn et al. [8] who used combinatorial sputtering to produce films in ternary systems. The power of such an approach is that it allows for both linear and orthogonal gradient deposition on different kinds of substrates using a modified multi-target sputtering machine [8]. Since then, both negative [9] and positive [10] electrode materials for Li-ion batteries have been studied.

2.1.2 Sputter Deposition

The ejection of atoms from the surface of a material by bombardment with energetic particles is called sputtering. The energetic particles are usually ions of gaseous materials, typically argon (Ar). Figure 2.1 shows a schematic representation of a typical sputtering system. In general, a sputtering system consists of: (a) a vacuum chamber, (b) the substrate which serves as the anode and is kept at a high positive potential, and (c) the target which serves as the cathode and is kept at a high negative potential. When the potential between the anode and the cathode exceeds a certain value, a glow discharge is produced and the argon becomes ionized. The ionized species in the glow discharge are accelerated under the applied electric field. The positive ions then bombard the negatively charged target and can eject some atoms from the target upon collision.

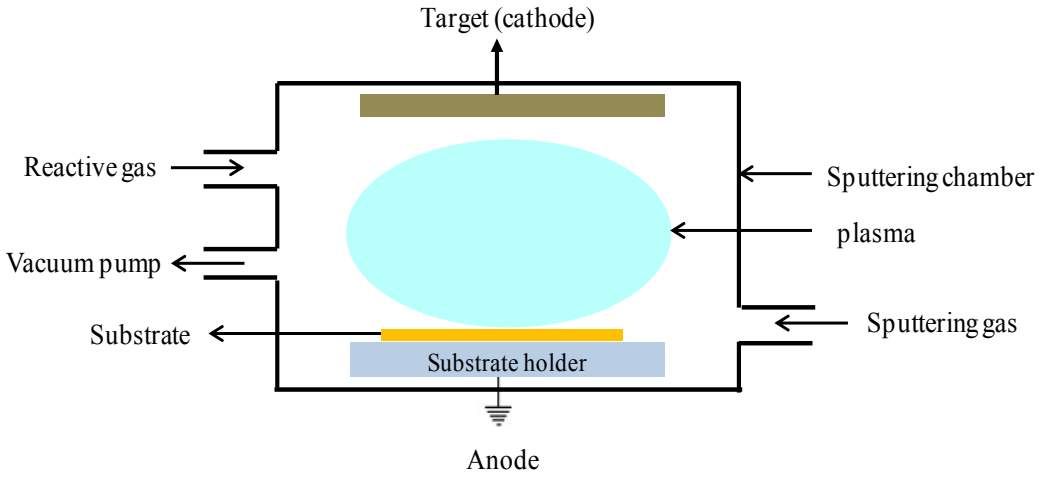

Figure 2.1: Basic components of sputtering system [12].

These ejected atoms deposit onto the substrate to form the desired thin film. This type of sputtering is called "DC sputtering" and it is suitable for conductors and semiconductors. If the target is a non-conducting material the positive charge will build up on the material and it will stop sputtering. However, if the polarity of the target is reversed to attract enough electrons from the plasma to eliminate the surface charge, sputtering may proceed. This is done by applying a radio-frequency (RF) AC voltage to the target. This type of sputtering is known as "RF sputtering". Some sputtering systems incorporate magnets near the target to increase the number of collisions of charged particles in the plasma and allow for plasma formation at lower pressures; thereby effectively increasing the sputtering rate. These magnets produce a magnetic field which cause the secondary electrons ejected from the target to follow a spiral path so that they have a greater chance of colliding with more gas atoms and creating new ions during their travel. This type of sputtering is called "magnetron sputtering" and can be used with DC or RF sputtering. This is the sputtering technique used to produce samples in the present thesis and is described in the next section. Additional information on these sputtering methods can be found in references [11-12], for example.

2.1.3 Description of the Sputtering Apparatus

All thin film libraries described in this thesis were produced using DC and/or RF magnetron sputtering in a Corona Vacuum Coater model V-3T multi-target system. Details of the sputtering system are presented in reference [8]. Figure 2.2 is a photograph of the sputtering chamber showing the various components. The sputtering chamber is 80 cm in diameter and its depth is 30 cm. A Varian 500 L/s turbo pump, backed by a roughing pump, is used to evacuate the chamber. A Polycold PFC-400 cryopump is integrated within the sputtering machine to remove the residual moisture from the sputtering chamber and a base pressure of approximately 1×10^{-7} Torr can be reached. The substrate table is water-cooled and can be rotated. Up to five targets can be used in the system. The five magnetrons each use a pair of 6 mm thick Nd-Fe-B magnets and are separated by 60^{o}; they are water-cooled to prevent the possibility of target material phase change or demagnetization of the magnets. In order to obtain the desired range of compositions, different stationary masks can be placed over the targets. Figure 2.2 shows also, as an example, masks producing a “linear in” deposition profile and a “constant” deposition profile. The angular velocity of the sputtering table as it rotated in front of the targets was 14 rpm to ensure atomic level mixing. Sputtering rate and angular velocity of the sputtering table were chosen in order to deposit a monatomic-thick layer in each rotation.

Continuous films on a 76 mm wide sputter track were deposited onto a variety of substrates. In order to clean the substrates, prior to deposition, all substrates were first exposed to oxygen plasma and then to argon plasma for 15 minutes each. Figure 2.3 shows a typical layout of the sputtering table for binary and pseudobinary runs. A variety of substrates were used. In the pseudobinary libraries, eleven pre-weighed Cu foil disks were used for mass determination, a Cu-coated glass slide for composition analysis, a Si (100) wafer for x-ray diffraction measurement, and kapton foils for Mössbauer measurements, if applicable, were

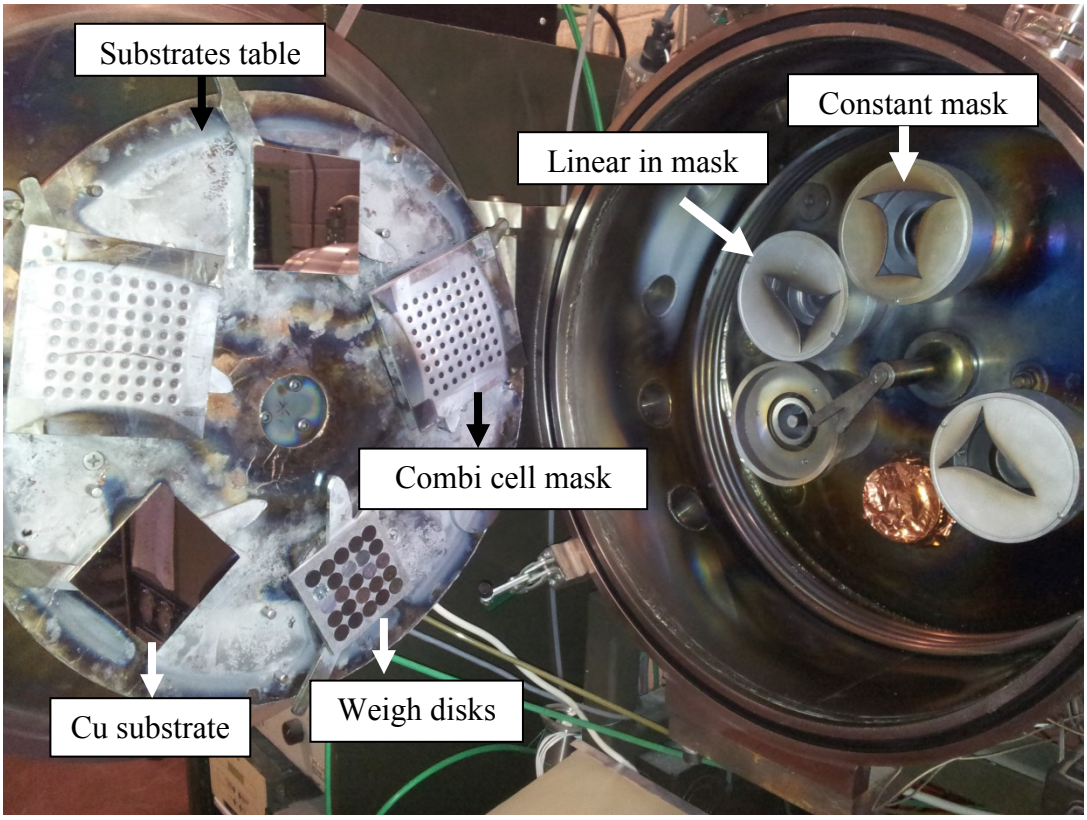

Figure 2.2: Photograph of sputtering chamber showing various components.

used. The stoichiometry of the sputtered elements on substrates varied linearly with position.

In order to produce a ternary library, a rotating table as shown in Figure 2.2, which has five sub-tables, was used. The five sub-tables were used to mount different types of substrates: a square array of 25 pre-weighted Cu foil disks to determine mass per unit area as a function of position on the sub-table, a 3 × 3 inch Cu coated glass for microprobe analysis, and a 3 × 3 inch Si wafer for x-ray diffraction. The stoichiometry of the sputtered elements on different substrates varied linearly and in an orthogonal manner with position. The ternary run was characterized using an 8 by 8 grids of points. In both pseudobinary and ternary runs, thin films libraries were also deposited on a combinatorial cell plate based on a

printed circuit board. More details about these cell plates will be presented in Chapter 3. In order to ensure the reproducibility in the electrochemical data, two or three combinatorial cell plates were produced in each sputtering run.

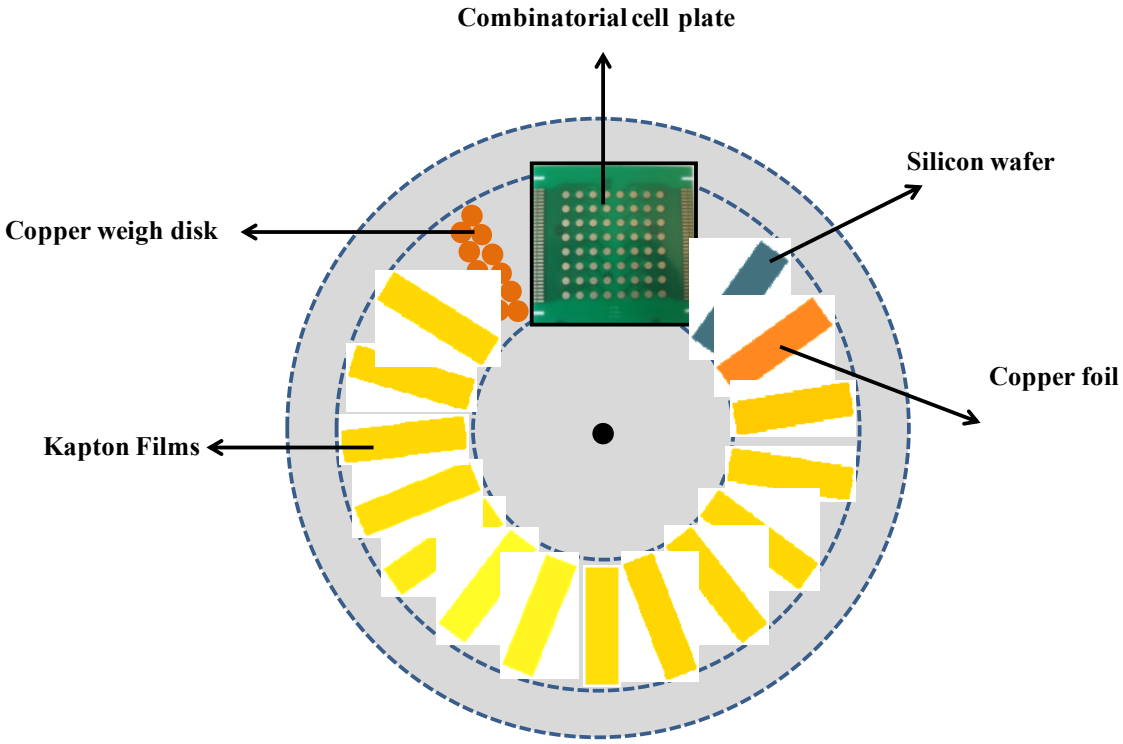

Figure 2.3: Typical layout of the sputtering table showing different substrates that are used in a binary sputtering run.

2.2 Compositional and Mass Determination

2.2.1 Microprobe Analysis

The chemical compositions of all the libraries prepared in this thesis were determined using a JEOL-8200 Superprobe electron microprobe for energy or wavelength dispersive spectroscopy (EDS and WDS, respectively). The machine is equipped with five wavelength dispersive spectrometers. A programmable stage is used to move to specific points in a line or grid. The basic principle of electron microprobe spectroscopy will be presented here and a detailed discussion can be found in different sources such as [13]. A high energy electron beam bombards the sample to be investigated, liberating inner shell electrons, leaving the atoms in excited states. As a result, the atom will decay by the transition of outer shell electrons to fill the vacancy created by those ejected electrons, and x-rays, with well-defined wavelengths, are emitted in this process. Each atom has characteristic x-ray energies that allow for its identification. The polychromatic x-rays from the sample are focused on a diffractor crystal of known lattice spacing, *d,* that is rotating over a range of incident angles θ to scan a broad range of wavelengths and are then incident on a detector. The intensities of the x-rays are compared to those produced from standards of known composition. The relative proportion of elements in the sample is determined based on the relative intensities of the energy peaks.

$$\frac{C^i_{sample}}{C^i_{std.}} = (ZAF)^i \frac{I^i_{sample}}{I^i_{std.}} = (ZAF)^i k^i \qquad (2.1)$$

C^i_{sample} and $C^i_{std.}$ are the mass percent of element *i* in the sample and the standard, respectively. I^i_{sample} and I^i_{std} are the intensity of the characteristic x-ray of element *i* in the sample and the standard, respectively. *ZAF* is a correction factor applied to

account for differences in the intensities of the sample and standard. *ZAF* is referred to as a matrix correction because it compensates for the distinct chemical environment of element *i* in the sample and the standard. This factor includes corrections for: (1) differences in atomic number [*Z*], (2) absorption [*A*], and (3) fluorescence [*F*]. Although the *ZAF* corrections are often effective, using standards similar, in composition, to the sample under study is desirable.

The x-rays emitted from the sample during the electron microprobe experiment can be analyzed by two different methods: (1) energy dispersive spectroscopy (EDS) and (2) wavelength dispersive spectroscopy (WDS). In the first method, a Si-drift detector (SDD) detects x-rays through the generation of electron-hole pairs, where the number of pairs is proportional to the energy per photon of the x-ray. These pairs are converted to a voltage pulse, which is proportional to the energy of the incident photon. In this method collecting the x-rays from all elements occurs almost simultaneously allowing for a rapid measurement. However, the energy resolution of EDS is less than WDS. In the WDS method, wavelengths are measured. To accomplish this, a crystal with atomic spacing *d* is positioned in the spectrometer so that the Bragg condition is satisfied:

$$n\lambda = 2d\sin\theta \qquad (2.2)$$

where *n* is an integer, λ is the wavelength, and θ is scattering angle. Measurement of different wavelengths can be determined by rotating the crystal and moving the detector relative to both the sample and the diffractor crystal. Prior to each experiment, the detectors were calibrated for the appropriate elements to ensure accuracy in the measurement.

2.2.2 Mass Determination

In order to determine the specific capacity of the prepared electrodes, the mass must be known. In each sputtering experiment, Cu weigh disks with a diameter of ~

1.27 cm were weighed before and after sputtering using a Sartorius SE-2 microbalance (0.1 μg precision). These disks were arranged on the sputtering substrate table as shown in Figures 2.3 in the pseudobinary runs. The mass per unit area across the library was determined after the deposition was completed.

2.3 Structural Analysis

2.3.1 X-Ray Diffraction

The scattered x-rays by atoms in a solid form the basis of the x-ray diffraction (XRD) technique. The x-ray diffraction method is a non-destructive technique used to characterize the crystallographic structure, crystallite size, and preferred orientation in crystalline samples.

X-rays are generated in x-ray tubes when the anode material (usually Cu) is bombarded with a beam of electrons that is accelerated by a high voltage, typically 10^4 V. The x-rays produced, which have a wavelength on the order of the lattice spacing, are directed to the sample being studied by a collimator, which aligns and focuses the beam. In a crystalline material, the atoms are arranged in a periodic lattice forming sets of parallel planes. Figure 2.4 demonstrates the basic principle of x-ray diffraction. Consider the two incident x-rays. These waves are diffracted from parallel atomic planes and constructive interference of the scattered x-rays will occur when Bragg's law is satisfied [14]:

$$n\lambda = 2d\sin\theta \qquad (2.3)$$

where d is the distance between the atomic planes in the crystal, θ is the angle of constructive diffraction, n is an integer, and λ is the x-ray wavelength, chosen to be comparable to the atomic spacing size. Therefore, if the x-ray wavelength is known and the angle of constructive diffraction is determined, the distance between atomic

planes can be calculated. The incident x-ray, reflected x-ray, and the normal to the scattering planes are coplanar. The angle between the incident and scattered x-ray wave vectors is 2θ and is defined as the scattering angle. A typical x-ray diffraction pattern for a single crystal shows sharp peaks centered at the angles satisfying Bragg's law. For a polycrystalline sample, the crystal grains are randomly distributed and the x-ray can interact with different families of planes of the sample to give constructive interference at different angles. The peak intensity is plotted versus the scattering angle, 2θ. Several factors, such as the structure factor and peak multiplicity, can play a role in the peak intensities.

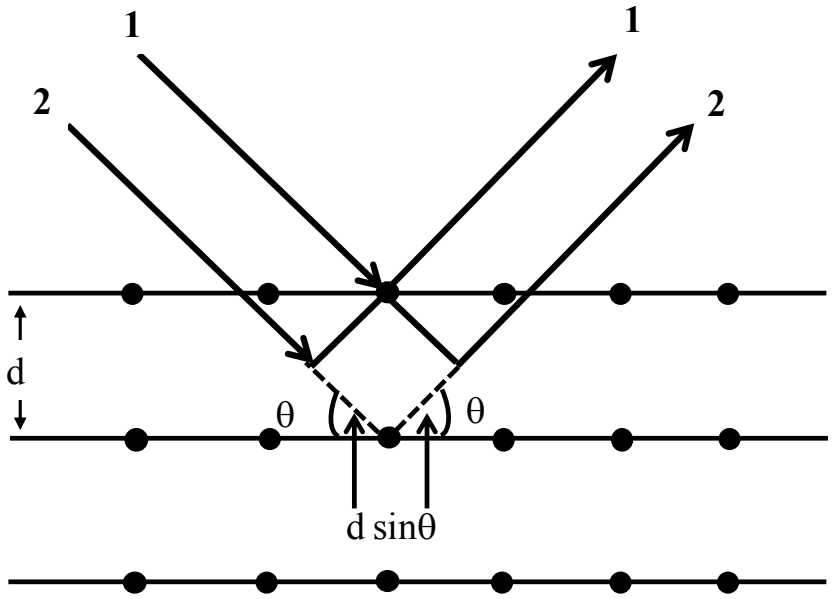

Figure 2.4: Schematic of a basic x-ray diffraction experiment.

The width of an individual peak, often defined as the full width at half the maximum, *w*, can be used to estimate the size of crystallite regions by the Scherrer formula:

$$w = \frac{0.9\lambda}{L\cos\theta} \qquad (2.4)$$

where L is the crystalline region size and λ is the wavelength. As the size of crystalline regions decreases the peaks become broader and of smaller amplitude. Most of the investigated materials in this thesis show very broad peaks. The material will be described as amorphous or nanocrystalline if the diffraction peaks are more than 8 degrees wide on the 2θ axis corresponding to a grain size of less than 5 nm or in the absence of any observable peaks.

XRD data were collected using two different diffractometers, an INEL CPS120 curved position sensitive detector equipped with PW-1720 Phillips x-ray generator tube and a Bruker D-8 Discover diffractometer equipped with a Vantec-2000 area detector. The INEL is equipped with an automated motion stage that can be programmed for an efficient data collection. In order to limit the wavelength of the x-rays hitting the sample, a monochromator is present in the path of the incident ray. The x-ray beam is incident at about 6 degrees with respect to the sample level. Figure 2.5 shows a photograph of the INEL diffractometer. The curved detector collects the entire diffraction pattern of a particular material over a wide range of angles simultaneously. More details on the operation of this detector are available in reference [15]. In this machine, the sample and the orientation of incident x-ray beam are stationary. The Bruker D-8 is equipped with a Cu target x-ray tube and a Gobel mirror and can measure up to 25^{o} per frame. This machine was also used for the XRD measurements of the ternary libraries.

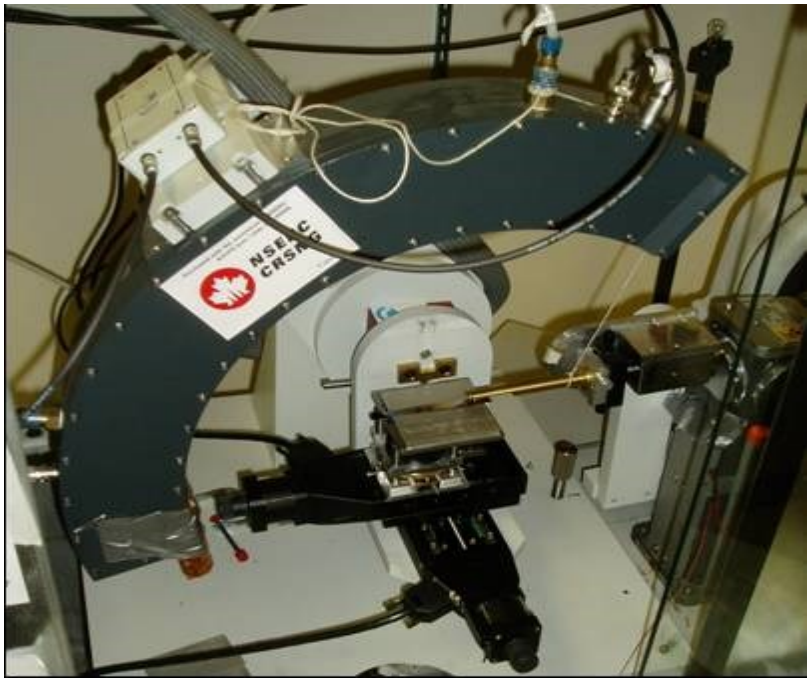

Figure 2.5: Photograph of the Inel.

2.3.2 Mössbauer Spectroscopy

Sn- and Fe-containing amorphous or nanostructured alloys have been found to be promising materials for negative electrode use in Li-ion batteries [16]. However, determining the properties of materials when they are nanostructured is difficult on the basis of x-ray diffraction measurements. Mössbauer effect (ME) spectroscopy can give more details about the microstructure of a material as it probes the structure of a material on the atomic scale. This section is intended to give a very brief introduction about this useful technique. The theory of the Mössbauer effect has been extensively discussed in different text books including [17].

Classically, when a gamma ray is emitted by the nucleus in a free atom as the nucleus undergoes a transition from an excited state to its ground state, the energy of the emitted gamma ray is reduced by an amount equal to the recoil energy that is imparted to the nucleus on the basis of energy and momentum conservation. In order for resonant absorption of the emitted gamma ray to occur at the absorber

nucleus, the gamma ray must be equal to the energy of the excited state plus twice the recoil energy. Figure 2.6 shows a schematic representation of energy distributions during emission and absorption.

It is clear from Figure 2.6 that the emission and absorption lines have a certain spread of energies. The main contributions to this energy distribution are (1) the natural line width Γ (FWHM) of the excited state, which is related to the Heisenberg uncertainty principle (according to $\Gamma\Delta t \sim \hbar$ where Δt is the mean life time of the excited state and $\hbar$ is Planck's constant) and (2) Doppler broadening related to the thermal broadening. However, these two contributions are generally too small to produce a significant energy overlap depicted in Figure 2.6.

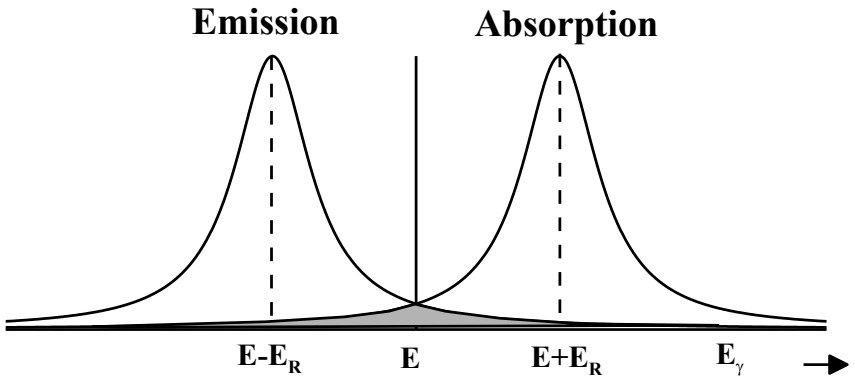

Figure 2.6: Schematic representation of the distribution energy for emission and absorption. Resonant overlap in energy is indicated by the shaded area [17].

The basic physics of this process may be described as follows: The recoil energy E_R is given by:

$$E_R = \frac{E_\gamma^2}{2Mc^2} \qquad (2.5)$$

where E_γ is the gamma-ray energy, M is the mass of the nucleus, and c is the speed of light. Typically for a nuclear transition, the recoil energy is on the order of 10^{-4} to 10^{-2} eV. This value is typically much larger than the line width of an excited nuclear state. As a consequence of the recoil-loss in energy, both the emission and the absorption lines are displaced relative to each other. The above discussion refers to the case of gamma rays emitted by a free nucleus. However, if the atoms are considered to be bound in a lattice (binding energy on the order of 1-10 eV), the recoil energy becomes much smaller, according to Eq. 2.5 as the relevant mass is the mass of the entire lattice and not just the mass of a free atom. The energy states of a crystal lattice are quantized in units of $\hbar\omega$, where ω is the lattice vibrational frequency. The recoil energy can be transferred to the lattice vibration, *i.e.* phonons. The emitting nucleus may not be able to transfer its recoil energy to excite these phonons, and the recoil momentum will be taken up by the crystal as a whole. This situation is known as recoil-free fraction. The probability of having such event is given by:

$$f = 1 - \frac{E_R}{\hbar\omega} \qquad (2.6)$$

The mass of the nucleus and gamma-ray transition energy are factors that contribute to the recoil-free fraction. Clearly, larger values of f are desirable. We also see from Eq. 2.6 that larger values of lattice vibrational energy are desirable.

Figure 2.7shows the decay schemes that populate the Mössbauer levels of ^{57}Fe and ^{119}Sn, two of the most commonly use Mössbauer probes and the two which are used in this thesis research. ^{57}Co, which has 270 day half-life time, decays by

electron capture resulting in the population of the 14.4 keV Mössbauer state of ^{57}Fe. For Sn measurements, metastable ^{119m}Sn decays by gamma emission to the 23.88 keV level used for Mössbauer measurements.

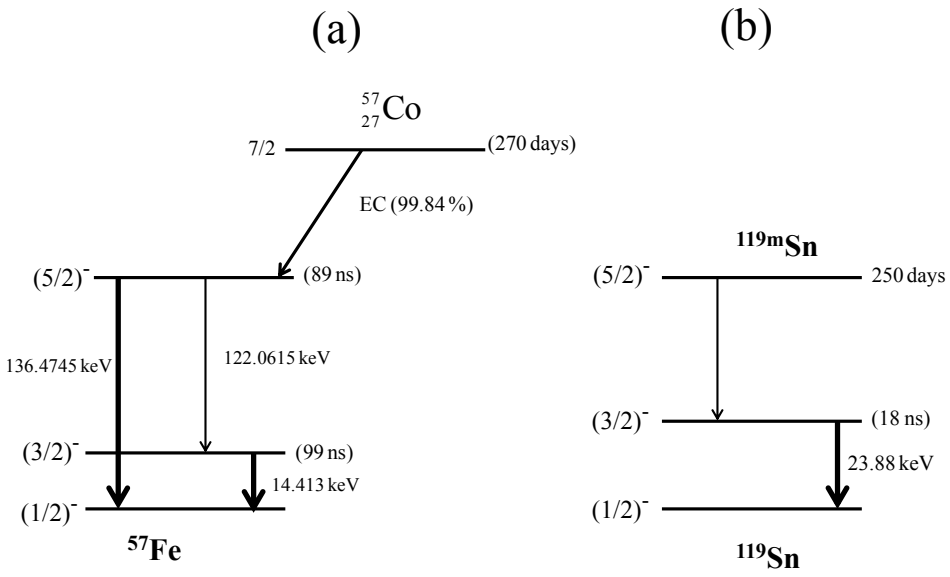

Figure 2.7: Decay schemes for (a) ^{57}Co and (b) ^{119m}Sn. Thick arrows show Mössbauer transitions. The energy of each state and spin values are shown. Reproduced from reference [17].

Figure 2.8 depicts the basic elements of a Mössbauer spectrometer which involves a radioactive source that contains the Mössbauer isotope in an excited state, an absorber, gamma ray detection unit, and a drive to move the source. The gamma rays emitted by the source pass through the absorber, where some of the gamma rays will be absorbed, and then pass to a detector. In order to investigate the energy levels of the Mössbauer nucleus in the absorber it is necessary to modify the energy of the gamma rays emitted by the source so that they have the correct energy for resonant absorption. This is usually accomplished by moving the source within a suitable range, relative to a stationary absorber and hence giving the gamma rays an energy shift as a result of the Doppler Effect as given by:

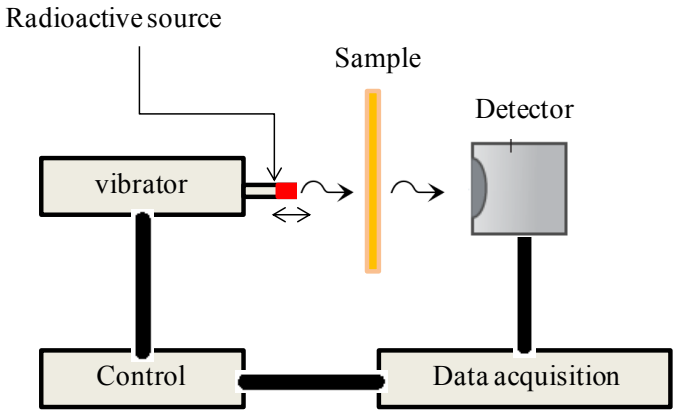

Figure 2.8: Schematic of an experimental set-up for transmission Mössbauer spectroscopy.

$$E_D = \frac{v}{c} E_\gamma \qquad (2.7)$$

where v is the velocity of the source and c is the speed of light. The resulting spectrum is accumulated for a period typically on the order of hours or days during which this spectrum may be monitored on a display screen.

Features of Mössbauer spectral lines, such as number, intensity, width, position, and shape are the result of interactions between the absorber atom and it surroundings and its effect on the hyperfine structure of the nuclear energy levels. Three types of hyperfine interactions are considered during the fitting of the Mössbauer spectrum; chemical isomer shift (δ), the quadrupole splitting (Δ), and the magnetic hyperfine interaction. Figure 2.9 shows schematic of energy level diagrams depicting each one. A brief description on each parameter is given as follows:

1. Isomer shift (δ): If both the source and absorber are in identical chemical environments, the resonance absorption peak will consist of a Lorentzian

function centered at E_γ. However, if some difference exists in s-electron densities at the source and absorber nuclei then this results in a displacement of the spectrum as a whole from zero relative velocity. The hyperfine interaction parameter corresponding to this displacement of the resonant peak is called the isomer shift (δ). For a given source the isomer shift, δ, measured from some standard is a linear function of the electron charge density $|\psi(0)|_A^2$ at the absorber nucleus and is given by:

$$\delta = \text{const.}\left[|\psi(0)|_A^2 - |\psi(0)|_S^2\right] \times \left[R_e^2 - R_g^2\right] \qquad (2.8)$$

$\psi(0)_A$ and $\psi(0)_S$ are the s electron density at the core of the source *S* and the absorber A, respectively. R_e and R_g are the radius of the excited (e) and ground (g) state, respectively. This isomer shift, δ, can be related to the measured shift in Doppler velocity, *v*, by Eq. 2.7. As can be seen, this parameter gives information about the electron density at the nucleus and hence the valence statee. The isomer shift, as defined above is the velocity shift at zero temperature. The center shift as discussed in the coming chapters is defined as the zero temperature isomer shift plus small changes due to the temperature dependent from second order Doppler effect.

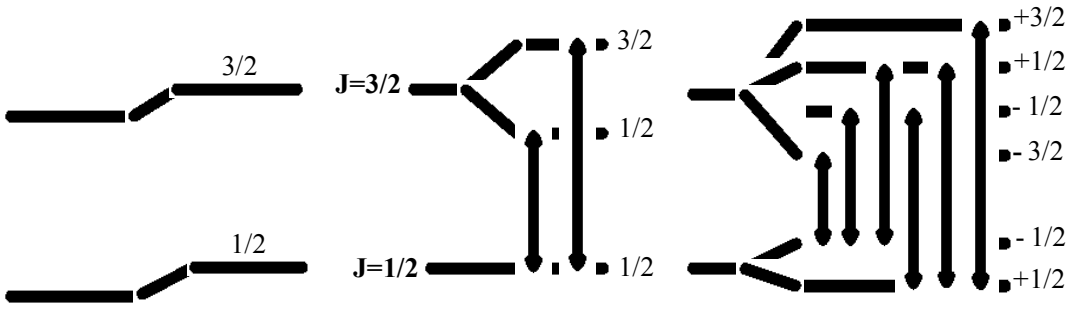

(a) Isomer shift (b) Quadrupole splitting (c) Magnetic splitting

Figure 2.9: Energy levels diagrams for ^{57}Fe when the unsplit source and absorber are in different local environments showing all possible nuclear transitions. (a) Representing the isomer shift; (b) Interaction of the nuclear quadrupole moment with the electric field gradient leads to splitting of the nuclear energy levels, causing a doublets in the Mössbauer spectrum; (c) presence of magnetic field at the nucleus, yielding a sextet pattern in the Mössbauer spectrum.

2. Quadrupole splitting (Δ): This arises from the interaction between the electric field gradient which exists at a nucleus of the absorber with electric quadrupole moment of the absorbing nucleus. The presence of electric field gradient is related to the geometry of the crystal whereas the nuclear quadrupole moment is a measure of the deviation of the nuclear charge from spherical symmetry. This interaction is given by:

$$\Delta = \frac{eQV_{zz}}{4J(2J-1)}\left[3m_J^2 - J(J+1)\right]\left(1+\frac{\eta^2}{3}\right)^{1/2} \qquad (2.9)$$

where e is the charge of an electron, Q is the quadrupole moment, V_{zz} is the z-component of electric field gradient, J is the total spin, m_J is the nuclear magnetic spin, and η a parameter that describes the asymmetry about the z axis (η equal zero for cubic symmetry about the Mössbauer nucleus). In the presence of an electric field gradient at a nucleus, a state of spin of J=3/2, will split into sublevels that correspond to different magnitudes of m_J. The center of

the resulting doublet corresponds to the isomer shift discussed earlier in this section.

3. Nuclear Zeeman Effect: In the presence of a magnetic field, *H,* the nuclear energy levels of a nucleus with a magnetic moment, μ, and total spin $J > 0$ will split into $(2J+1)$ sublevels. This interaction is expressed as:

$$E_m = -g\mu_N H m_J \qquad (2.10)$$

where g is the nuclear g-factor, μ_N is the nuclear magneton, and m_J is the magnetic quantum number. In ^{57}Fe, as an example, the excited spin 3/2 state splits into four levels and the spin ½ ground state split into two levels as depicted in Figure 2.9(c). The allowed transitions are indicated by the arrows.

In this thesis, room temperature ^{57}Fe Mössbauer effect spectra were collected using a $\underline{Rh}^{57}Co$ source and a W302 spectrometer from SEE Co. A Wissel System II spectrometer and $Ca^{119m}SnO_3$ source were used for ^{119}Sn measurements. Both spectrometers operate in the constant acceleration mode. The velocity scale was referenced using the spectra for room-temperature of α-Fe and $BaSnO_3$ for Fe and Sn Mössbauer measurement, respectively. The acquisition time of the spectrum was usually 24 hours, but could differ depending of the sample composition. The software package Recoil 1.0 (K. Lagarec and D.G. Rancourt, University of Ottawa) was employed to fit all the spectra [18].

2.4 Electrochemical Measurements

In this thesis, the electrochemical study of sputtered materials was performed using a half cell with a Li metal foil as counter and reference electrode. Therefore, all materials produced and tested served as positive electrodes. Electrodes used were cycled using cyclic voltammetry, in which a linear potential sweep was applied to the cell and the current was measured. Current-versus-potential data can

be plotted as a cyclic voltammogram. In this thesis, the electrochemical features of the prepared cells were evaluated and discussed through two different kinds of plots: (1) potential versus specific capacity curve and (2) differential capacity plots, from which the potential corresponding to various electrochemical reactions can be identified. Differential capacity can be calculated from the current, I, and charge, Q, and voltage, V, as:

$$\left(\frac{dQ}{dV}\right)=\left(\frac{dQ}{dt}\right)\left(\frac{dt}{dV}\right) \qquad (2.11)$$

where $$I=\left(\frac{dQ}{dt}\right)$$

Figure 2.10 presents a voltage curve of a Si thin film showing two sloping plateaus, which is indicative of an amorphous or nanostructured electrode material. These features are more identifiable in the differential capacity plots and are reflected by the two humps shown in Figure 2.11. In contrast, these sloping plateaus in the voltage curve in crystalline materials become flat plateaus and are represented by sharp peaks in the differential capacity plots.

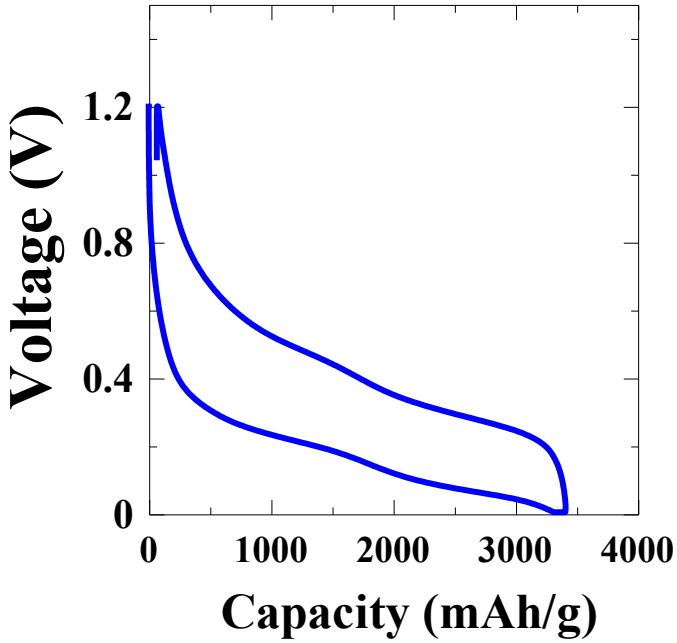

Figure 2.10: Potential versus specific capacity curve of amorphous sputtered Si thin film.

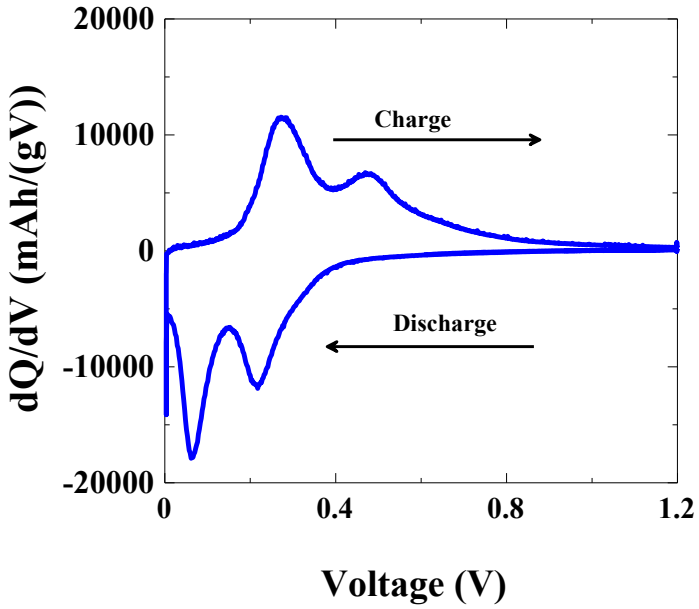

Figure 2.11: Differential capacity plot of amorphous sputtered Si thin film.

Some of the important parameters for evaluating electrode materials are:

(1) Specific capacity: it is the amount of available charge that can be withdrawn per unit mass from a fully-charged electrode under specified conditions. The theoretical specific capacity can be calculated as:

$$\text{gravimetric capacity} = \frac{nF}{m}\left(\frac{\text{C}}{\text{g}}\right) = \frac{nF}{3.6m}\left(\frac{\text{mAh}}{\text{g}}\right) \qquad (2.12)$$

where n is the number of moles of electrons involved in the reaction, F is Faraday's constant (96,487 Coulombs), and m is the atomic weight of the material. Volumetric capacity can be obtained by multiplying the gravimetric capacity (mAh/g) by the density of the material (in g/cc) to obtain the capacity in mAh/cc. Volumetric capacity is of particular interest for batteries that can be incorporated in portable devices. It is essential factor to use high capacity electrode materials to develop a high energy density battery.

(2) Irreversible capacity: it is the difference between the first discharge (Li insertion) and charge (Li extraction) capacities. Different factors can contribute to the irreversible capacity, such as the formation of a passivation layer on the surface of the electrode consuming Li or electrolyte, trapping of Li in the host material, and reaction with surface oxide layers. Generally, thin films show lower irreversible capacity than the bulk samples as a result of faster diffusion processes. Ideally the amount of irreversible capacity should be minimized.

(3) Cycle life: it is represented by the number of discharge-charge cycles that can be obtained from a battery before it degrades to 80% of its initial reversible value. Many factors affect the cycle life and capacity retention such as the structural stability during operation. Obviously, a large number of cycles is desired.

Figure 2.12 shows the new design of the combinatorial cell plate (details are presented in Chapter 3). It consists of 64 pads, where the material of interest is deposited. These pads are arranged in an 8 × 8 grid, which can fit within the

sputtering track as shown in Figure 2.3. Each pad is 5 mm in diameter and has its own electrical contact for connection to the charger. In order to deposit the material under investigation on these pads, the cell plate was covered by a mask so that only the contact pads were exposed. Such an approach provided 64 discrete electrodes with different compositions. The combinatorial cell was designed in the Dahn research group and was prepared by commercial suppliers.

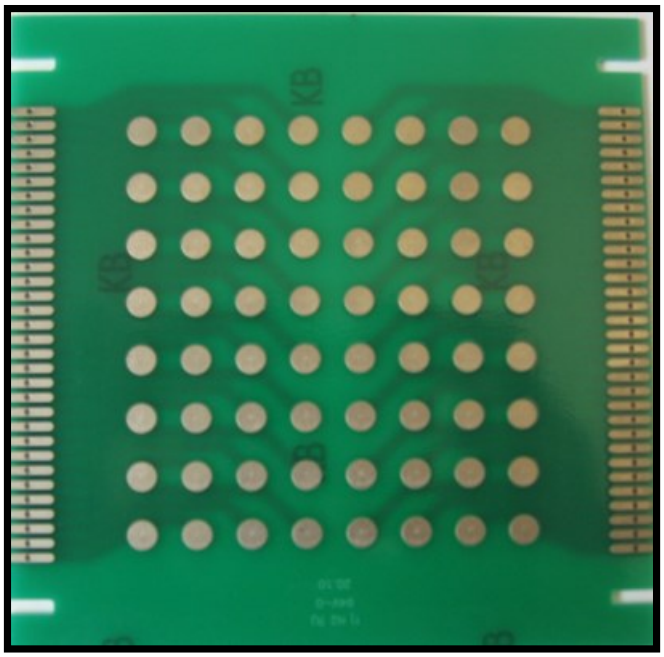

Figure 2.12: Photograph of 64-channel printed circuit board electrochemical cell plate [19].

Figure 2.13 shows a schematic representation of the combinatorial cell hardware [20]. The construction of the combinatorial cell can be summarized as follows: (1) the cell plate was loaded onto the aluminum base and wetted with 2 mL of electrolyte [1 M $LiClO_4$ (Aldrich) in 33:67 ethylene carbonate/diethyl carbonate (EC:DEC) (Ferro Corporation)]; (2) two different kinds of separators were placed onto the combinatorial electrochemical cell: a Celgard 2300 microporous film and a polypropylene blown micro fiber (BMF) separator (available from 3M Company). The microporous film was placed in contact with the Li foil and the BMF contacted the material to be investigated; (3) Li foil was laid on top of the separators to be used as a common counter and reference electrode; and (4) the whole stack was then capped with a stainless steel top to seal the cell and the cell was bolted together. The author did a study to optimize the stack pressure and found that the combination of separators described here provided uniform pressure on each of the 64 electrodes. The assembly procedure was performed in an argon-filled glove box. Then the cell was removed from the glove box and was ready for electrochemical testing.

The assembled combinatorial cell typically had an open-circuit voltage (around 2.6 V) and is in its fully charged state. The combinatorial cell was then cycled potentiodynamically using an in-house built multichannel pseudopotentiostat system. All 64-electrodes of each cell were analyzed simultaneously. All the cells were tested at room temperature. Typically, cells were discharged using linear sweep voltammetry from open-circuit voltage (around 2.6 V) to 1.2 V in 30 minutes. The potential was held at 1.2 V for 30 minutes then the cell was discharged to 0.005 V in 12 hours. This was followed by a hold at 0.005 V for 3 hours. The potential was then returned to 1.2 V in 12 hours and held for 30 minutes. This procedure was then repeated three times followed by 20 cycles where a rate of C/3 was used. A further 3 cycles at C/12 were carried out at the end of cycling. This particular cycling protocol was chosen in order to study the response of the material to different scan rates and to understand how different rates affect the structural and

electrochemical properties of the material. Using the masses of each deposited electrode, the specific capacity was calculated. All voltages in this thesis are quoted relative to a Li electrode.

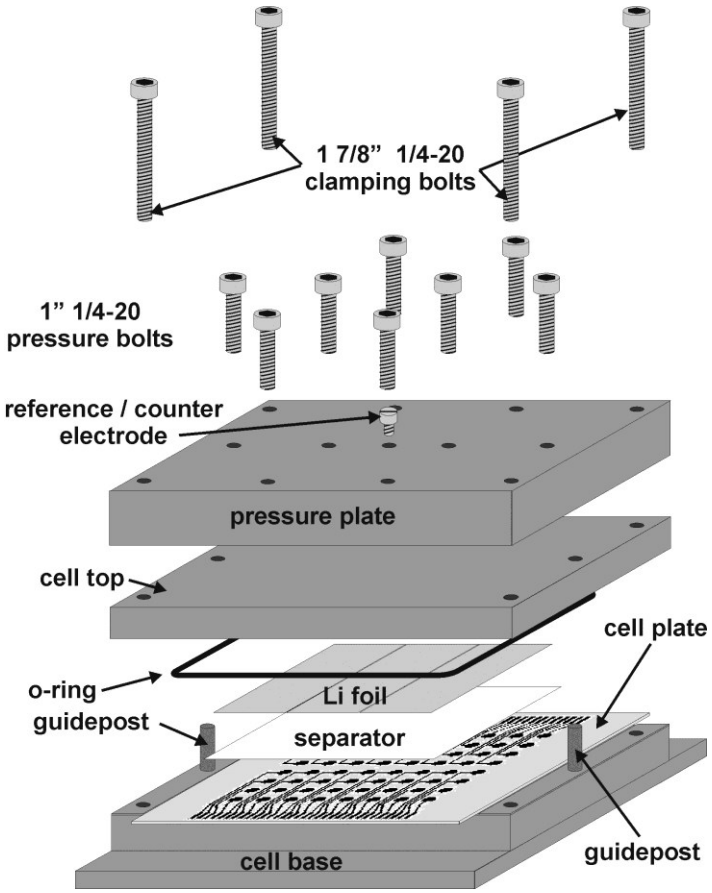

Figure 2.13: Schematic of the combinatorial electrochemical cell [20].

2.5 References

[1] L. Thompson and J. Ellman, "Synthesis and applications of small molecule libraries", *Chem. Rev.* **96** (1996) 555-600.

[2] E. Gordon, M. Gallop, and D. Patel, "Strategy and tactics in combinatorial organic synthesis applications to drug discovery", *Acc. Chem. Res.* **29** (1996) 144-154.

[3] K. Kennedy, T. Stefansky, G. Davy, V. Zackay, and E. Parker, "Rapid method for determining Ternary-Alloy phase diagrams", *J. Appl. Phys.* **36** (1965) 3808-3810.

[4] J. Hanak, "The multiple-sample concept" in materials research: Synthesis, compositional analysis and testing of entire multicomponent systems", *J. Mater. Sci.* **5** (1970) 964-971.

[5] X. Xiang, X. Sun, G. Briceno, Y. Lou, K. Wang, H. Chang, W. Wallacefreedman, S. Chen, and P. Schultz, "A combinatorial approach to materials discovery", *Science* **268** (1995) 1738-1740.

[6] E. Reddington, A. Sapienza, B. Gurau, R. Viswanathan, S. Sarangapani, E.S. Smotkin, and T.E. Mallouk, "Combinatorial electrochemistry: A highly parallel, optical screening method for discovery of better electrocatalysts", *Science* **280** (1998) 1735-1737.

[7] I. Yanase, T. Ohtaki, and M. Watanabe, "Application of combinatorial process to $LiCo_{1-x}Mn_xO_2$ powder synthesis", *Solid State Ionics* **151** (2002) 189-196.

[8] J. Dahn, S. Trussler, T. Hatchard, A. Bonakdarpour, J. Mueller-Neuhaus, K. Hewitt, and M. Fleischauer, "Economical sputtering system to produce large-size composition-spread libraries having linear and orthogonal stoichiometry variations", *Chemistry of Materials* **14** (2002) 3519-3523.

[9] M. Fleischauer, M. Obrovac, and J. Dahn, "Al–Si thin-film negative electrodes for Li-ion batteries", *J. Electrochem. Soc.* **155** (2008) A851-A854.

[10] P. Liao, B. MacDonald, R. Dunlap, and J. Dahn, "Combinatorially prepared $[LiF]_{1-x}$ Fe_x nanocomposites for positive electrode materials in Li-ion batteries", *Chemistry of Materials* **20** (2007) 454-461.

[11] J. Vossen and W. Kern, "Thin film processes", Academic Press, New York (1978).

[12] K. Chopra, "Thin film phenomena", McGraw-Hill, New York (1969).

[13] J. Goldstein, "Scanning Electron Microscopy and X-ray Microanalysis : A text for biologists, materials scientists, and geologists", Plenum Press, New York (1992).

[14] R. Jenkins and R. Snyder, "Introduction to X-ray Powder Diffractometry", Wiley, Hoboken (2012).

[15] J. Ballon, V. Comparat, and J. Pouxe, "The blade chamber: A solution for curved gaseous detectors", *Nuclear Instruments and Methods in Physics Research* **217** (1983) 213-216.

[16] M. Fleischauer, J. Topple, and J. Dahn, "Combinatorial investigations of Si-M (M= Cr, Ni, Fe, Mn) thin film negative electrode materials", *Electrochemical and Solid-State Letters* **8** (2005) A137-A140.

[17] N. Greenwood and T. Gibb, "Mössbauer spectroscopy", Chapman and Hall, London (1971).

[18] K. Lagarec and D.G. Rancourt," Recoil-Mössbauer spectral analysis software for windows", University of Ottawa, Ottawa (1998).

[19] M. Al-Maghrabi, N. van der Bosch, R. Sanderson, D. Stevens, R. Dunlap, and J. Dahn, "A new design for a combinatorial electrochemical cell plate and the inherent irreversible capacity of lithiated silicon", *Electrochemical and Solid-State Letters* **14** (2011) A42-A44.

[20] M. Fleischauer, T. Hatchard, G. Rockwell, J. Topple, S. Trussler, S. Jericho, M. Jericho, and J. Dahn, "Design and testing of a 64-channel combinatorial electrochemical cell", *J. Electrochem. Soc.* **150** (2003) A1465-A1469.

Chapter 3:

A New Design for a Combinatorial Electrochemical Cell Plate and the Inherent Irreversible Capacity of Lithiated Silicon[1]

M. A. Al-Maghrabi, Nils van der Bosch, R. J. Sanderson, D. A. Stevens, R. A. Dunlap, and J. R. Dahn

3.1 Abstract

A new design for a 64-electrode cell plate for combinatorial electrochemical studies of electrodes for Li-ion cells is described. This plate, made using circuit board technology, has advantages over previously used plates made by sputtering electrode pads onto glass. It eliminates spurious capacity from the sputtered lead pattern exposed to electrolyte; it can be easily and economically produced in quantity, and it is more robust. This plate design was tested using a sputtered Si wedge. With these improved plates, the irreversible capacity if Li_xSi was measured to be less than 70 mAh/g or less than 2% of the reversible capacity.

[1] This chapter was published in Electrochemical and Solid-State Letters, 14 (4) A42-A44 (2011).

3.2 Introduction

The use of combinatorial sputtering methods has allowed for the high throughput investigation of the composition dependence of the properties of a wide variety of materials [1–3]. One field that has benefited greatly from the availability of combinatorial science techniques has been the development of new materials for advanced battery electrodes [4]. Cumyn et al. [5] and Fleischauer et al. [6] have reported the design of a 64-channel electrochemical cell for the efficient testing of combinatorially sputtered electrode arrays. In this method, the cell electrode array is prepared by sputtering 64 conductive leads and pads in an 8 × 8 array on a glass cell plate. This approach has provided a highly efficient method of testing the composition dependence of the electrochemical properties of potential Li-ion battery electrode materials, particularly those for use as negative electrodes (e.g., References [7–9]).

There have been three drawbacks to this technique as a result of the cell plate design: (1) the production of the plates by sputtering methods is both time consuming and expensive, (2) the plates sometimes break when the cell is assembled, and (3) the sputtered copper lead pattern oxidizes over time and, when exposed to the cell testing conditions, contributes irreversible capacity [6]. In order to alleviate these difficulties, we have designed and tested a combinatorial cell plate based on a printed circuit board. The present article describes the design of this cell plate and the results of a test utilizing a sputtered Si electrode with a thickness gradient.

3.3 Experimental Techniques

A 64-channel electrochemical cell plate has been constructed utilizing standard, 1 mm thick, resin-based printed circuit board. Cell plates were designed with Eagle software from Cadsoft USA. The circuit boards were made by Optima Technology

Associates Inc. (Lewisberry, PA). Figure 3.1 shows the details of the new cell plate. Figure 3.1(a) shows a photograph of the top of the cell plate. Figure 3.1(b) shows a cross section of the region near a conducting pad. The board has been drilled to allow the conductors to exit the back side, and the drilled hole has been electroplated with copper and the central hole filled with solder. Then a nickel layer was applied to the top of the copper pad to cover the solder. The pads were plated with nickel in order to: (1) prevent the contact of the cell electrolyte with the solder since Li will alloy with solder at low potentials; (2) prevent irreversible capacity in studies of alloy negative electrodes since Ni does not form a thick oxide (unlike copper as was used in the old design [6]); and (3) reduce the possibility of oxidation prior to use. Figures 3.1(c) and 3.1(d) show the conductor patterns on the top and bottom of the board, respectively.

The electrode material to be studied is sputtered, through an appropriate shadow mask, onto the pads on the top side of the board. For the purpose of testing this electrochemical cell plate, high purity Si was sputtered onto the plate using a modified Corona Vacuum Model V-3T system (Vancouver, B.C., Canada) [3]. A“linear-out” mask [6] was used in order to obtain a linear variation in Si thickness from right to left across the cell plate in Figure 3.1(a). Sputtering was done with the substrate at room temperature under an argon pressure of 1 mT. Total sputtering time was 7 h. Cu foil weighing disks positioned on the sputtering table were weighed before and after the sputtering run using a Sartorius microbalance (0.1 μg precision) to determine the position dependence of the mass per unit area of the Si deposit. The mass per unit area was used to calculate the specific capacity of the Si deposited on each 5.0 mm diameter electrode pad. Electron microprobe studies showed that the oxygen content of the film was less than 1% atomic over most of the film and always less than 3% atomic.

A combinatorial electrochemical cell was constructed as described by Fleischauer et al. [6] for the testing of the new combinatorial cell plates. A common Li counter and reference electrode, 1 M $LiClO_4$ in (ethylene carbonate) EC: (diethyl

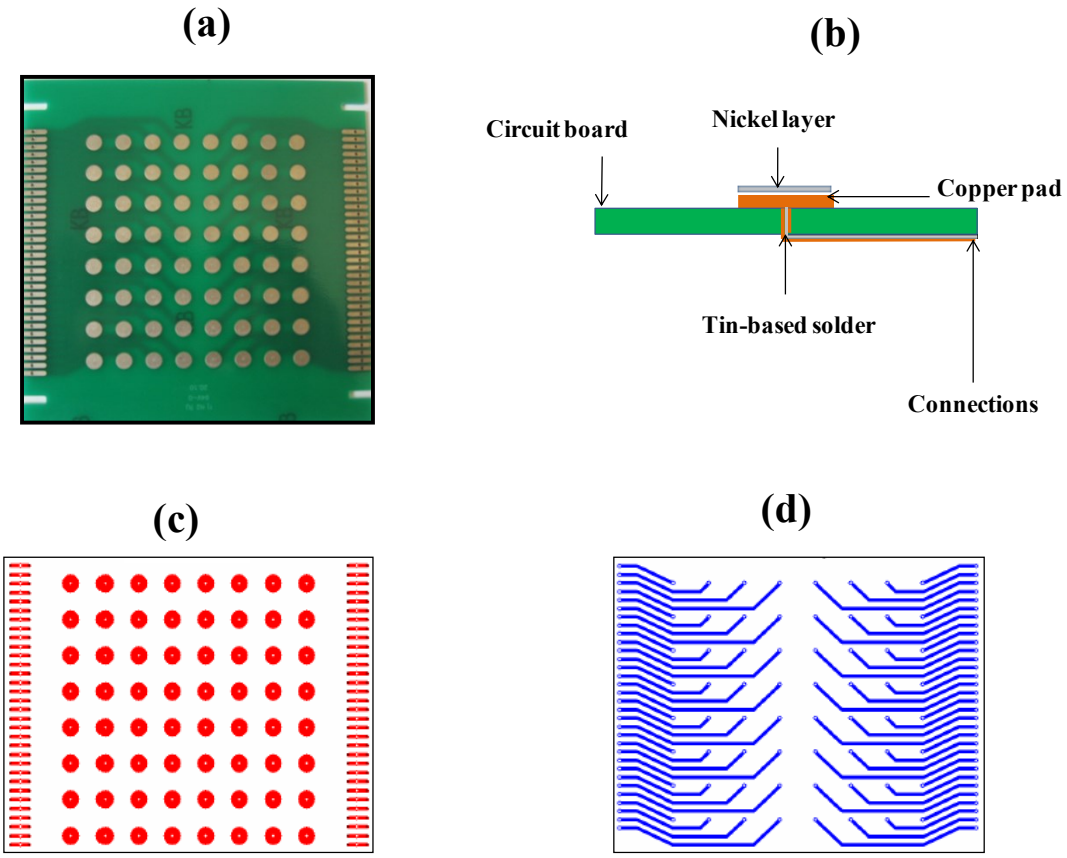

Figure 3.1: (a) Photograph (from top side) of 64-channel printed circuit board electrochemical cell plate, (b) schematic of cross section through printed circuit board cell plate showing connection of cell pads with charger leads, (c) lead pattern on top of printed circuit board, and (d) lead pattern on bottom of printed circuit board.

carbonate) DEC 1:2 electrolyte and Celgard 2300 separator were used. Cyclic voltammetry measurements were performed on the 64-channels of the cell plate using a multichannel pseudopotentiostat as described by Cumyn et al. [5]. Cells were discharged/charged between 1.2 and 0.005V using scans that took 15 h (for a discharge or a charge) for a total of five cycles.

3.4 Results of Electrochemical Testing

Differential capacity versus potential of the Si electrodes on the 64-electrode cell plate is shown in Figure 3.2. The differential capacity, dQ/dV, was obtained from the cyclic voltammogram current using dQ/dV = I dt/dV. The data for the 64 charger channels shown in Figure 3.2 map directly onto the 64-electrode pads illustrated in Figure 3.1. Data are shown for the first three cycles. The capacity increases with the amount of Si on the pads, from left to right in Figure 3.2. Figure 3.2 shows a consistent trend across the cell plate as expected since each column of electrodes contains the same mass of Si. However, there are some electrodes along the bottom row that do not fit the overall trend. This can occur in testing of combinatorial cells from time to time and can be caused by uneven application of pressure on the electrode plate. For sputtered films that have a one dimensional composition or mass gradient, there are a sufficient number of electrodes that are nominally the same to allow for consistency checks of the results. Overall the results for the 64 electrodes as described in Figure 3.2 are at least equivalent to the quality of typical combinatorial electrochemistry results in the literature.

The second cycle capacity as a function of the mass of the sputtered electrode for the electrodes in rows 2 through 5 (corresponding to electrodes 9 through 40) is shown in Figure 3.3. The results for different rows of cells are quite consistent, and the total capacity increases as a linear function of electrode mass as expected. A fit to the data shown in Figure 3.3 gives a slope of 3550 ±150 mAh/g for the specific

of Li_xSi in good agreement with the theoretical value of 3580 mAh/g (reference [10]).

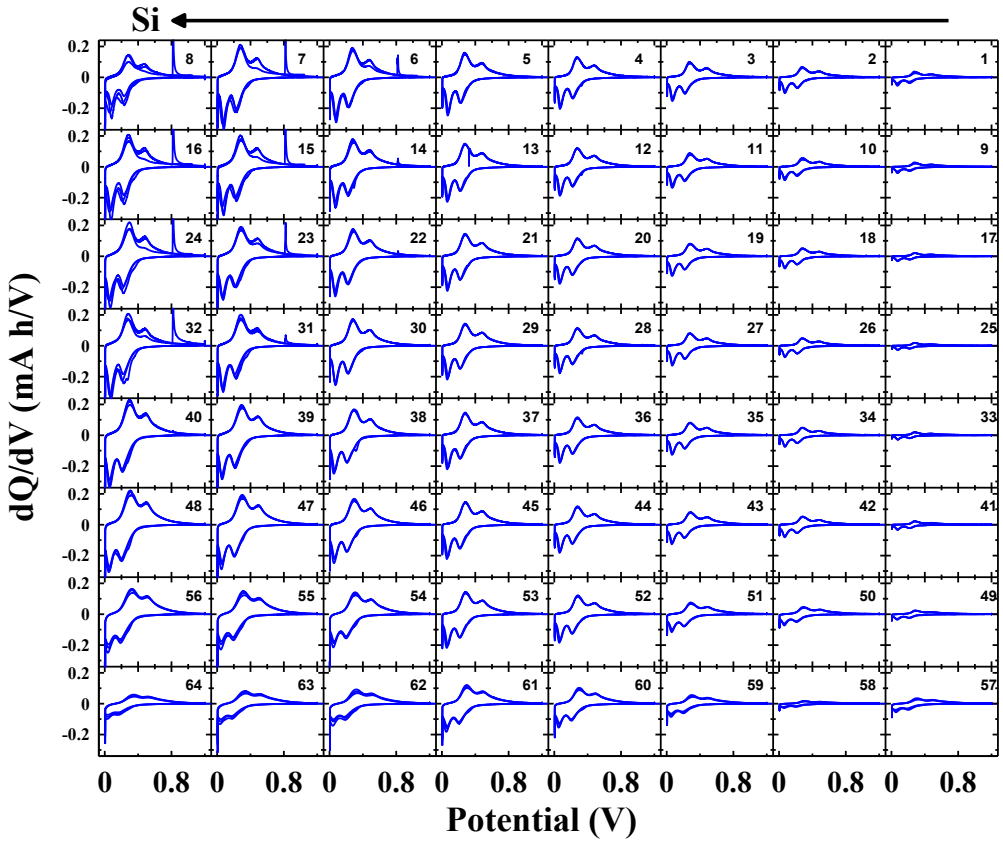

Figure 3.2: Differential capacity of the 64 charger channels. The 64 channels map onto the 64 cell pads illustrated in Figure 3.1. Data are shown for the first three cycles.

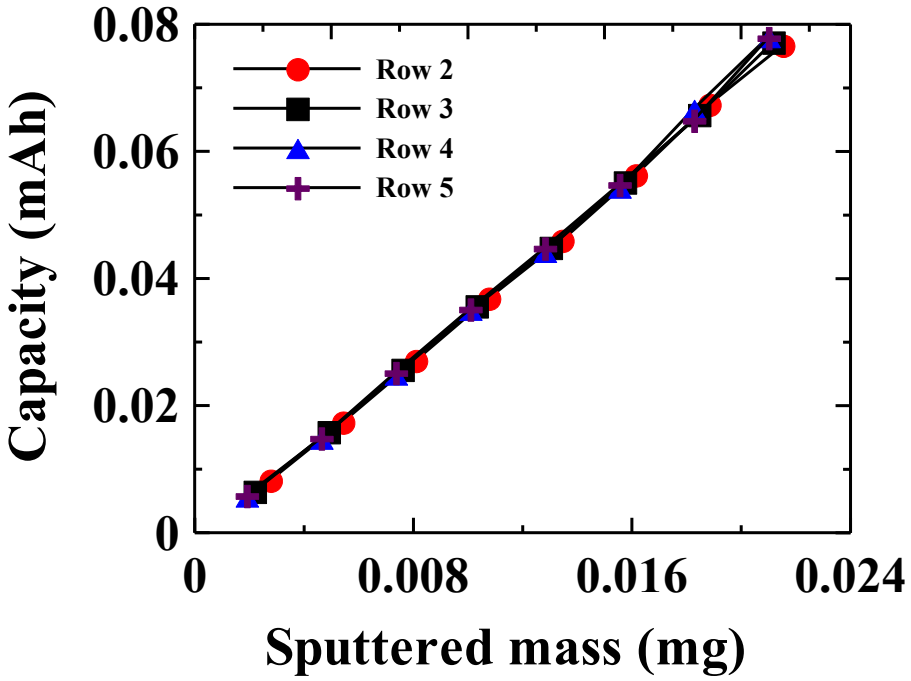

Figure 3.3: Cell capacity as a function of sputtered Si electrode mass corresponding to rows 2 (circles), 3 (squares), 4 (triangles), and 5 (crosses). These correspond to the charger channels shown in Figure. 7–9 of row 2 (channels 9–16), row 3 (channels 17–24), row 4 (channels 25–32), and row 5 (channels 33–40).

Figure 3.4 shows the potential versus. specific capacity for three typical electrodes, selected to be 47, 45, and 43. The capacity was obtained by integrating the current with respect to time ($Q = \int I\,dt$). What is especially noteworthy about Figure 3.4 is the extremely small irreversible capacity of only 60 mAh/g or about 2% of the reversible capacity for all electrodes, even electrode 43, which had a reversible capacity of only 25 μAh. In previous work by Fleischauer et al. [6], irreversible capacity from the copper lead and conductor pattern on the old glass cell plates was shown to be as large as 3 μAh (Figure 5 in Reference [6]). The irreversible capacity of electrode 43, using the old plate, would have been more

than 10% just from the Cu lead pattern itself, if corrections were not made. This demonstrates some important advantage of the new cell plates.

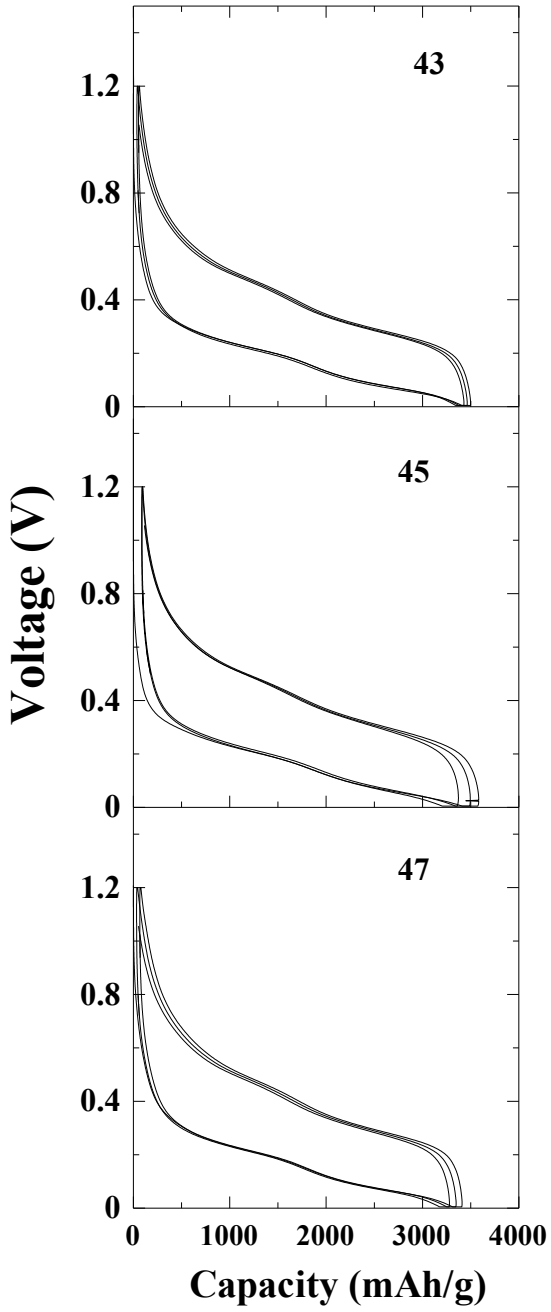

Figure 3.4: Potential versus specific capacity curves of the three typical charger channels; (a) channel 43, (b) channel 45, and (c) channel 47.

The results in Figure 3.4 put an upper bound on the true irreversible capacity of Si thin films. It must be less than 2% of the reversible capacity. By contrast, many literature reports show comparatively huge values of irreversible capacity, which is not inherent to well prepared Si. For example, Maranchi et al. [11] show irreversible capacities of 600 mAh/g (17%) for 250 nm thick Si and 400 mAh/g (13%) for 1μ thick Si. Graetz et al. [12] show irreversible capacities of 1000 mAh/g (33%) for a Si film, and Jung et al. [13] show irreversible capacities of over 800 mAh/g for 500 nm thick Si films. It is not clear how, or if, these previous authors may have accounted for the contribution of the substrate to the irreversible capacity of the Si films that they studied. After the experiments, using the circuit board cell plate, the combinatorial cell was opened, and the cell plate was carefully examined by eye and using an optical microscope. No evidence for dissolution, pitting, or damage to the cell plate was observed. Hence, we conclude that the resin used in the manufacture of these circuit boards is compatible with the electrolyte used. Additionally, the lithiated Si easily washed off the cell pads with water and the Ni pads appeared just as they did when new.

3.5 Conclusions

The new combinatorial electrochemical cell plate made using circuit board technology provides results that are consistent with those obtained using traditional glass cell plates. In addition, the new cell plate gives much smaller values of irreversible capacity due to the exposure of Ni, not Cu to the electrolyte. The irreversible capacity of sputtered Li_xSi was found to be less than 2%.

The new plates have the advantage of being more economical and convenient as they can be produced in bulk and stored until needed. They are also more robust and have the advantage of being virtually unbreakable during cell assembly. A final advantage of the new plate design is reusability. After cycling, the electrode

materials readily cleaned from the pads with water allowing the plate to be used again. This may be important in laboratories where funding is an issue.

3.6 References

[1] X. Xiang. "Combinatorial materials synthesis and screening: An integrated materials chip approach to discovery and optimization of functional materials", *Annual Review of Materials Science* **29** (1999) 149-171.

[2] J. Hanak, "The "multiple-sample concept" in materials research: Synthesis, compositional analysis and testing of entire multicomponent systems", *J. Mater. Sci.* **5** (1970) 964-971.

[3] J. Dahn, S. Trussler, T. Hatchard, A. Bonakdarpour, J. Mueller-Neuhaus, K. Hewitt, and M. Fleischauer, "Economical sputtering system to produce large-size composition-spread libraries having linear and orthogonal stoichiometry variations", *Chemistry of Materials* **14** (2002) 3519-3523.

[4] M. Roberts, A. Spong, G. Vitins, and J. Owen, "High throughput screening of the effect of carbon coating in $LiFePO_4$ electrodes", *J. Electrochem. Soc.* **154** (2007) A921-A928.

[5] V. Cumyn, M. Fleischauer, T. Hatchard, and J. Dahn, "Design and testing of a low-cost multichannel pseudopotentiostat for quantitative combinatorial electrochemical measurements on large electrode arrays", *Electrochemical and Solid-State Letters* **6** (2003) E15-E18.

[6] M. Fleischauer, T. Hatchard, G. Rockwell, J. Topple, S. Trussler, S. Jericho, M. Jericho, and J. Dahn, "Design and testing of a 64-channel combinatorial electrochemical cell", *J. Electrochem. Soc*. **150** (2003) A1465-A1469.

[7] M. Fleischauer and J. Dahn, "Combinatorial investigations of the Si-Al-Mn system for Li-ion battery applications", *J. Electrochem. Soc.* **151** (2004) A1216-A1221.

[8] M. Fleischauer, T. Hatchard, A. Bonakdarpour, and J. Dahn, "Combinatorial investigations of advanced Li-ion rechargeable battery electrode materials", *Measurement Science and Technology* **16** (2005) 212-220.

[9] S. Beattie and J. Dahn, "Combinatorial electrodeposition of ternary Cu–Sn–Zn alloys", *J. Electrochem. Soc*. **152** (2005) C542-C548.

[10] M. Winter and J. Besenhard, "Electrochemical lithiation of tin and tin-based intermetallics and composites", *Electrochim. Acta.* **45** (1999) 31-50.

[11] J. Maranchi, A. Hepp, and P. Kumta, "High capacity, reversible silicon thin-film anodes for lithium-ion batteries", *Electrochemical and Solid-State Letters* **6** (2003) A198-A201.

[12] J. Graetz, C. Ahn, R. Yazami, and B. Fultz, "Highly reversible lithium storage in nanostructured silicon", *Electrochemical and Solid-State Letters* **6** (2003) A194-A197.

[13] H. Jung, M. Park, Y. Yoon, G. Kim, and S. Joo, "Amorphous silicon anode for lithium-ion rechargeable batteries", *J. Power Sources* **115** (2003) 346-351

Chapter 4:

Combinatorial Studies of $Si_{1-x}O_x$ as a Potential Negative Electrode Material for Li-ion Battery Applications[1]

M. A. Al-Maghrabi, Junji Suzuki, R. J. Sanderson, V. L. Chevrier, R. A. Dunlap, and J. R. Dahn

4.1 Abstract

Thin films of $Si_{1-x}O_x$ were produced using combinatorial sputtering methods. X-ray diffraction studies of these films show that they are amorphous or nanostructured. The effect of oxygen content on the electrochemical performance of these materials was studied. The reversible specific capacity (between 0.005 and 0.9 V) agrees with the assumption that $Si_{1-x}O_x$ is made up of amorphous Si, which can react to form $Li_{3.75}Si$ and amorphous SiO_2, which reacts to form Li_4SiO_4. The irreversible capacity increases with oxygen content when measured to a potential limit of 0.9 V versus Li/Li^+ but further Li can be extracted from sites presumably near oxygen up to a potential of 2.0 V versus Li/Li^+. However, such potentials for the negative electrode would not be reached in a full Li-ion cell. This work shows that the oxygen content in $Si_{1-x}O_x$ should be optimized to produce materials with a reasonable active-inactive ratio in order to have electrodes with the desired specific capacity, an appropriate irreversible capacity and an appropriate amount of inactive phase to buffer volume expansion.

[1] This chapter was published in Journal of The Electrochemical Society, 160 (9) A1587-A1593 (2013).

4.2 Introduction

Carbon and/or graphite has been employed extensively as a negative electrode material in Li-ion batteries due to its low cost, abundance, long cycle life, appropriate voltage, and excellent conductivity [1-3]. However, the growing demands for high energy density storage devices that can be used in new generations of portable electronics, for example, has motivated researchers to consider alternatives to graphite, which has a limited specific capacity of 372 mAh/g. Si has the largest specific (3580 mAh/g) [4] and volumetric (8483 mAh/cc, before expansion) capacities among all known Li-storage materials and it has a low operating potential versus Li. However, the commercial use of pure Si anodes is hindered by their poor cycleability resulting from their huge volume expansion (up to 300 %). Realizing this problem, many studies have been undertaken to investigate the electrochemical behavior of Si-alloy anodes, which show high energy density and good safety characteristics [e.g. 5-6]. Beaulieu et al. [7-8] used *in situ* atomic force and optical microscopy to study the volume changes that occur during the lithiation and de-lithiation process of amorphous Si alloys. A homogeneous expansion was observed and 10-30 μm pieces of thin films expanded and contracted reversibly. Capacity loss occurs in electrodes of such amorphous alloys and was attributed to the fact that electrical contact is lost due to expanding and contracting particles undergoing large volume changes. Extensive work has been carried out during the last two decades to overcome this issue [e.g. 4, 9-10].

$Si_{1-x}O_x$, and in particular SiO, has been proposed as a promising electrode material among the Si-based systems, because of its high capacity and unique microstructure [11-13]. Different models have been presented to describe the microstructure of SiO. One of these models views the microstructure of SiO as consisting of nanometer regions of SiO_2 and nano-clusters of Si surrounded by a sub-oxide (SiO_x) matrix [14]. A study on the effects of heat treatment on SiO powder has shown that SiO disproportionates into amorphous Si and SiO_2 [15-16].

Miyachi et al. [17] have investigated the effect of metal-doping on the electrochemical performance of SiO negative electrode materials. Fe doping was found to be the best among the other studied metals.

The large irreversible capacity in the first cycle of SiO is considered one of the main drawbacks of this material. One possible cause of this irreversible capacity is the reaction of Li with oxygen in the suboxide matrix. Various studies have been reported which attempt to reduce the irreversible capacity. SiO anodes with C coating [15, 18] and silver coating [19] have been reported. The use of SiO as a negative electrode paired with a lithium-cobalt-manganese-nickel-oxide cathode was reported by Nagai et al. [20]. A 530 Wh/L capacity was obtained compared with 495 Wh/L for a conventional graphite/$LiCoO_2$ pair. Jeong et al. [21] studied the effect of a TiO_2 coating prepared using a facile sol-gel process on the electrochemical performance of SiO as anode material. The effect of binders and additives on the electrochemical performance of $Si_{1-x}O_x$ graphite electrodes were reported in [22].

One model which describes the lithiation process of SiO was reported [23], in which some of the Li is consumed by oxygen in the formation of Li_2O and this phase behaves as a buffering matrix to help accommodate volume expansion. The formation of Li_2O would cause the irreversible capacity and this would, therefore be inherent to SiO materials. An alternative model describing the lithiation mechanism of SiO-C composites was proposed by Yamada et al. [24]. They reported that as the electrode was lithiated, active lithium-silicon alloys (e.g.$Li_{15}Si_4$) form from the Si fraction of SiO and lithium silicates form from the SiO_2 fraction of the SiO. The active lithium-silicon particles are surrounded by the amorphous lithium silicates. However, in their study only a single composition was considered.

Here, $Si_{1-x}O_x$ binary thin films prepared by the combinatorial sputtering method are studied to determine the impact of oxygen content on the electrochemical properties, including the reversible and irreversible specific capacities. The oxygen

content in these combinatorial sputtered films varies continuously from about x = 0.1 to x = 0.4 for x in $Si_{1-x}O_x$.

4.3 Experimental Methods

To the best of our knowledge, this is the first combinatorial study of $Si_{1-x}O_x$. Our aim was to obtain a range of compositions in which both Si and O vary linearly in other to obtain a variety of Si to O ratios, ($Si_{1-x}O_x$. where $10 < x < 40$). Producing combinatorial films in this system with such a composition range was not a straightforward process, as we found that controlling the oxygen flux during the sputtering procedure was very difficult and did not follow the expected profile based on the mask geometry. Through our very detailed and careful experiments we have determined that a variety of sputtering parameters have significant impact on the deposition profile. These parameters include (1) the number of targets, (2) the thickness of the targets (i.e. the thinner the target the more magnetic field confinement around the target), (3) the sputtering time, (4) the sputtering pressure, (5) the rotational speed of the substrate table, and (6) the distance between the target and the substrate. A considerable effort was required to optimize the sputtering conditions with respect to the above-mentioned factors and obtain sputtered libraries with the desired compositin ranges. The electron microprobe determination of the composition of the sputtered films in this system also was difficult, as SiO_2 target is an insulator and the affects the analysis. Different standards were employed in order to calibrate the microprobe; particularly magnetite (Fe_3O_4) was found to be suitable for oxygen deterination. We found the optimum factors that yielded the desired compositions can be summarized as follows: a pressure 1 mT, the distance between the target and the samples should be as small as possible (less than 1 mm) and the use of a SiO_2 target rather than SiO.

Library closure is a routine that has been established here at Dalhousie University that enables us to confirm the results of the microprobe analysis. This

confirmation is based on the geometry of the masks used during sputtering as well as the mass measured by an accurate balance and is described in more detail in Section 4.4.1 of this thesis.

A combinatorial library of $Si_{1-x}O_x$ was produced using a Corona Vacuum Coaters model V3-T multi-target sputtering system as described in [25]. A base pressure of 2.3×10^{-7} Torr was achieved and moisture was eliminated from the chamber using a Polycold cryopump. The chamber pressure was maintained at 1 mTorr of argon gas during the depositions. The angular velocity of the sputtering table was 14 rpm to ensure atomic level mixing [25]. Continuous films on the 76 mm wide sputter track were deposited on a variety of substrates: Cu disks for mass determination, a Cu coated glass slide for compositional analysis, a Si (100) wafer for x-ray diffraction (XRD) measurements and a combinatorial cell plate for electrochemical testing. Two different sputtering targets, two inches in diameter, were used: a silicon target (99.99% pure) from Williams Advanced Materials and a silicon dioxide (SiO_2) target (99.995 % pure) from Kurt J Lesker. The desired deposition profile was achieved by using a "constant" and a "linear out" mask for the Si and SiO_2 targets, respectively. The distances between the masks and the substrates were kept extremely small (about 1 mm) in order to control the sputtering flux. A Sartorius SE-2 microbalance (0.1 μg precision) was used to determine the position-dependence of the mass per unit area of the sputtered materials. Thin film library compositions were determined using a JEOL-8200 Superprobe electron microprobe using wavelength dispersive spectroscopy (WDS) to verify that the intended composition range was achieved. The microprobe is equipped with a translation stage, which allowed the composition measurements to be matched with the results of other measurements. The microprobe was calibrated immediately before conducting the experiment using pure Si and Fe_3O_4 standards for Si and O, respectively. The uncertainty of the composition is about ± 2 %. A Bruker D-8 Discover diffractometer equipped with a Vantec-2000 area detector and a Cu target x-ray tube was used for the XRD measurements.

For electrochemical testing of the combinatorial library, a 64-electrode electrochemical cell plate based on a printed circuit board was used [26]. A combinatorial electrochemical cell was constructed as described by Fleischauer et al. [27]. Two different kinds of separators were used in the combinatorial electrochemical cell: a Celgard 2300 microporous film and a polypropylene blown micro fiber (BMF) separator (available from 3M Company). The microporous film was placed in contact with the Li foil and the BMF contacted the $Si_{1-x}O_x$ combinatorial cell plate. This combination of separators provides uniform pressure on each of the 64 electrodes. 1 M $LiClO_4$ ethylene carbonate: Diethyl carbonate (EC: DEC, 1:2 by volume) electrolyte was applied. This approach has provided a highly efficient method of testing the composition dependence of the electrochemical properties of potential Li-ion battery electrode materials, particularly those for use as negative electrodes [28]. Slow scan cyclic voltammetry measurements were performed on the 64 electrodes of the cell plate using a multichannel pseudopotentiostat as described by Cumyn et al. [29]. The voltage window was between 2.0 and 0.005 V. Differential capacity (dQ/dV) versus voltage (V) was then estimated by dividing the current (dQ/dt) by the sweep rate (dV/dt). The scan time was 12 hours for each discharge or charge during the first three cycles.

4.4 Results and Discussion

4.4.1 Compositional and Structural Analysis

Figure 4.1 shows that the compositions as obtained from microprobe analysis were confirmed by "library closure" [28]. Figure 4.1 shows the composition and mass per unit area of the sputtered library as a function of position along the

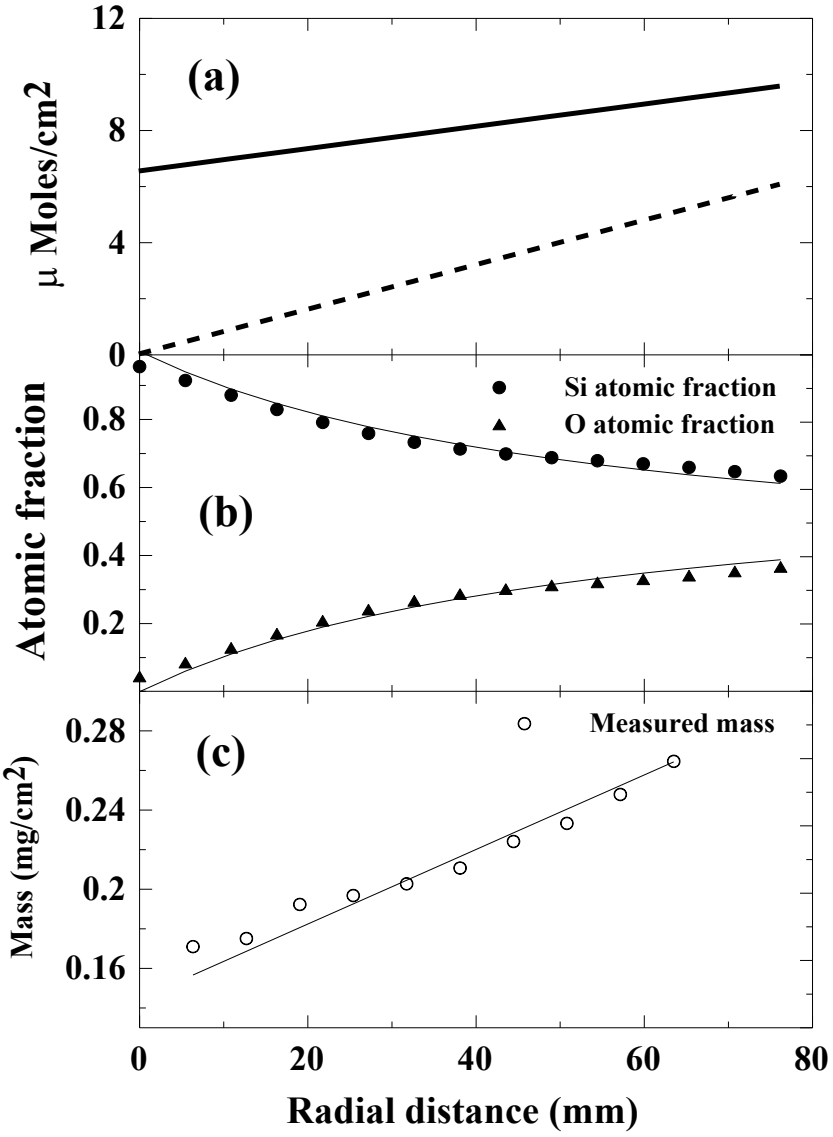

Figure 4.1: A "library closure". (a) The moles per unit area of Si (continuous line) and O (dashed line) defined by "constant" and "linear out" sputtering masks, respectively, (b) Composition calculated from curves in (a) (solid lines) are shown to agree well with and the measured compositions from wavelength dispersive spectroscopy (WDS) (data points), and (c) The measured mass of the sputtered films on each weighing disk (open circles) and that calculated from the curves in (a) (solid line) for the $Si_{1-x}O_x$ library.

sputtered library as a function of position along the sputtering track. Figure 4.1(a) shows the calculated moles of Si and oxygen per unit area, as defined by the "constant" and "linear out" sputtering masks, respectively. The observed gradient in the number of moles of Si results from the contribution of: (1) a constant amount of Si sputtered through the "constant" mask and (2) a gradient of Si resulting from sputtering the SiO_2 target through the "linear out mask". Figure 4.1(b) shows that the compositions calculated from Figure 4.1(a), based on the calculated moles per unit area, agree well with the compositions measured by the microprobe. Figure 4.1(c) compares the measured mass of the sputtered films on each weigh disk with the calculated mass from the curves in Figure 4.1(a) for the sputtered library and illustrates that the measured compositions are consistent with the expected compositions based on mask geometry. Thus, the combinatorial library is reliable and well-characterized from a composition versus position standpoint.

Figure 4.2 shows x-ray diffraction patterns of selected compositions across the sputtered film. Oxygen content increases from the top of the figure to the bottom. Films with the low oxygen content represent a typical pattern of amorphous or nanostructured sputtered Si, as a broad hump is observed at $2\theta = 28^{o}$. As the oxygen content increases, the structure remains amorphous.

4.4.2 Electrochemical Studies

Figure 4.3 shows the computed Li-Si-O phase diagram of obtained from the publicly available materials project [30-32]. In this study, the starting material is on the line in Figure 4.3 joining Si and O. In equilibrium, if the phase diagram is correct, the lithiation process occurs along the dashed line (represented by two segments). Along the red segment of the dashed line, lithiation of SiO_2 starts and different phases of lithium silicate form (occurs at higher potential relative to pure

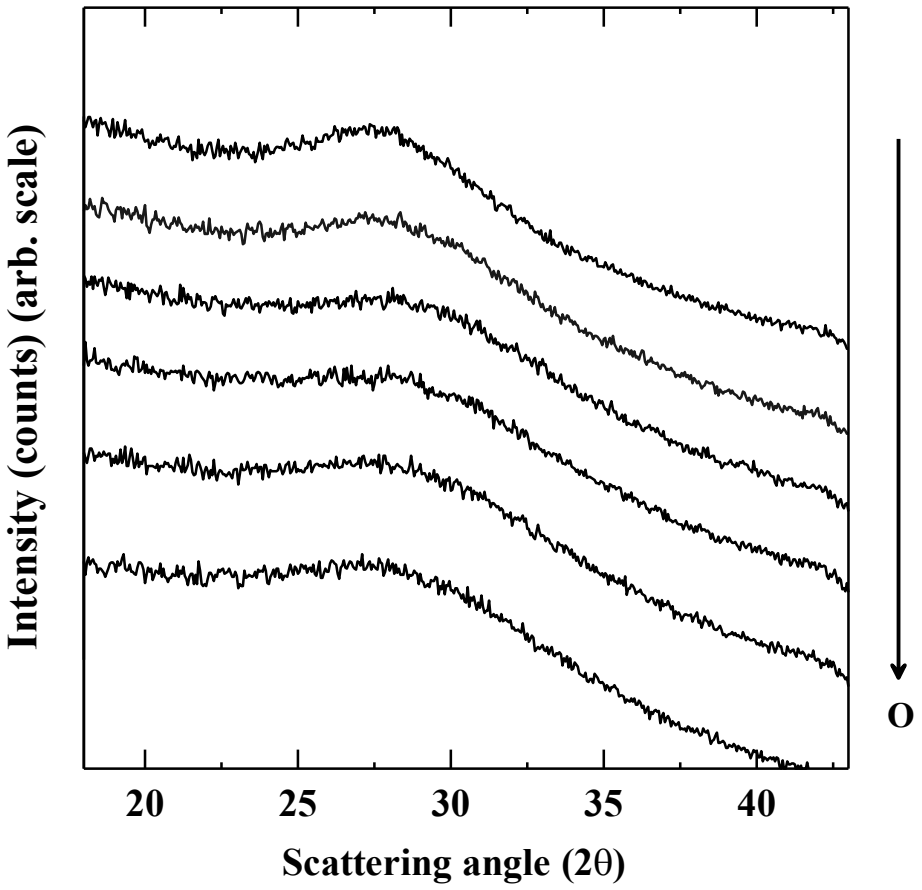

Figure 4.2: Selected room temperature Cu-K_α x-ray diffraction patterns of $Si_{1-x}O_x$. Oxygen content increases from the top to the bottom of the figure.

Si). This lithiation process proceeds till Li_4SiO_4 is formed. Then along the blue segment of the dashed line in Figure 4.3, lithiation of Si takes place ultimately forming the $Li_{13}Si_4$ phase. The blue segment intersects with the co-existence line between $Li_{13}Si_4$ and Li_4SiO_4, suggesting that the two phases are present at the end of the first lithiation. It has been shown that $Li_{15}Si_4$ is the limit of lithiation of Si at room temperature [4], but the $Li_{15}Si_4$ phase is not shown on the phase diagram of Figure 4. 3. We assume that a tie line connects $Li_{15}Si_4$ to Li_4SiO_4. If this is the case, then the impact of the structure of the phase diagram in Figure 4.3 on the irreversible and reversible capacity of $Si_{1-x}O_x$ can be considered.

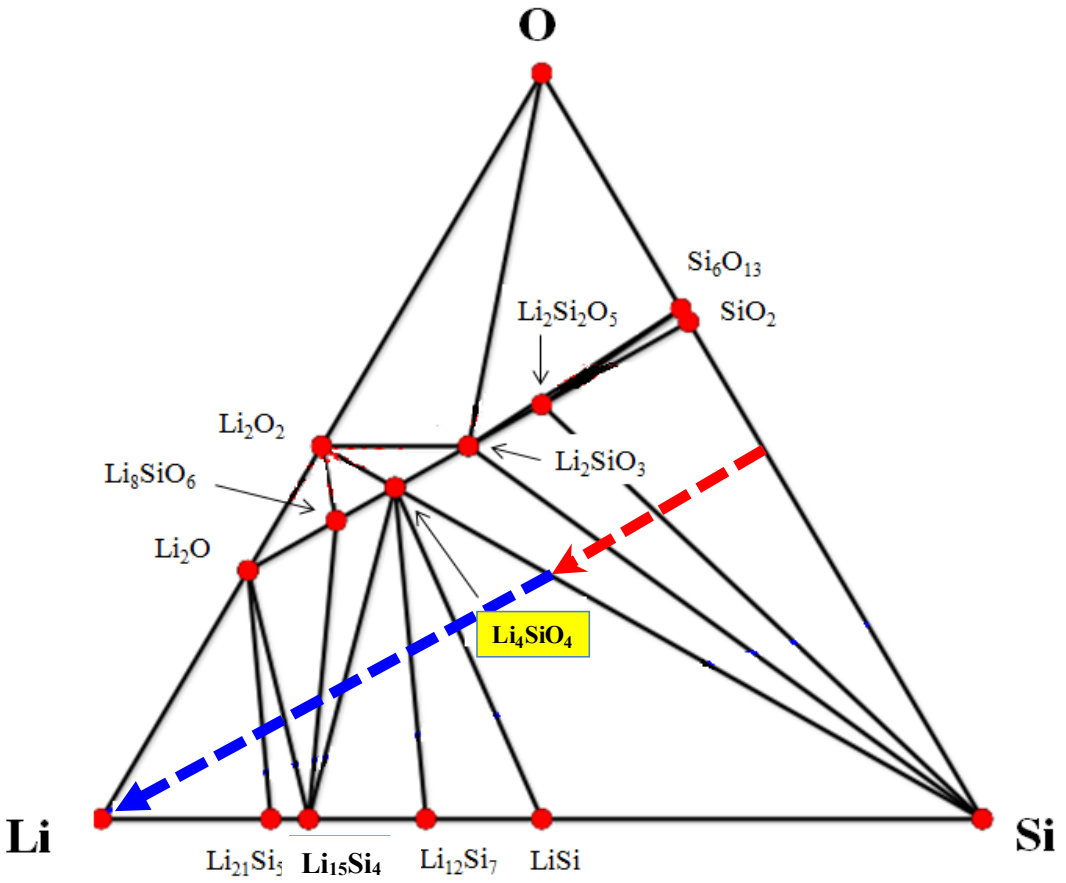

Figure 4.3: Li-Si-O ternary phase diagram adapted from the publicly available materials project [29–32]. The region of interest for this study is shown along the dashed line.

Figure 4.4 shows the potential versus specific capacity for the 64 electrodes of the combinatorial electrochemical cell made from the sputtered films. The variation of Si and oxygen content is indicated by the arrow at the top of the figure. As the radial distance from the center of the sputtering table changes only slightly along each column in Figure 4.4, each column corresponds to cells with approximately constant Si and O content. Figure 4.4 illustrates the general trends in the electrochemical properties that exist in the material as a function of oxygen content.

Figure 4.5 shows the differential capacity (dQ/dV) versus potential plots as a function of composition for eight selected electrodes across the sputtered library (i.e. data from row 3 of Figure 4.4). The first three cycles are plotted in this figure in order to illustrate the response of the electrode material to subsequent lithiations. The first cycle is represented by the dashed line (red), whereas the two subsequent cycles are shown by solid lines (blue). The oxygen content in the film increases from 5(a) to (h). Figure 4.5(a) shows the results for the electrode with the minimum oxygen content. During the first discharge (Li insertion), the profile of the differential capacity has the characteristic features of amorphous Si with an additional peak at ~ 0.35 V as indicated in the figure by the location of the vertical dashed line. Close inspection of the position of this peak shows that it shifts to a higher potential value across the film as the oxygen content increases, Figure 4.5(b) through (f). This additional peak is probably due to the reaction of Li with SiO_2 nano regions to, presumably, form different lithium silicate phases according to the phase diagram in Figure 4.3. As the Li content in the electrodes increases, the overall electrode composition moves first along the red-dashed line in Figure 4.3(a) and Li_4SiO_4 is created. The area under this ~0.35 V peak in dQ/dV increases with oxygen content as expected based on the phase diagram in Figure 4.3. Once the oxygen content reached a certain value, x = 0.3, the potential of the peak did not shift further. The other peaks, which appeared at ~ 0.2 and ~ 0.05 V during discharge and at ~ 0.35 and ~ 0.45 V during charge, are identical to those of amorphous Si electrodes [4]. Figure 4.5 shows that when the oxygen content

exceeds x = 0.2, the dQ/dV profiles exhibit a tail during charge that extends to voltages higher than 1.1 V.

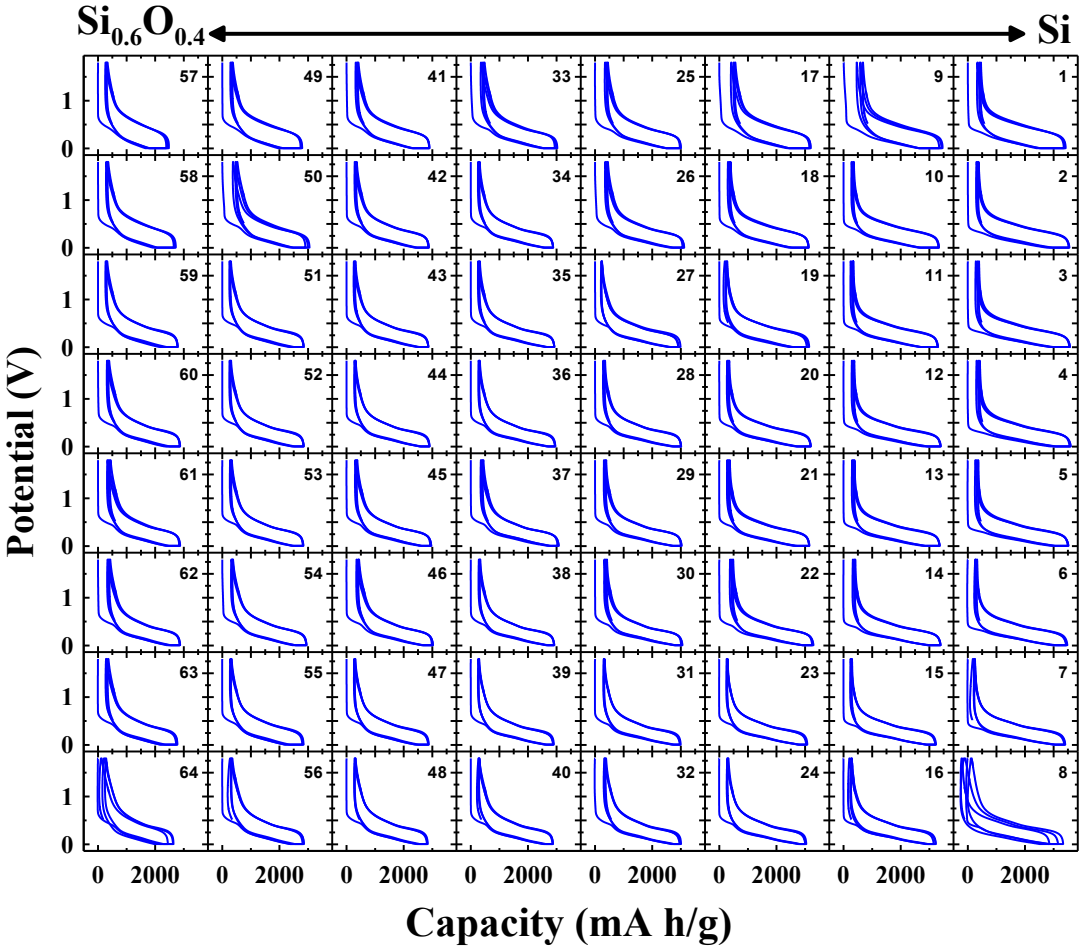

Figure 4.4: Potential versus capacity for the combinatorial cell made from the sputtered library. The voltage limits are 0.005 to 2 V. Data are shown for the first three cycles. Variation in composition is indicated. The horizontal direction in the figure corresponds to the radial direction on the sputtering table and represents the direction of the composition gradient. The vertical direction in the figure corresponds to columns of cells with approximately the same composition.

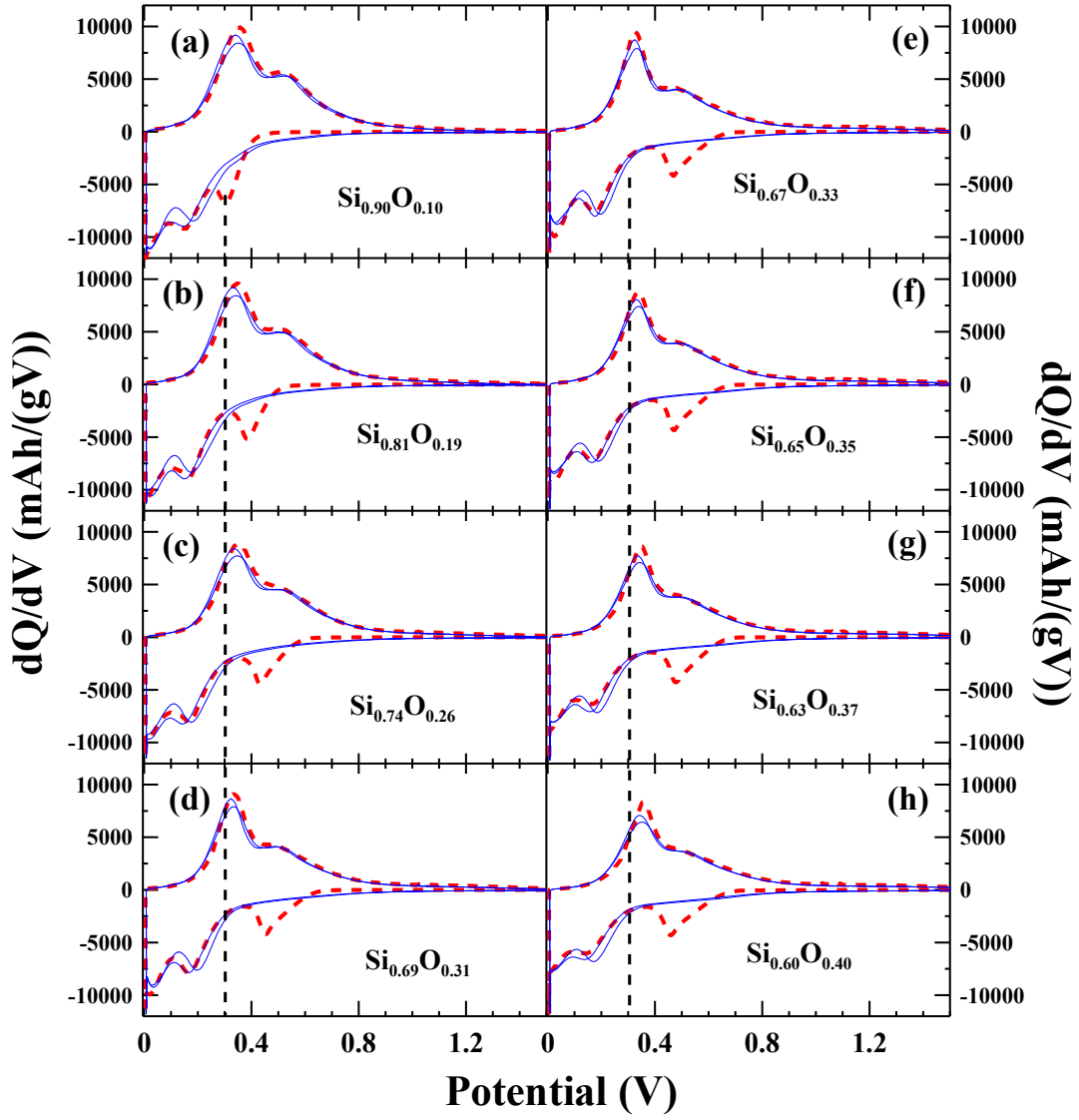

Figure 4.5: dQ/dV versus V plots for the first three cycles for eight electrodes. The oxygen content increases from (a) to (h); dashed line (red) for first cycle, continuous line (blue) for second and third cycles.

The magnitude of this tail increases as a function of oxygen content suggesting that Li is being removed from positions near oxygen in this potential range. After the first cycle, the reduction peak at about 0.35 V disappears due to the fact that the initial reaction with sites near oxygen took place in the first cycle. However, this does not mean that Li is unable to react again with these sites near oxygen during the second cycle. Figure 4.6(a) shows a comparison of the differential capacity for the second cycle of two electrodes from Figures 4.5(a) and (h). For the film with more oxygen, there is enhanced discharge capacity near 0.6 V which is believed to be due to reaction of Li with sites near oxygen. This capacity exists because some Li was extracted from these sites near oxygen during the previous charge (extracting Li) to 2.0 V. If the charge is limited to 1.2 V, this extra discharge capacity near 0.6 V does not appear in samples with high oxygen contents (Figure 4.6(b)). This reaction does show voltage hysteresis due to bond breaking and reformation.

Figure 4.7 shows the potential versus capacity curves for the first three cycles for eight selected compositions across the sputtered library where the oxygen content increases from panels (a) to (h). In general, the voltage curves are smooth and show a single sloping plateau during the first discharge indicating the presence of a single phase region, as expected for amorphous Si electrodes [26]. Such amorphous structures expand and contract homogenously during the lithiation process [7], which may enhance the stability of these electrodes. The first lithiation capacity for this composition shown in Figure 7(a) is ~ 3450 mAh/g; slightly less than expected for pure Si at room temperature as a small amount of oxygen is present. The first delithiation capacity for this composition was 3220 mAh/g. As the oxygen content increases across the film a plateau appeared during the first discharge at about 0.4 to 0.55 V as is consistent with Figure 4.5.

Figure 4.8 summarizes the electrochemical performance (lithiation, delithiation and irreversible capacity) of the eight different electrodes first presented in Figures 4.5 and 4.7.

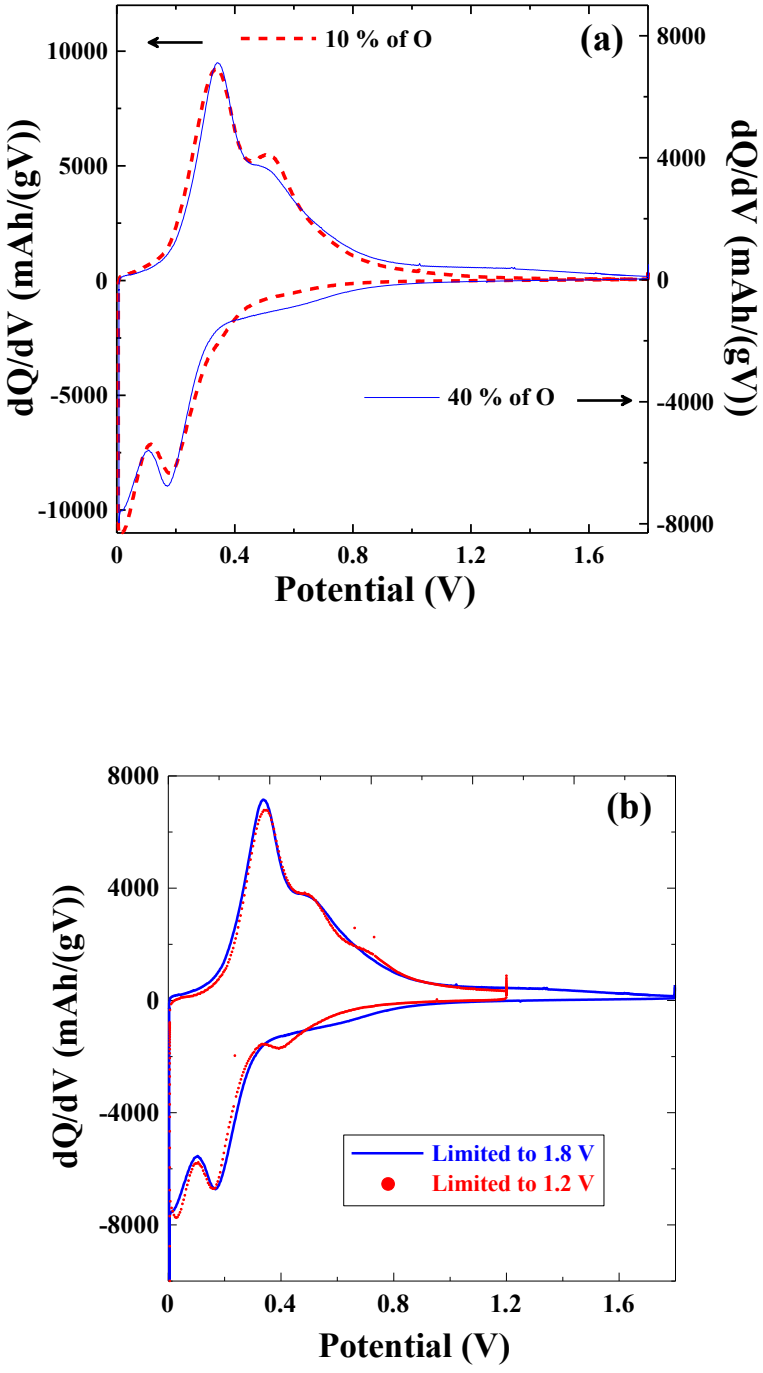

Figure 4.6: (a) dQ/dV versus V plots for two electrodes of $Si_{1-x}O_x$. The dashed line (red) is for $x \sim 0.1$ (left) and continuous line (blue) is for $x \sim 0.4$ (right) and (b) dQ/dV versus V plots for two electrodes of $Si_{1-x}O_x$ with 40% oxygen content and cycled up to two different cut-off voltages.

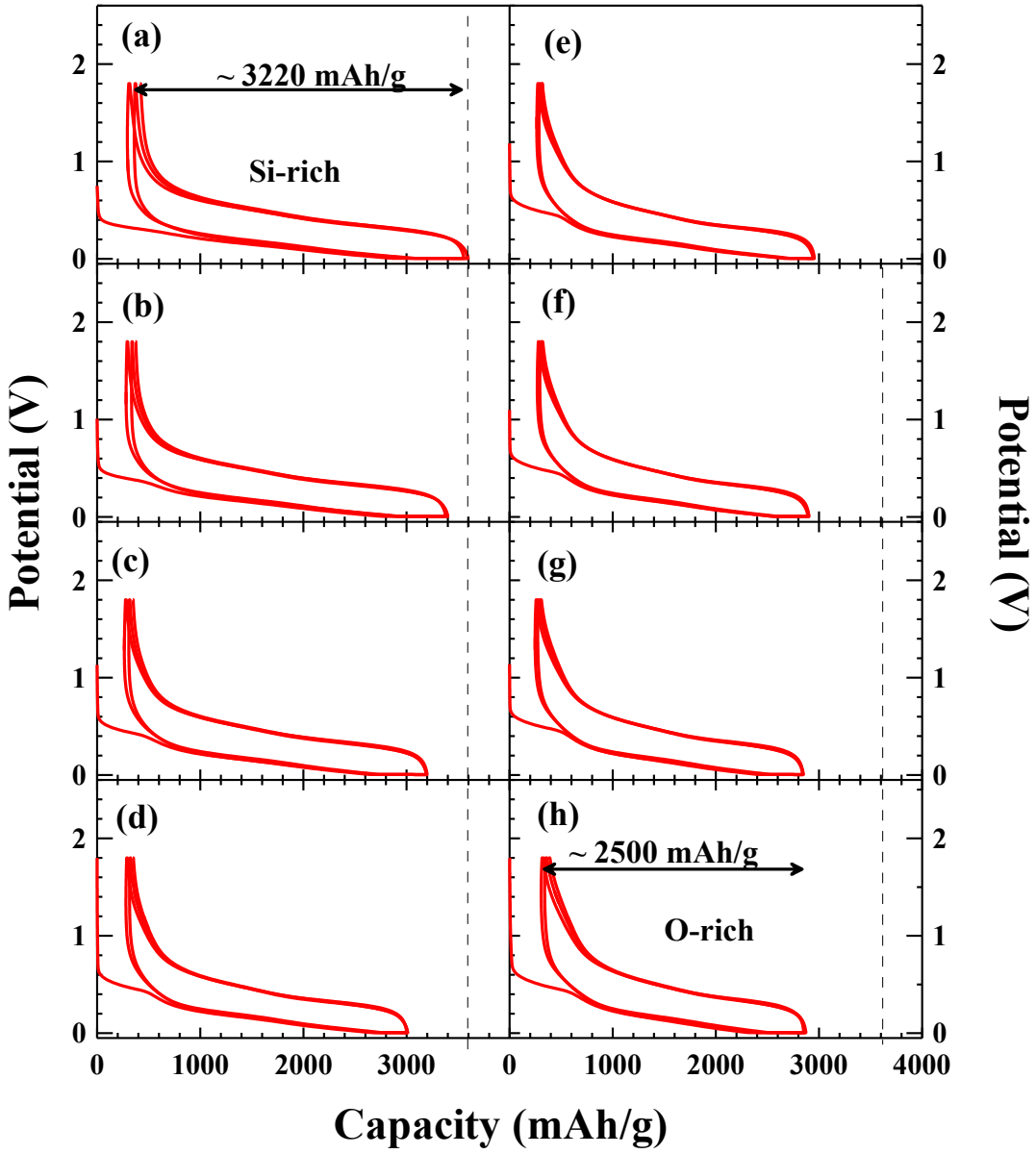

Figure 4.7: Potential versus capacity for eight different electrodes. The voltage limits are 0.005 to 2 V. Data are shown for the first three cycles. Oxygen content increases from (a) to (h). The vertical dashed lines are described in the text.

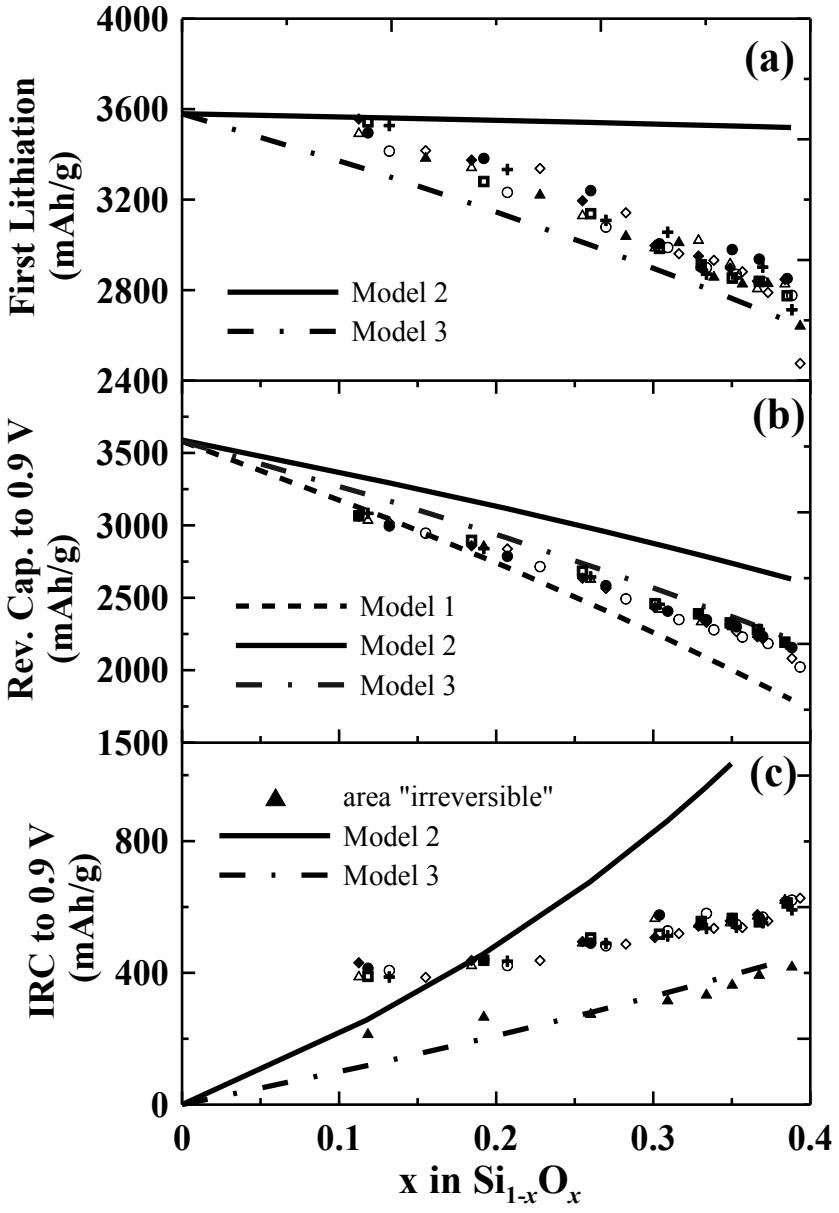

Figure 4.8: (a) first discharge capacity for 64-electrodes shown in Figure 4.4. Solid and dashed lines represent the prediction of Model 2 and 3, respectively. Data points (circles, diamonds…etc) are the experimental data from all rows in Figure 4.4; (b) Reversible capacity (first charge) to 0.9 V as a function of oxygen content Dashed and solid lines represent the prediction from Models 1 to 3 as discussed in the text for the same electrodes shown in panel (a); and (c) irreversible capacities to 0.9 V for the same electrodes as shown in panel (a) and (b). The solid triangles represent the integrated area under the first peak during first discharge, the solid and dashed lines represent the predictions of Models 2 and 3, respectively.

In order to illustrate the reproducibility of the data, additional data, representing all 8 rows from Figure 4.4, are included. Three different models are proposed to consider the measured data. These models can be summarized as follows:

(1) This model gives the expected reversible capacity based on the assumption that $Si_{1-x}O_x$ is made up of nanometer scale regions of active Si (3.75 Li/Si) and inactive SiO_2. Both the first lithiation capacity and the reversible capacity based on this model are:

$$capacity\ \left(\text{mAh/g}\right)=\frac{3.75\cdot\left(1-3x/2\right)}{\left(1-x\right)\cdot molar\,mass_{Si}+\left(x\right)\cdot molar\,mass_{o}}\cdot\frac{96500\,\text{C/mole}}{3.6\,\text{C/mAh}} \qquad (4.1)$$

(2) Model 2 assumes that all the Si, even that initially bonded to oxygen, is active (3.75 Li/Si) and results in the formation of Li_2O after the first lithiation. However, the formation of Li_2O is an irreversible process. The first lithiation capacity based on Model 2 is:

$$capacity\ \left(\text{mAh/g}\right)=\frac{3.75\cdot\left(1-x\right)+2\cdot\left(x\right)}{\left(1-x\right)\cdot molar\,mass_{Si}+\left(x\right)\cdot molar\,mass_{o}}\cdot\frac{96500\,\text{C/mole}}{3.6\,\text{C/mAh}} \qquad (4.2)$$

The reversible capacity (to 0.9 V) based on this model is:

$$capacity\ \left(\text{mAh/g}\right)=\frac{3.75\cdot\left(1-x\right)}{\left(1-x\right)\cdot molar\,mass_{Si}+\left(x\right)\cdot molar\,mass_{o}}\cdot\frac{96500\,\text{C/mole}}{3.6\,\text{C/mAh}} \qquad (4.3)$$

and the irreversible capacity (to 0.9 V) is:

$$capacity\ \left(\text{mAh/g}\right)=\frac{2(x)}{\left(1-x\right)\cdot molar\,mass_{Si}+\left(x\right)\cdot molar\,mass_{o}}\cdot\frac{96500\,\text{C/mole}}{3.6\,\text{C/mAh}} \qquad (4.4)$$

(3) Model 3 assumes that after the first lithiation, the whole structure can be viewed as nanometer scale regions of active Si (3.75 Li/Si) and Li_4SiO_4. However, we

assume Li cannot be extracted from Li_4SiO_4 below 0.9 V. The first lithiation capacity based on Model 3 is:

$$capacity\ (\text{mAh/g}) = \frac{3.75\cdot(1-5x/4)+x}{(1-x)\cdot molar\ mass_{Si}+(x)\cdot molar\ mass_{o}}\cdot\frac{96500\,\text{C/mole}}{3.6\,\text{C/mAh}} \qquad (4.5)$$

The reversible capacity (to 0.9 V) based on this model is:

$$capacity\ (\text{mAh/g}) = \frac{3.75\cdot(1-5x/4)}{(1-x)\cdot molar\ mass_{Si}+(x)\cdot molar\ mass_{o}}\cdot\frac{96500\,\text{C/mole}}{3.6\,\text{C/mAh}} \qquad (4.6)$$

and the irreversible capacity (to 0.9 V) is:

$$capacity\ (\text{mAh/g}) = \frac{x}{(1-x)\cdot molar\ mass_{Si}+(x)\cdot molar\ mass_{o}}\cdot\frac{96500\,\text{C/mole}}{3.6\,\text{C/mAh}} \qquad (4.7)$$

Figure 4.8(a) shows that the first lithiation capacity (data points representing the 8 rows of Figure 4.4) declines as a function of oxygen content. There is less active Si and some additional capacity due to the reaction of Li with sites near oxygen. Figure 4.8(a) also includes two calculated curves. The first curve (solid) is for the first lithiation capacity of Model 2 given by Eq. 2 and the other curve (dashed) is for the first lithiation capacity of Model 3 given by Eq. 5.The prediction of Model 3 matches the data in Figure 4.8(a) very well, apart from a constant offset presumably caused by the small irreversible capacity of the Ni electrode pads, which suggests that the general structure of the phase diagram in Figure 4.3 is appropriate to describe the lithiation of $Si_{1-x}O_x$.

Figure 4.8(b) shows the reversible specific capacity measured from the first delithiation between 0.005 and 0.9 V. Figure 4.8(b) also shows three calculated reversible specific capacity curves based on the three proposed models, Eqs.1, 3 and

6, respectively. Figure 4.8(b) shows that Model 3 agrees well with the measured reversible capacity, suggesting that the sputtered $Si_{1-x}O_x$, after the first lithiation, becomes a mixture of nanometer scale regions of active Si (3.75 Li/Si) and Li_4SiO_4.

Figure 4.8(c) shows the irreversible capacity measured to a potential of 0.9 V during the first charge (extraction of Li) plotted versus the oxygen content. The potential of 0.9 V was selected for two reasons. First, the data in Figure 4.5 suggests the capacity due to Li extracted from sites near oxygen is predominantly above 0.9 V and, second, because the negative electrode in a practical Li-ion cell would probably never reach a potential greater than 0.9 V versus Li/Li^+ even if the Li-ion cell were fully discharged. Figure 4.8(c) also shows the integrated area under the "irreversible" peak in Figure 4.5 (triangles), which is believed to be associated with the first reaction of Li with these sites near oxygen, and some Si, to form Li_4SiO_4. Figure 4.8(c) also shows the predicted irreversible capacities based on Model 2 (solid line) and Model 3 (dashed line). An excellent agreement was obtained between the integrated area and the prediction of Model 3 while Model 2 was unable to describe the data. Figure 4.8(c) shows that the measured irreversible capacity and the area under the irreversible peak in Figure 4.5 have a constant offset. The constant offset can be explained based on the amount of Li irreversibly lost to the Ni electrode contact. Our previous work, [26], showed that the irreversible capacity of the sputtered Si is about ~ 2 % and this was interpreted to be caused by some Li reacting with the thin NiO layer on the top of the Ni electrode pads. Taking this into consideration in the interpretation of the data in Figure 4.8(c), there is very good agreement between the measured irreversible capacity and the integrated area under the "irreversible" peak in Figure 4.5.

4.5 Conclusions

XRD results showed that sputtered $Si_{1-x}O_x$is a nanostructured or amorphous mixture of Si and SiO_2. The measured reversible specific capacity, irreversible

capacity and first lithiation capacity are consistent with the structure of the computed Li-Si-O ternary phase diagram. Li reacts first with the SiO_2 portion to ultimately form Li_4SiO_4 and then reacts with the Si portion to form $Li_{15}Si_4$ [$Li_{15}Si_4$ is not shown in the equilibrium phase diagram, however]. The amount of Li_4SiO_4 formed increases as a function of x in $Si_{1-x}O_x$ leading to an increase in irreversible capacity measured to 0.9 V as it appears Li cannot be removed from Li_4SiO_4 to this potential. The Li_4SiO_4 phase may play two roles: (1) it may enhance the diffusion of Li atoms into the nano Si phase by creating numerous grain boundaries [24] and (2) it buffers some of the volume expansion as Si particles are lithiated. The differential capacity plots did not reveal any major structural changes during cycling, indicating the amorphous nature of these alloys. The major message of this work is that increasing the oxygen content in $Si_{1-x}O_x$ leads to an increase in irreversible capacity, but the creation of the Li_4SiO_4 inactive phase may help improve cycling by buffering volume change. Thus it is important to optimize the oxygen content in such materials.

Acknowledgments

The authors acknowledge funding from NSERC and 3M Canada Co. under the auspices of the Industrial Research Chairs Program. We also acknowledge the support of the Canada Foundation for Innovation, the Atlantic Innovation Fund and other partners that fund the Facilities for Materials Characterization managed by the Institute for Research in Materials.

4.6 References

[1] T. Nagaura and K. Tozawa, "Lithium ion rechargeable battery", *Prog. Batteries Solar Cells* **9** (1990) 209-214.

[2] T. Reddy and D. Linden, "Linden's Handbook of Batteries", McGraw-Hill, New York (2011).

[3] M. Yoshio, R. Brodd, and A. Kozawa, "Lithium-ion Batteries Science and Technologies", Springer, New York (2009).

[4] M. Obrovac and L. Christensen, "Structural changes in silicon anodes during lithium insertion/extraction", *Electrochemical and Solid-State Letters* **7** (2004) A93-A96.

[5] H. Ahn, Y. Kim, K. Park, and T. Seong, "Use of Sn–Si nanocomposite electrodes for Li rechargeable batteries", *Chem. Commun.* (2005) 43-45.

[6] O. Mao, R. Turner, I. Courtney, B. Fredericksen, M. Buckett, L. Krause, and J. Dahn, "Active/Inactive nanocomposites as anodes for Li−Ion batteries", *Electrochemical and Solid-State Letters* **2** (1999) 3-5.

[7] L. Beaulieu, K. Eberman, R. Turner, L. Krause, and J. Dahn, "Colossal reversible volume changes in lithium alloys", *Electrochemical and Solid-State Letters* **4** (2001) A137-A140.

[8] L. Beaulieu, T. Hatchard, A. Bonakdarpour, M. Fleischauer, and J. Dahn, "Reaction of Li with alloy thin films studied by *in situ* AFM", *J. Electrochem. Soc.* **150** (2003) A1457-A1464.

[9] H. Lee, Y. Kim, M. Hong, and S. Lee, "Carbon-coated $Ni_{20}Si_{80}$ alloy–graphite composite as an anode material for lithium-ion batteries", *J. Power Sources* **141** (2005) 159-162.

[10] T. Hatchard, M. Obrovac, and J. Dahn, "Electrochemical reaction of the Si_{1-x} Zn_x binary system with Li", *J. Electrochem. Soc*. **152** (2005) A2335-A2344.

[11] Y. Hwa, C. Park, and H. Sohn, "Modified SiO as a high performance anode for Li-ion batteries", *J. Power Sources* (2012).

[12] K. Kim, J. Park, S. Doo, and T. Kim, "Effect of oxidation on Li-ion secondary battery with non-stoichiometric silicon oxide (SiO_x) nanoparticles generated in cold plasma", *Thin Solid Films* **518** (2010) 6547-6549.

[13] J. Wang, H. Zhao, J. He, C. Wang, and J. Wang, "Nano-sized SiO_x/C composite anode for lithium ion batteries", *J. Power Sources* **196** (2011) 4811-4815.

[14] A. Hohl, T. Wieder, P. Van Aken, T. Weirich, G. Denninger, M. Vidal, S. Oswald, C. Deneke, J. Mayer, and H. Fuess, "An interface clusters mixture model for the structure of amorphous silicon monoxide (SiO)", *J. Non Cryst. Solids* **320** (2003) 255-280.

[15] C. Park, W. Choi, Y. Hwa, J. Kim, G. Jeong, and H. Sohn, "Characterizations and electrochemical behaviors of disproportionated SiO and its composite for rechargeable Li-ion batteries", *Journal of Materials Chemistry* **20** (2010) 4854-4860.

[16] M. Mamiya, H. Takei, M. Kikuchi, and C. Uyeda, "Preparation of fine silicon particles from amorphous silicon monoxide by the disproportionation reaction", *J. Cryst. Growth* **229** (2001) 457-461.

[17] M. Miyachi, H. Yamamoto, and H. Kawai, "Electrochemical properties and chemical structures of metal-doped SiO anodes for Li-ion rechargeable batteries", *J. Electrochem. Soc.* **154** (2007) A376-A380.

[18] C. Guo, D. Wang, Q. Wang, B. Wang, and T. Liu, "A SiO/graphene nanocomposite as a high stability anode material for lithium-ion batteries", *Int. J. Electrochem. Sci*. **7** (2012) 8745-8752.

[19] J. Lee and S. Park, "High-performance porous silicon monoxide anodes synthesized via metal-assisted chemical etching", *Nano Energy* **2** (2013) 146-152.

[20] R. Nagai, F. Kita, and M. Yamada, "Development of highly reliable high-capacity batteries for mobile devices and small-to medium-sized batteries for industrial applications", *Energy* **450** (2003) 350-358.

[21] G. Jeong, J. Kim, Y. Kim, and Y. Kim, "Multifunctional TiO_2 coating for a SiO anode in Li-ion batteries", *Journal of Materials Chemistry* **22** (2012) 7999-8004.

[22] A. Guerfi, P. Charest, M. Dontigny, J. Trottier, M. Lagace, P. Hovington, A. Vijh, and K. Zaghib,"SiO_x–graphite as negative for high energy Li-ion batteries", *J. Power Sources* **196** (2011) 5667-5673.

[23] Y. Nagao, H. Sakaguchi, H. Honda, T. Fukunaga, and T. Esaka, "Structural analysis of pure and electrochemically lithiated SiO using neutron elastic scattering", *J. Electrochem. Soc*. **151** (2004) A1572-A1575.

[24] M. Yamada, A. Inaba, A. Ueda, K. Matsumoto, T. Iwasaki, and T. Ohzuku, "Reaction mechanism of "SiO"-carbon composite-negative electrode for high-capacity lithium-ion batteries", *J. Electrochem. Soc.* **159** (2012) A1630-A1635.

[25] J. Dahn, S. Trussler, T. Hatchard, A. Bonakdarpour, J. Mueller-Neuhaus, K. Hewitt, and M. Fleischauer, "Economical sputtering system to produce large-size composition-spread libraries having linear and orthogonal stoichiometry variations", *Chemistry of Materials* **14** (2002) 3519-3523.

[26] M. Al-Maghrabi, N. van der Bosch, R. Sanderson, D. Stevens, R. Dunlap, and J. Dahn, "A new design for a combinatorial electrochemical cell plate and the inherent irreversible capacity of lithiated silicon", *Electrochemical and Solid-State Letters* **14** (2011) A42-A44.

[27] M. Fleischauer, T. Hatchard, G. Rockwell, J. Topple, S. Trussler, S. Jericho, M. Jericho, and J. Dahn, "Design and testing of a 64-channel combinatorial electrochemical cell", *J. Electrochem. Soc.* **150** (2003) A1465-A1469.

[28] M. Al-Maghrabi, J. Thorne, R. Sanderson, J. Byers, J. Dahn, and R. Dunlap, "A combinatorial study of the Sn-Si-C system for Li-ion battery applications", *J. Electrochem. Soc.* **159** (2012) A711-A719.

[29] V. Cumyn, M. Fleischauer, T. Hatchard, and J. Dahn, "Design and testing of a low-cost multichannel pseudopotentiostat for quantitative combinatorial electrochemical measurements on large electrode arrays", *Electrochemical and Solid-State Letters* **6** (2003) E15-E18.

[30] A. Jain, G. Hautier, S. Ong, C. Moore, C. Fischer, K. Persson, and G. Ceder, "Formation enthalpies by mixing GGA and GGA U calculations", *Physical Review B* **84** (2011) 1-10

[31] S. Ping Ong, L. Wang, B. Kang, and G. Ceder, "Li−Fe−P−O_2 phase diagram from first principles calculations", *Chemistry of Materials* **20** (2008) 1798-1807.

Chapter 5:

A Combinatorial Study of the Sn-Si-C System for Li-Ion Battery Applications[1]

M. A. Al-Maghrabi, J. S. Thorne, R. J. Sanderson, J. N. Byers, J. R. Dahn and R. A. Dunlap

5.1 Abstract

In the present work three pseudobinary libraries of the Sn-Si-C system were produced using combinatorial methods. X-ray diffraction was used to study the structure of these libraries and Mössbauer spectroscopy was employed to probe the atomic environment. Cyclic voltammetry measurements were performed using a multichannel pseudopotentiostat to study the behavior of these materials as negative electrodes for Li-ion batteries. These three libraries were compared in terms of the phases formed, amorphous versus crystalline structure, the reversible capacity as a function of composition and the capacity retention. The addition of C to Sn-Si inhibits the aggregation of Sn into regions of relatively pure Sn. This minimization of free Sn has the effect of improving cycleability by reducing the adverse effects of volume expansion, by eliminating two-phase coexistence regions during delithiation and lithiation.

[1] This chapter was published in Journal of The Electrochemical Society, 159 (6) A711-A719 (2012).

5.2 Introduction

Lithium ion (Li-ion) batteries are very popular and considered a good choice for energy in mobile applications such as laptops, phones, and transportation [1] because they offer numerous advantages [2], including excellent performance and long charge-discharge cycle life. In the 1990s, Sony commercialized the first Li-ion battery. Since then, graphite, which provides good cycle life, has been the most common negative electrode material used in these batteries [3-4]. Graphite has a theoretical specific capacity of 372 mAh/g for LiC_6 [5]. This capacity can be a limiting factor for use in portable devices and indicates the need to develop new advanced anode materials that are commercially viable. Thus, in recent years there has been considerable research into the development of metal-based negative electrode materials for Li-ion batteries.

Different binary lithium-metal systems, including Li_xSi [6] and Li_xSn have been the subject of investigation. Sn and Si [7] can form $Li_{4.4}Sn$ and $Li_{3.75}Si$ phases to store 994 and 3580 mAh/g, respectively, providing much higher capacities than obtained from C [8]. Electrodes synthesized from pure Sn are generally considered in appropriate because of large undesired capacity loss during the first few cycles. In the case of Sn, the coexistence of crystalline Li_xSn phases of different volume per Sn atom leads to electrode pulverization and loss of electrical contact [9–12]. There have been promising results for electrodes prepared from pure Si, since Li_xSi becomes amorphous during the first reaction with Li and then particles expand homogeneously, hence undergoing reversible cycling with minimal capacity loss [12]. However, the volume change associated with the lithiation of Si is over 270% and it is very hard to design practical electrodes that can accommodate such large volume changes without capacity loss. One possible way to overcome capacity loss is to surround nanometer-sized active material grains, which react reversibly with lithium, with an inactive matrix to make an active-inactive nanocomposite that limits the overall volume expansion of the nanocomposite particle [11, 13, 14–16].

Ahn et al. [16] have reported that a nanostructured $Si_{1-x}Sn_x$ thin film sputtered onto Cu foil can have a capacity between 700 and 870 μAh cm^{-2} μm^{-1} (Figure 2 in reference 16) with an irreversible capacityof 27–33% in the first cycle. *In situ* x-ray diffraction studies and the electrochemical performance of an amorphous Si-Sn alloy was reported by Beaulieu et al. [7] and a specific capacity of 860 mAh/g for $Si_{0.66}Sn_{0.33}$ was attained for the first discharge. In another study, Beaulieu et al. [17] have shown that an amorphous alloy of Sn and Si can reversibly react with Li and undergo volume changes on the order of 250%. Suzuki et al. [18] have reported that the optimum atomic ratio of Si:Sn is 8:1, and a capacity as high as 1400 mAh/g was attained. Dahn et al. [19] have demonstrated the effect of adding rare earth elements to $Si_{1-x}Sn_x$ on its structural properties, and hence on its electrochemical performance, and have found an optimal composition of 20-40 at% Sn and15-20 at% rare earth elements. Hatchard et al. [20] have compared the electrochemical performance of different binary systems including Si-Sn, Si-Ag, and Si-Zn and shown that a Si-Sn system has superior features including phase stability during subsequent cycles and the least capacity fade compared to other investigated system. In order to understand the interaction between the grains in the electrode, Timmons et al. [21] have undertaken an *in situ* optical study of a $Si_{0.64}Sn_{0.36}$ electrode, suggesting that increasing the lower cut off potential plays a role in electrochemical performance by limiting volume expansion and hence interparticle movement in the electrode. Rock et al. [22] had limited success in studying a Sn-Si-C composite. They reported that the highest capacity attained after 30 cycles was 470 mAh/g coupled within irreversible capacity loss of 50.5%, which made it a very inferior electrode.

The properties of Si-C prepared by Timmons et al. [23] using mechanical milling and sputtering provide insight into the interaction between C atoms and other components of the electrode material. Although both Si and C are active materials, capacity loss has been observed in Si-C samples due to local Si-C bonding. Thus nanocomposite Si-C materials may best be viewed as active-inactive

composites where localized inactive regions result from Si-C bonds analogous to those found in inactive SiC.

Because of their improved electrical conductivity compared to pure Si, Si-Sn based materials remain attractive and the synthesis of a suitable nanostructured material that can effectively accommodate volume expansion and maintain good cycleability warrants further investigation.

The addition of C to other active components has been successful in improving electrode performance in the past [24] as it is electrically conductive and provides a suitable matrix for nanostructured active grains to undergo lithiation and de-lithiation with minimal capacity loss. To the best of our knowledge, no comprehensive study of the effects of C on the Sn-Si system has been reported. In the Sn-Si-C system, it is possible that some C may be incorporated in SiC-like bonding as found in Si-C [23] resulting in capacity loss as described above. It is the aim of the current work to make such a systematic study using combinatorial methods and to explore the role of C on the microstructural and electrochemical performance of a Sn-Si alloy.

5.3 Experimental

Three pseudobinary combinatorial libraries in the Sn-Si-C system were produced using a Corona Vacuum Coater model V3-T multitargets sputtering system described in detail in reference [16]. Libraries were distinguished by their nominal compositions in $Sn_{100-x-y}Si_xC_y$, where "$y \sim 20$", "$y \sim 35$", and "$y \sim 45$". Table 5.1 summarizes the target compositions and deposition parameters for the three libraries. A base pressure of 1×10^{-7} Torr was reached prior to sputtering. Three different kinds of targets two inches in diameter were used: a C target (99.999% pure) obtained from Kurt J. Lesker Co., a Sn target (99.85% pure) cut

from a plate obtained from Alfa Aesar, and a Si target (99.99% pure, Williams Advanced Materials).

Prior to deposition, all substrates were first exposed to an O_2 plasma and then to an Ar plasma for 15 minutes each. To obtain the desired deposition profile, different stationary masks were placed over the targets. Deposition was carried out with a flow of 3 sccm argon. The chamber pressure was maintained at 1 mTorr of argon gas during the depositions. The sputtering table was loaded with a variety of substrates: Cu disks for mass determination, a Cu foil for composition analysis, a Si (100) wafer for x-ray diffraction measurement, Kapton films for Mössbauer measurement and a combinatorial cell plate for electrochemical testing. The angular velocity of sputtering table was 14 rpm to ensure atomic level mixing [16] of the Si, Sn and C atoms. Continuous films on the 76 mm wide sputter track were deposited on these substrates. The three masks were designed to obtain: (1) a constant amount of C throughout the library, (2) a linearly varying amount of Si versus Sn. As the sputtering table passed over the target, a layer of approximately one atom thickness was deposited this assured the atomic scale mixing of the deposition. A Sartorius SE-2 microbalance (0.1 μg precision) was used to determine the position-dependence of the mass per unit area of the sputtered materials. Thin film library compositions were determined using a JEOL-8200 Superprobe electron microprobe

Table 5.1: Summary of the compositions and sputtering parameters for the prepared combinatorial libraries.

library number	nominal C content (y)	range of Si content (x) in $Sn_{100-x-y}Si_xC_y$	power to targets (W)			pressure (mT)
			Sn	Si	C	
1	20	$10 < x < 65$	13	2 × 140	200	1
2	35	$2 < x < 60$	17	110	2 × 95	1
3	45	$5 < x < 45$	53	150	2 × 250	1

using wavelength dispersive spectroscopy (WDS) to verify that the intended composition gradients were achieved. The microprobe was equipped with a translation stage, which allowed the composition measurements to be matched with the results of other measurements. X-ray measurements were collected using an INEL CPS120 curved position-sensitive detector coupled with an x-ray generator equipped with a copper target x-ray tube. The incident angle of the beam with respect to the sample was ~6◦, which does not satisfy the Bragg condition for a Si (100) wafer used as a substrate, allowing for zero-background measurements. The diffraction peaks ($2\theta = 6^{o}$ to 120^{o}) were collected simultaneously. Acquisition time for each composition was 2400 s. The spatial resolution on the film as defined by the distance between adjacent x-ray diffraction scans in conjunction with the composition gradient in the sample yielded an uncertainty in the composition for the x-ray measurements of about ±0.5 at% in Si and Sn. Room temperature ^{119}Sn Mössbauer effect spectra were collected using a constant-acceleration Wissel System II spectrometer equipped with a $Ca^{119m}SnO_3$ source. The velocity scale of the system was referenced relative to $BaSnO_3$. A lead aperture was used to select the part of the film to be investigated [25]. The width of the aperture yielded an uncertainty in Si and Sn composition of ±2.0 at% for the Mössbauer measurements.

For electrochemical testing, a 64-channel electrochemical cell plate based on a resin-based printed circuit board as illustrated in Figure 5.1 was used. Details of this cell plate design can be found in reference [6]. A combinatorial electrochemical cell was constructed as described by Fleischauer et al. [26]. Slow scan cyclic voltammetry measurements were performed on the 64 channels of the cell plate using a multichannel pseudopotentiostat as described by Cumyn et al. [27]. Cells were discharged/charged between 1.2 and 0.005 V for a total of 27 cycles. The attractiveness of the combinatorial approach is its ability to create and study large numbers of samples. Once promising compositions are identified, more detailed studies employing coin cells and extended cycling can be undertaken. The

differential capacity, dQ/dV versus V was determined by dividing the current (dQ/dt) by the sweep rate (dV/dt). The scan time was 12 hours for each discharge or charge during the first three cycles, 3 hours during cycles 4–24 and 12 hours again for cycles 25, 26 and 27. This was done so that changes to the electrode which may have occurred during 27 cycles could be carefully monitored by comparing slow cyclic voltammetry measurements take in the first three and last three cycles.

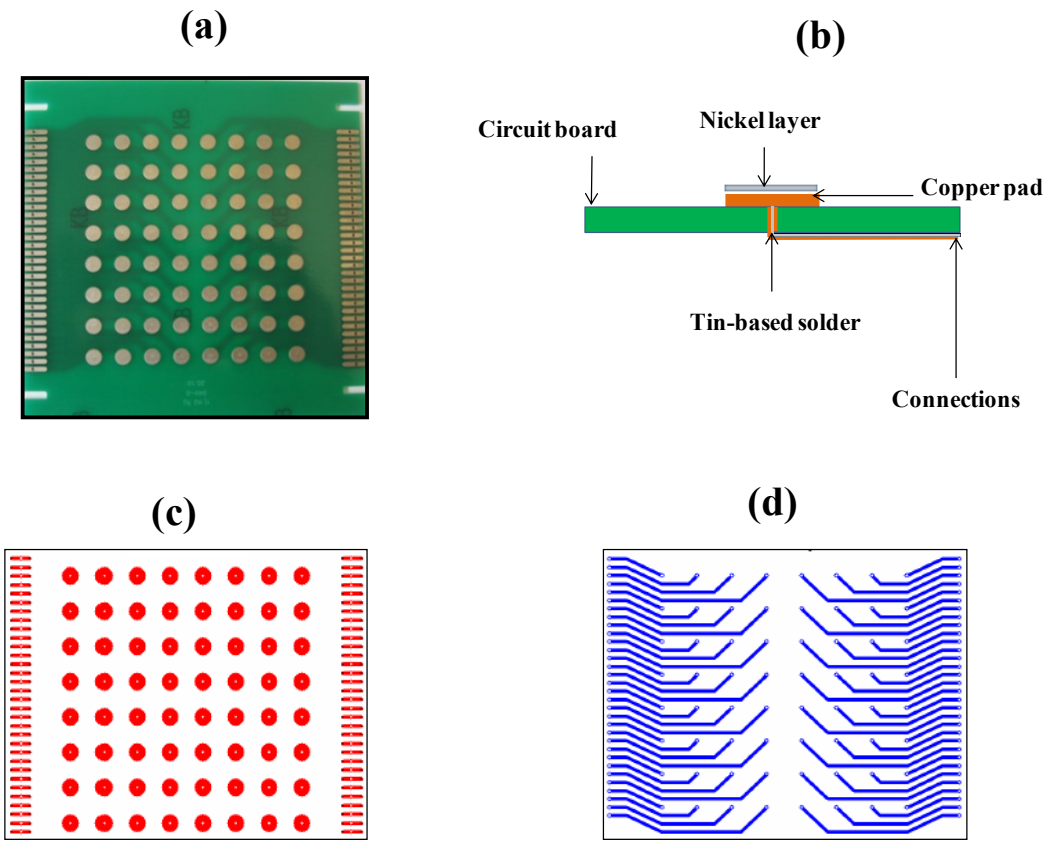

Figure 5.1: (a) Photograph (from top side) of 64-electrode printed circuit board cell plate, (b) schematic of cross section through printed circuit board cell plate showing connection of cell pads with charger leads, (c) lead pattern on top of printed circuit board and (d) lead pattern on the bottom of printed circuit board.

5.4 Results and Discussion

5.4.1 Composition Studies

Figure 5.2 shows the Gibbs triangle for the Sn-Si-C system showing the compositions of the three prepared libraries (see Table 5.1). This figure shows that libraries with varying Sn and Si content and with an approximately constant amount of C were obtained. The shaded area in the figure indicates the amorphous or nanostructured range as determined from x-ray diffraction. Materials were judged to be nanostructured or amorphous when the x-ray patterns displayed no sharp diffraction peaks, only broad amorphous like"humps".

Compositions as obtained from microprobe analysis were confirmed by "library closure" [28] as shown in Figure 5.3. In this figure the composition and mass per unit area of a typical library as a function of position along the library is plotted. Figure 5.3(a) shows moles per unit area of C (open diamond), Sn (solid triangle), and Si (solid squares) defined by "constant", "linear in" and "linear out" sputtering masks, respectively. Figure 5.3(b) shows that the compositions calculated from Figure 5.3(a) agree with the compositions measured by wavelength dispersive spectroscopy. Figure 5.3(c) compares the measured mass of the sputtered films on each weighing disk (open circle) with the calculated mass from the curves in Figure 5.3(a) (solid line) for a $Sn_{100-x-y}Si_xC_y$ library ($10 < x < 65$ and $y \sim 20$). The other two libraries showed similar results.

5.4.2 X-ray Diffraction Studies

Figures 5.4, 5.5, and 5.6 show the results of x-ray diffraction studies of the three libraries (summarized in Table 5.1) that are presented in this work. The composition of each sample is indicated. Figure 5.4 shows selected diffraction patterns that cover the composition range of $Sn_{100-x-y}Si_xC_y$ in Library 1. For the compositions studied in the present work, an amorphous or nanostructured phase

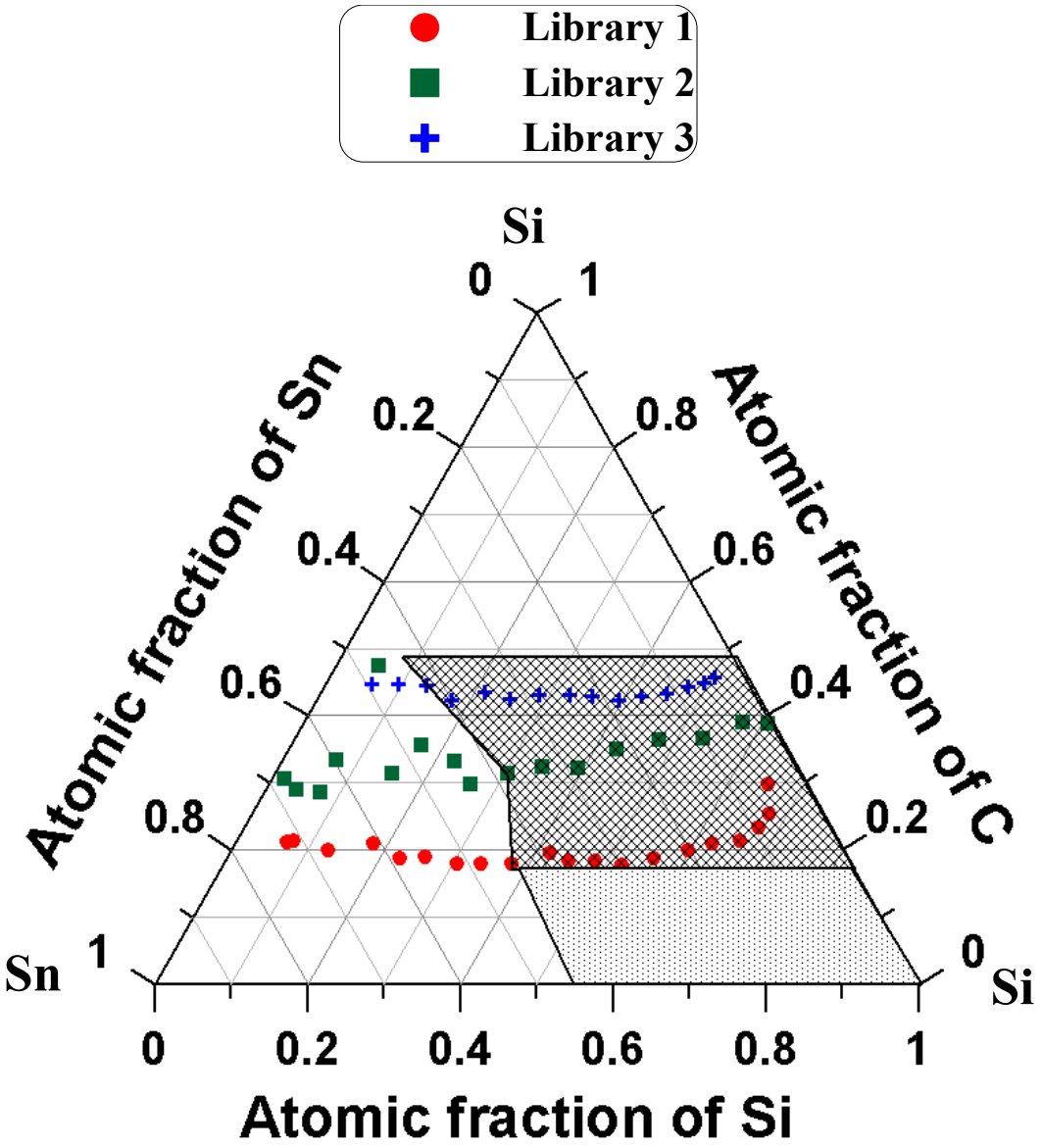

Figure 5.2: Gibbs triangle for the Sn-Si-C system showing compositions of the $Sn_{100-x-y}Si_xC_y$ libraries as determined by electron microprobe analysis. Library 1 (y ~ 20): circles; Library 2 (y ~ 35): squares; Library 3 (y ~ 45): crosses. The darker shaded area indicates the composition range over which the samples where amorphous or nanostructured in the present work. The amorphous ranges for sputtered alloys inferred from measurements on samples without C by Beaulieu et al. [7] and Hatchard et al. [14] are shown in the diagram by the lighter shaded region.

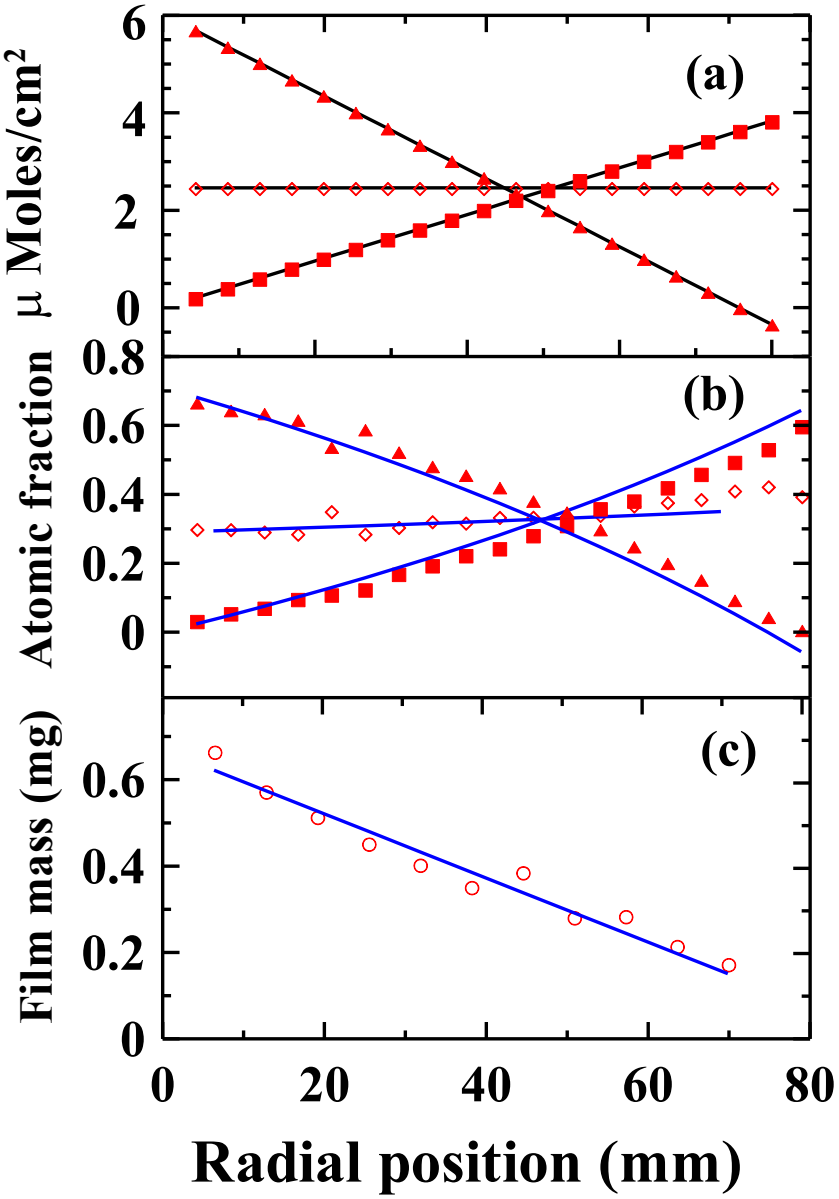

Figure 5.3: A typical "library closure" (a) the moles per unit area of C (open diamonds), Sn (solid triangles) and Si (solid squares) defined by "constant", "linear in" and "linear out" sputtering masks, respectively. (b) Composition calculated from (a) agree with the measured compositions from wavelength dispersive spectroscopy (WDS). (c) The measured mass of the sputtered films on each weighing disk (open circles). Data points compared to that calculated from the curves in (a) (solid line) for the $Sn_{100-x-y}Si_xC_y$ library ($2 < x < 60$ and $y \sim 35$).

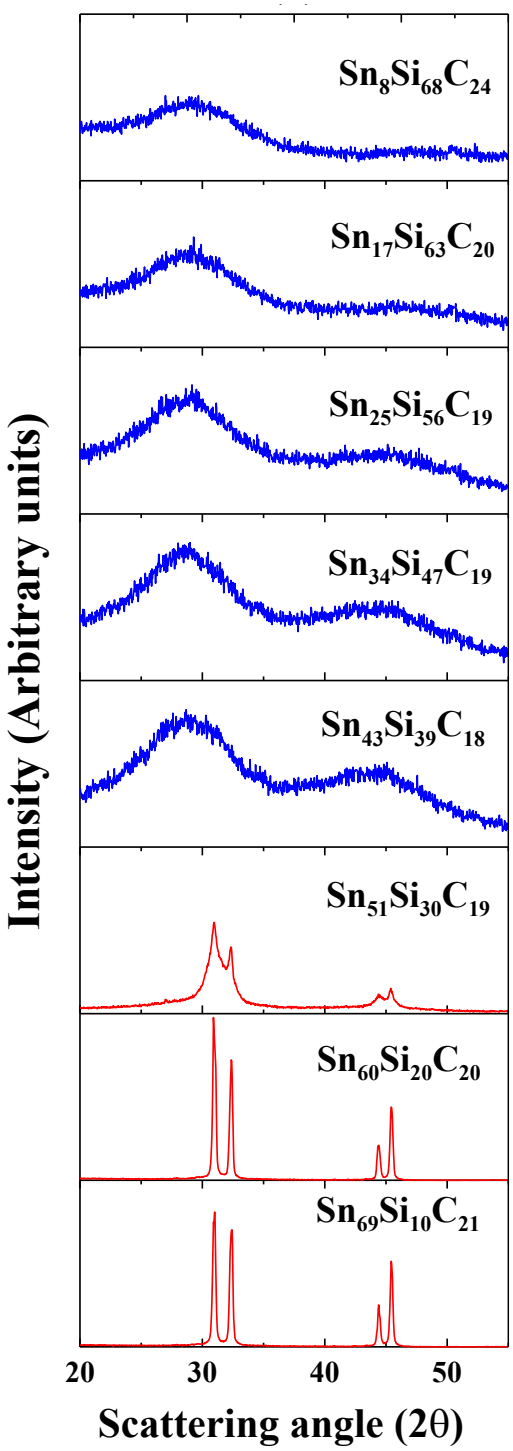

Figure 5.4: X-ray diffraction patterns of selected samples from Library 1. Compositions are indicated.

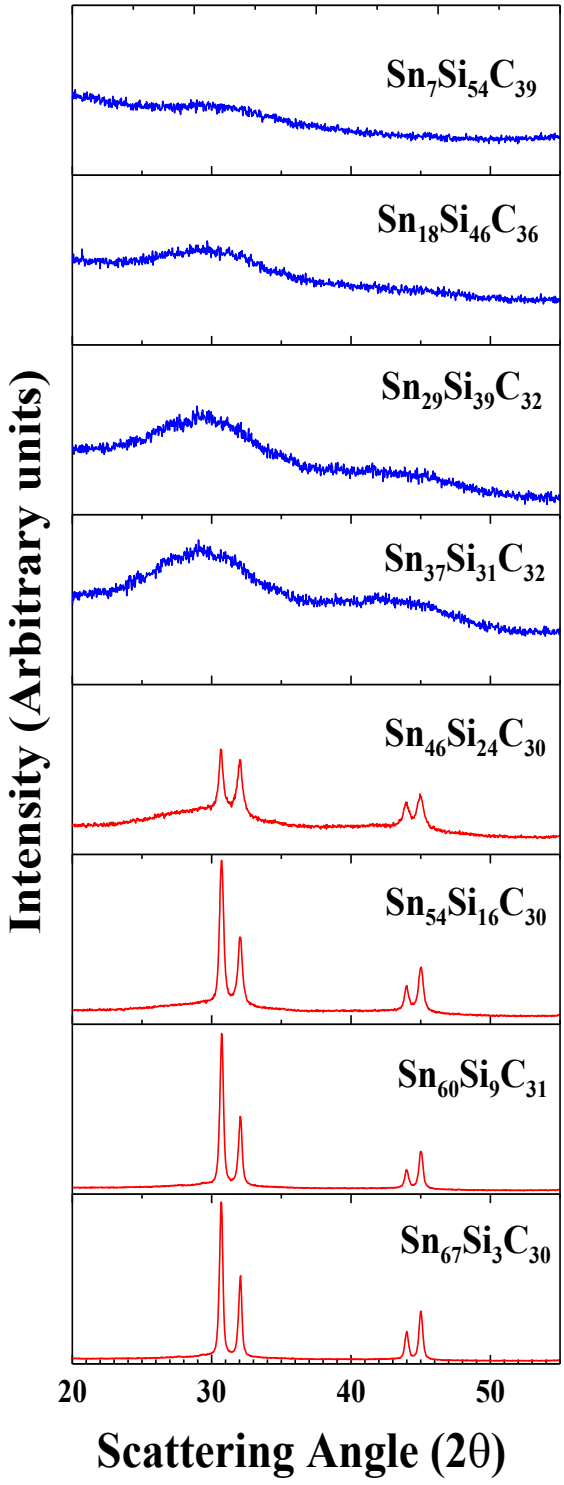

Figure 5.5: X-ray diffraction patterns of selected samples of Library 2. Compositions are indicated.

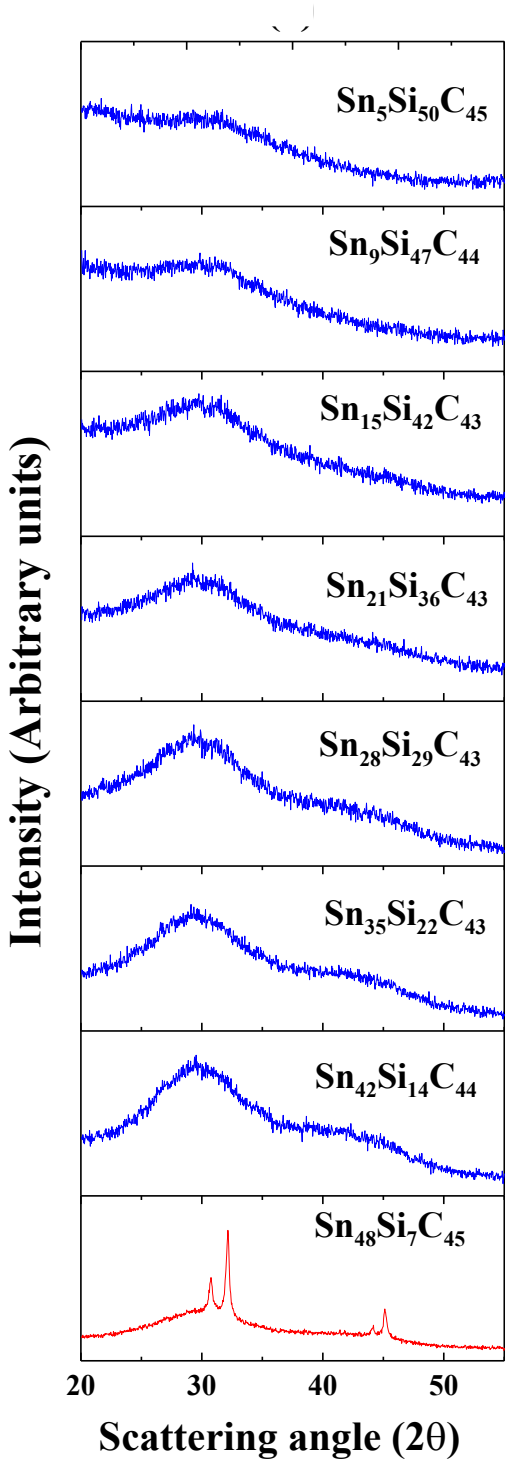

Figure 5.6: X-ray diffraction patterns of selected samples of Library 3. Compositions are indicated.

was found for Sn content in the range of $8 \leq (100\text{-}x\text{-}y) \leq 43$. Figure 5.5 shows the diffraction patterns for Library 2 where the amorphous or nanostructured range was found to be between $7 \leq (100\text{-}x\text{-}y) \leq 37$. This range was extended in Library 3 as shown in Figure 5.6, to $5 \leq (100\text{-}x\text{-}y) \leq 42$. In all these ranges the thin films had broadened peaks centered at $2\theta = 29$ and 44◦, which closely matched the reflections of amorphous or nanostructured Si [8, 30] reported previously in reference [31]. As found in previous work [30, 31] this region certainly extends to lower Sn content and would include the $(100\text{-}x\text{-}y) = 0$ axis. As the amount of Sn exceeded a certain percentage, $(100\text{-}x\text{-}y) \geq 51$, $(100\text{-}x\text{-}y) \geq 46$, and $(100\text{-}x\text{-}y) \geq 48$ for Libraries 1 to 3, respectively, diffraction peaks appeared at 2θ=30.6◦, 32.0◦, 44.0◦, and 45.0◦peaks, corresponding to the (200), (101), (220), and (211) reflections of crystalline Sn. Library 3 had the largest range of compositions that were found to be amorphous or nanostructured. The Sn-rich limit of the amorphous range varied systematically with C content and corresponded to Sn:Si atomic ratios of ~ 1:1, 1.2:1 and 3:1, respectively, in Libraries 1 through 3. Beaulieu et al. [7] studied the structure of $Si_{100-x}Sn_x$ electrodes prepared by the sputtering method. They reported that the amorphous phase of $Si_{100-x}Sn_x$was found in samples with $x \leq 36$, which corresponds to a 0.8:1 ratio of Sn:Si. Hatchard et al. [14] reported that the amorphous range of a $Si_{100-x}Sn_x$ sputtered film was obtained when $0 < x < 50$ (corresponding to a1:1 ratio). These measurements indicate that the amorphous ranges extends downward (in C content) from the region studied in the present work to the line on the $y = 0$ (no C) axis as illustrated in Figure 5.2. Comparing the reported Sn:Si ratios from these previous reports with those obtained in the present study shows that the C content plays a role in extending the amorphous range and acts as a buffer matrix that inhibits the diffusion of Sn atoms to form well ordered crystalline phases of Sn. Generally, within of each library, a systematic dependence of the structure on Si content was observed. For each different amount of C present, a different minimum Si to Sn ratio was needed to produce an amorphous or nanostructured phase. With increasing C content, the necessary minimum Si to Sn ratio decreased. Although

there is a possibility of forming SiC, no peaks for crystalline silicon carbide were observed for any of our samples. Generally, the present results show that a substantial portion of the compositions prepared in this work are amorphous or nanostructured and, from structural standpoint, show potential for use as electrode materials.

5.4.3 Electrochemical Studies

Figures 5.7(a) – 5.9(a) show selected differential capacity versus potential plots for the three $Sn_{100-x-y}Si_xC_y$ combinatorial libraries. The composition of each sample is indicated. The first three cycles are shown. Close inspection of the results for Libraries 1, 2, and 3 shows smooth curves with broad humps for $8 \leq (100-x-y) \leq 43$, $7 \leq (100-x-y) \leq 37$, and $5 \leq (100-x-y) \leq 42$, respectively, during both discharge and charge. Such a profile is similar to the characteristics of amorphous sputtered Si thin films [6] and suggests that little crystalline Sn was present in the present samples. X-ray diffraction patterns for these compositions show that the materials were amorphous or nanostructured. Sharp peaks in the differential capacity versus voltage curves were observed for crystalline portions of each library. Generally, the sharp peak in the differential capacity versus potential curves is an indicator of the presence of crystalline phases, in this case crystalline Sn [32] and the corresponding panels in the figures showing x-ray diffraction patterns confirmed that crystalline Sn was present. It seems that there is a transition point where the dispersed Sn within the Si and C matrix starts to aggregate, forming regions of crystalline Sn.

Figures 5.7(b) to 5.9(b) show the specific capacity versus cycle number for the same samples shown in Figures 5.4 to 5.6 and Figures 5.7(a) to 5.9(a). Figure 5.7(b) shows that the capacity of cells degraded rapidly for compositions that were: (1) found to contain crystalline Sn as evidenced by x-ray diffraction patterns and in the differential capacity versus potential curves (toward the bottom of the panel) and

(2) in Si-rich regions where oxygen concentrations were found to be higher (toward the top of the panel).

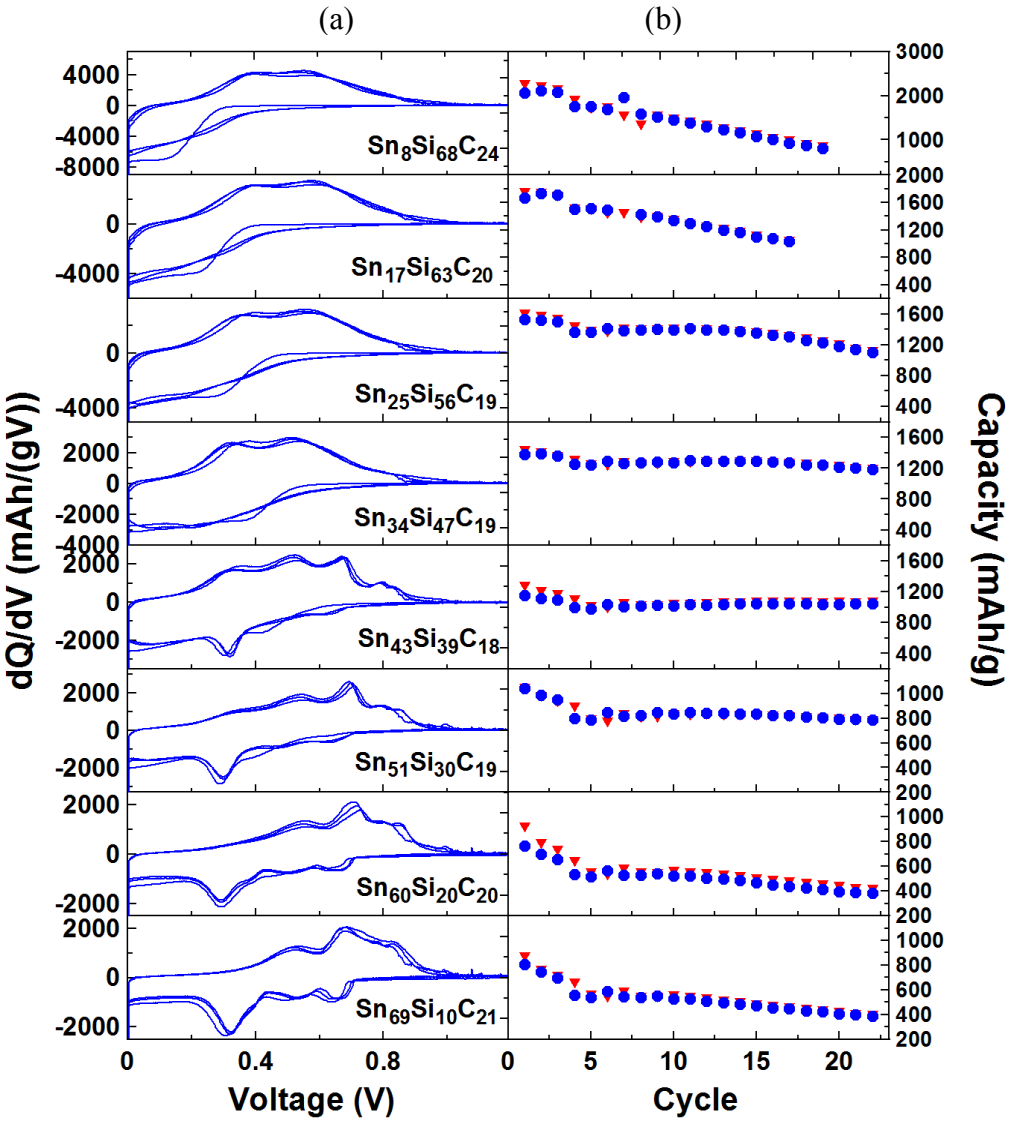

Figure 5.7: (a) dQ/dV versus voltage for the first 3 cycles and (b) capacity versus cycle number, discharge capacity (red solid triangle) and charge capacity (blue solid circles) from Library 1. Compositions are indicated.

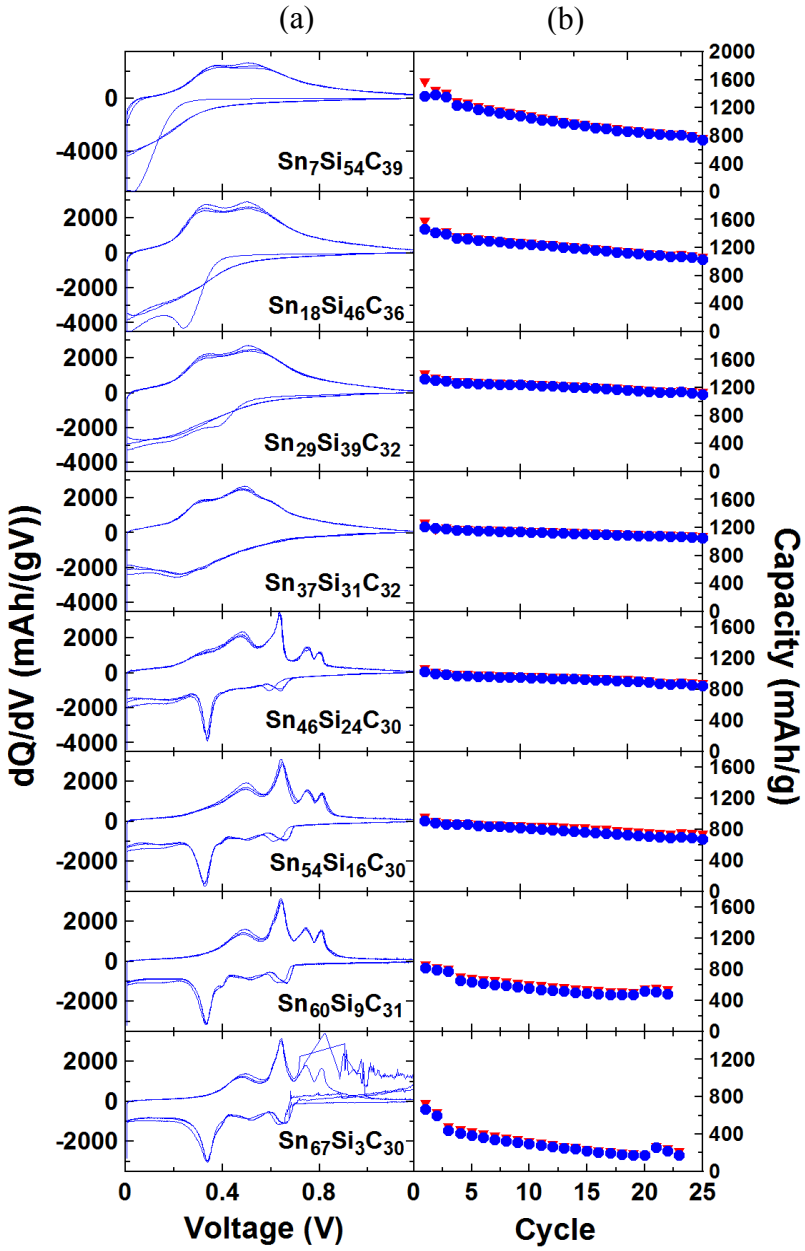

Figure 5.8: (a) dQ/dV versus voltage for the first 3 cycles and (b) capacity versus cycle number, discharge capacity (red solid triangle) and charge capacity (blue solid circles) from Library 2. Compositions are indicated.

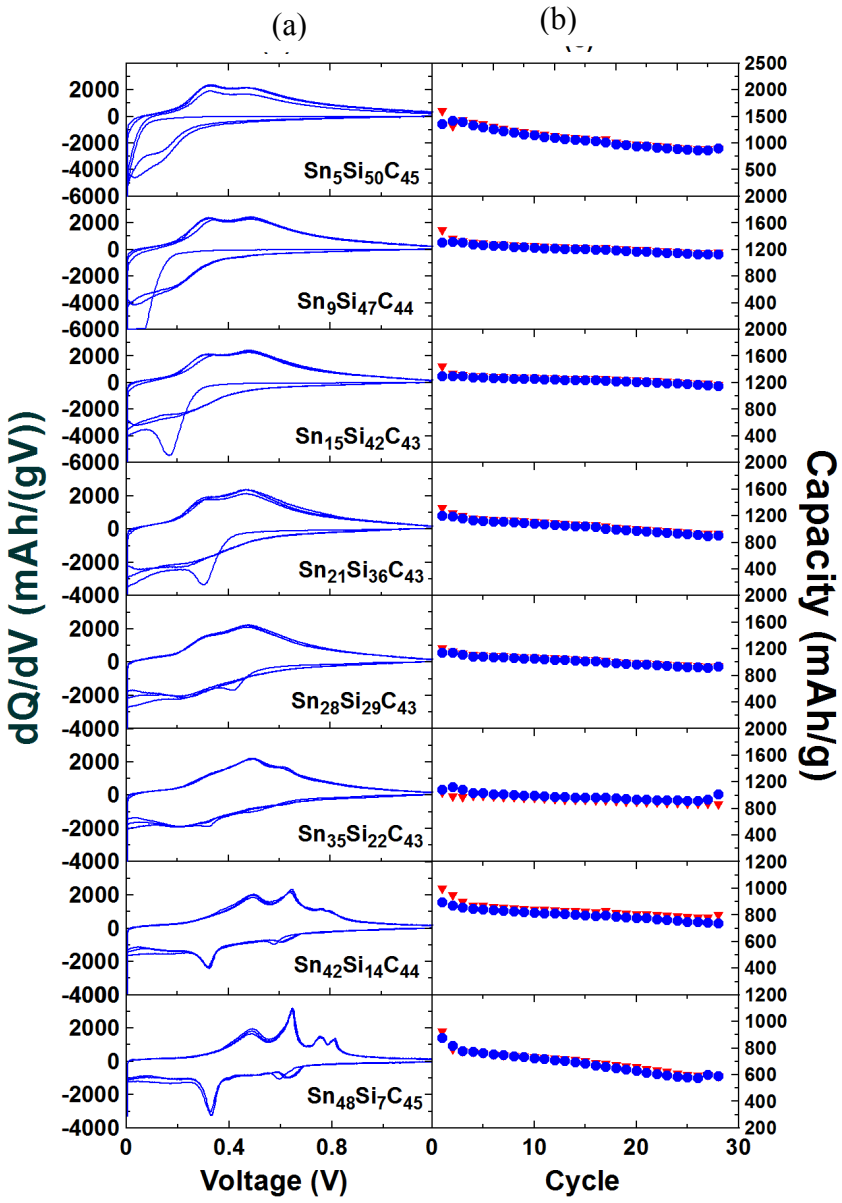

Figure 5.9: (a) dQ/dV versus voltage for the first 3 cycles and (b) capacity versus cycle number, discharge capacity (red solid triangle) and charge capacity (blue solid circles) from Library 3. Compositions are indicated.

This excess oxygen may come from residual oxygen in the sputtering chamber or from oxygen incorporation in possibly porous films upon exposure of the films to air. Electron microprobe measurements found that Si-rich regions had more oxygen content compared to other regions in the library. For example, microprobe analysis showed that Library 3 had an oxygen content that ranged from 1 to 6% atomic. Elsewhere, the capacity remained within 90% of the initial value after about27 cycles. Such degradation could also be a result of mechanical cracking caused by volume expansion during cycling since these electrodes do not contain any C black or binder [9]. Figures 5.10(a) to 5.10(c) show the capacity versus cycle number for Libraries 1 to 3, respectively. Upon close inspection of these plots, the following remarks can be made:(1) most of the samples did not suffer from high irreversible capacity in the first cycles, which is a common problem that has been reported in literature studies, especially with alloy negative electrodes, and (2) undesirable capacity loss is associated with compositions in both Si- and Sn-rich regions, as discussed above. Figure 5.11 shows plots of potential versus capacity for the best performing cell on the basis of capacity and capacity retention from Library1 ($Sn_{34}Si_{47}C_{19}$), Library 2 ($Sn_{37}Si_{31}C_{32}$) and Library 3 ($Sn_{35}Si_{22}C_{43}$). The figure also shows the differential capacity versus potential for the first 3 cycles and the last three cycles of the same cells. Figure 5.11(a) clearly shows smooth and stable charge and discharge curves with no plateaus. As shown in the figure, the capacity achieved for this cell was 1450 mAh/g. Hatchard et al. [30] have investigated the electrochemical performance of a composition similar to that shown in Figure 5.11(a), but containing no C. Although the capacity for their sample (row 7 of Figure 6 in reference [30]) was about 2000 mAh/g, substantial capacity fade was observed after only 10 cycles. Figure 5.11(b) shows excellent capacity retention for the sample from Library 2. The stability of this composition during discharge and charge is reflected by the smooth curve during charge and discharge, with a capacity of 1060 mAh/g after 27 cycles. Similar results are shown for Library 3,

except that features in the differential capacity curves as illustrated for the last three cycles indicate the precipitation of crystalline Sn-containing phases.

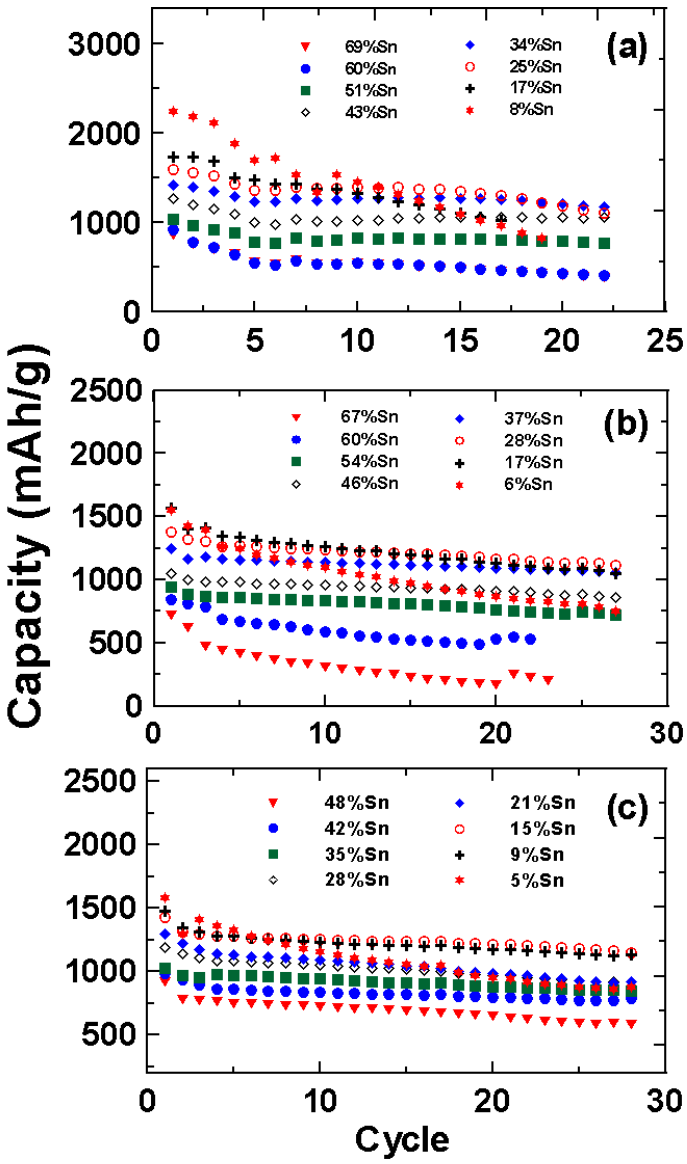

Figure 5.10: Capacity versus cycle number plots for compositions indicated from the combinatorial libraries of $Sn_{100-x-y}Si_xC_y$ (a) Library 1; ($10 < x < 65$ and $y \sim 20$), (b) Library 2; ($2 < x < 60$ and $y \sim 35$), and (c) Library 3; ($5 < x < 45$ and $y \sim 45$).

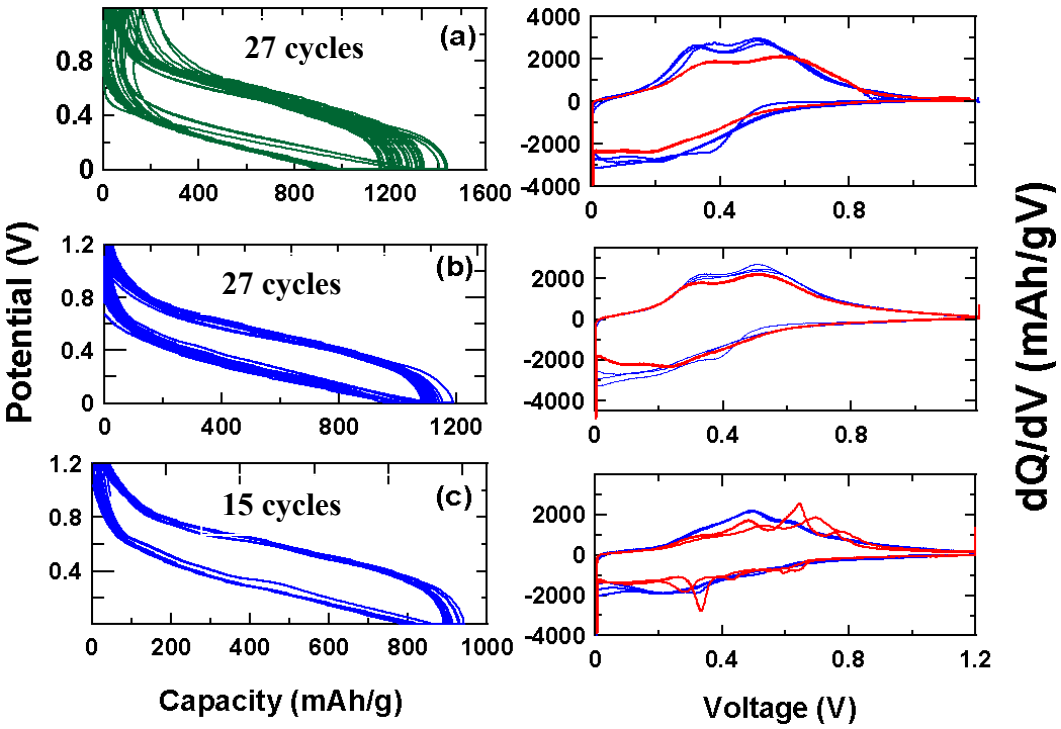

Figure 5.11: (a) Potential versus capacity for an electrode with composition of $Sn_{34}Si_{47}C_{19}$ from Library 1 and the corresponding differential capacity curves. The first 3 cycles are shown in blue and the last 3 cycles in red. (b) Data as in (a) for an electrode with composition of $Sn_{37}Si_{31}C_{32}$ for from Library 2, and (c) data as in (a) for an electrode with composition of $Sn_{35}Si_{22}C_{43}$ from Library 3. The number of cycles shown in the potential versus capacity plots is indicated in the figure.

The high first cycle columbic efficiency achieved in these electrodes is a consequence of the thin film nature of these materials. Even pure Si thin films can show excellent first-cycle efficiency as shown in reference [6].

Knowing the phases present in the active material make it possible to understand the measured values of specific capacities. Most of the literature does not compare the obtained capacity with that predicted for the expected phases. Figures 5.12(a) to 5.12(c) present the theoretical capacities for the first charge (removing lithium) for the selected electrodes from the 3 libraries, respectively, as discussed above. Figure 5.12 shows the measured capacity (solid circles) and theoretical capacity (solid triangles) assuming that $Li_{15}Si_4$, $Li_{22}Sn_4$ and LiC_6 are the fully lithiated room temperature phases for Si, Sn, and C, respectively, as well as the theoretical capacity (solid lines) assuming $Li_{15}Si_4$ and $Li_{22}Sn_4$ are fully lithiated room temperature phases of Si and Sn, respectively, and that C has negligible capacity. Figure 5.12(a) shows there is reasonable agreement between the theoretical and the observed values, particularly for high Sn content. As the Sn content is decreased, particularly in Libraries 2 and 3, where the C content is higher, the observed capacity falls far below the theoretical capacity. It is probable that this decreased capacity is the result of the formation of nanocrystalline SiC which is inactive and would not be visible in the x-ray diffraction pattern if the grain size were in the 1-2 nm range.

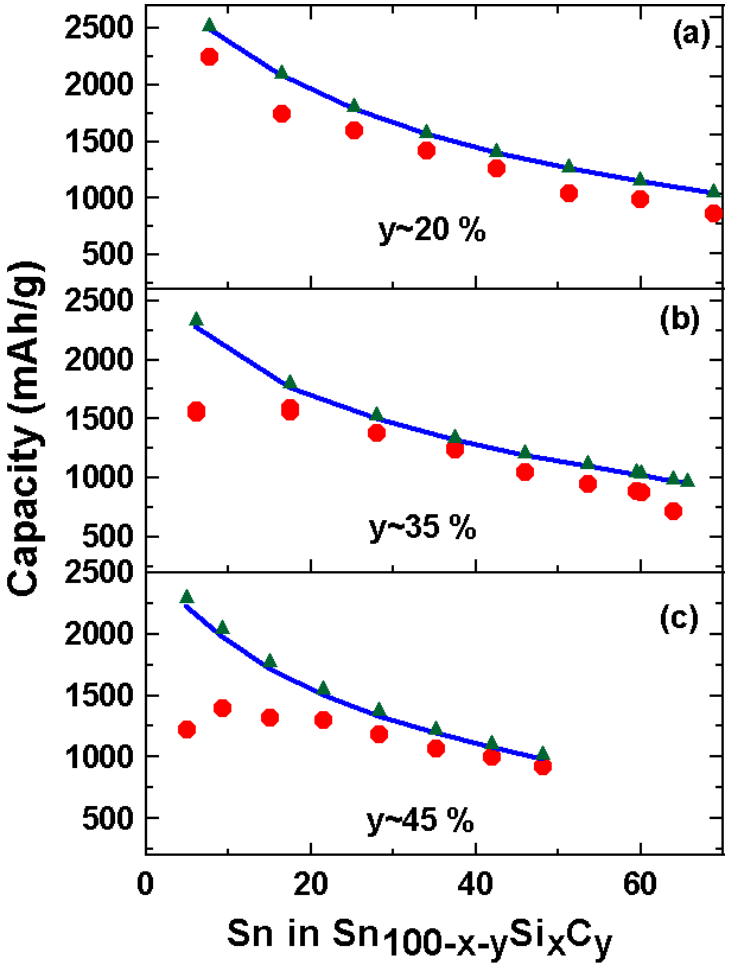

Figure 5.12: Theoretical and observed specific capacity of (a) $Sn_{100-x-y}Si_xC_y$ library ($10 < x < 65$ and $y \sim 20$), (b) $Sn_{100-x-y}Si_xC_y$ library ($2 < x < 60$ and $y \sim 35$), and (c) $Sn_{100-x-y}Si_xC_y$ library ($5< x < 45$ and $y \sim 45$). The observed data are represented by solid circles. The solid triangles correspond to the theoretical capacity, assuming the Si, Sn and C react with Li to form $Li_{15}Si_4$, $Li_{22}Sn_4$ and LiC_6, respectively. The solid line assumes that the C in the sample does not react with lithium but that the Si and Sn form $Li_{15}Si_4$ and $Li_{22}Sn_4$.

5.4.4 Mössbauer Studies

Figure 5.13 shows room temperature ^{119}Sn Mössbauer effect spectra for the samples from Library 1, which has approximately 20% C, with the indicated compositions. These have been fitted to two Lorentzian components; a singlet from an essentially pure Sn phase with a center shift of +2.54 mm/s [24] and quadrupole split doublet with a less positive center shift, resulting from a Sn-Si phase [32]. As the amount of Sn increased across the library, the singlet peak, corresponding to the Sn phase, increased in intensity at the expense of the Sn-Si phase. This is presumably due to the increased aggregation of Sn regions in the C matrix. It is apparent that even for very small Sn concentrations, Sn regions are present. Figure 5.14 shows the ^{119}Sn Mössbauer effect spectra for samples from Library 2, which has roughly 30% C, with the indicated compositions. Spectra collected from samples with 46 at% Sn or less were well fit to one doublet. The inclusion of singlet for elemental Sn did not improve the fit and is not included in the present analysis. For larger concentrations of Sn, the aggregation of Sn is evidenced by the appearance of the singlet component in the spectra. The small feature present in the Sn-rich region of the library corresponds to a small amount of tin oxide, as represented by a Lorentzian singlet component with a center shift of near 0 mm/s. It is clear from Figure 5.14 that the aggregation of Sn was inhibited up to the 46% Sn. This suggests that the addition of C plays an important role in defining the microstructure of the sample. The increase in the amount of C matrix supporting the nanostructured Sn-Si phases helps to prevent the aggregation of pure Sn regions. Figure 5.15 shows the ^{119}Sn Mössbauer effect spectra for samples from Library 3, which has roughly 45% C, with the indicated compositions. Close inspection of these spectra shows that, in addition to the doublet component of Sn-Si phase, there is only a very small singlet component from pure Sn which had near zero amplitude (as illustrated in the figure) for less than 28% Sn. According to the trends shown in the previous two libraries, the increase in C content has further inhibited the aggregation of Sn. It is possible that the formation of SiC as suggested above on the

basis of electrochemical studies may ultimately limit the ability of C to totally eliminate the possibility of free Sn formation by binding up Si and forcing Sn out of the resulting Sn-Si phase.

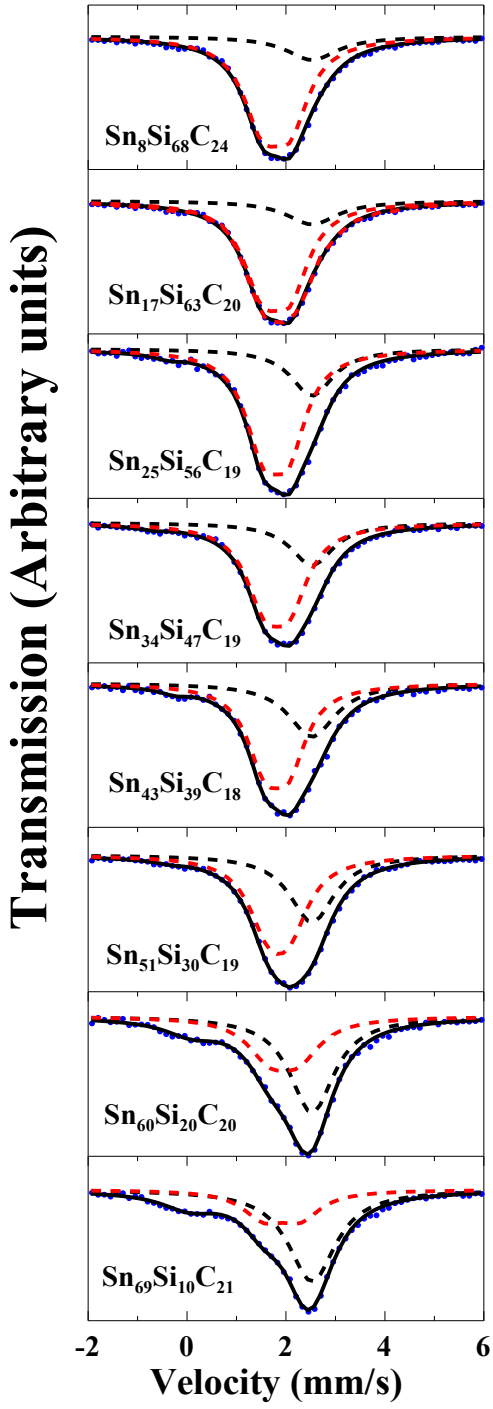

Figure 5.13: Selected Mössbauer effect spectra of samples from Library 1; circles: raw data, solid lines: overall fit, black dashed line: elemental Sn component, and red dashed line: Sn-Si component: Compositions are indicated.

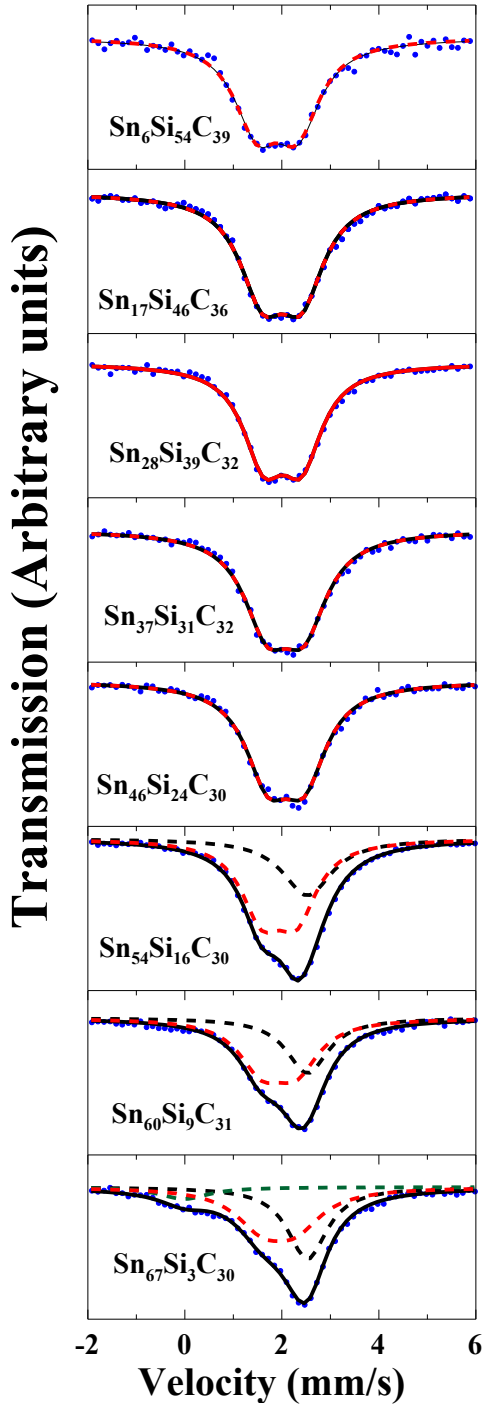

Figure 5.14: Selected Mössbauer effect spectra of samples from Library 2; circles: raw data, solid lines: overall fit, black dashed line: elemental Sn component, red dashed line: Sn-Si component, and green dashed line: SnO_2 component. Compositions are indicated.

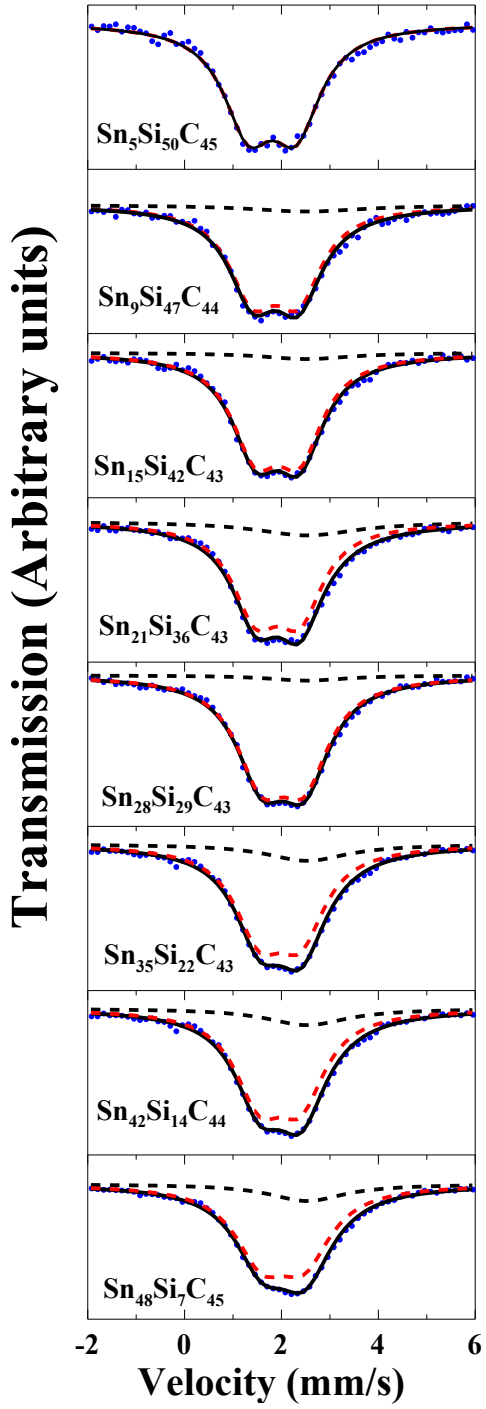

Figure 5.15: Selected Mössbauer effect spectra of samples from Library 3; circles: raw data, solid lines: overall fit, black dashed lines: elemental Sn component, red dashed line: Sn-Si component. Composition is indicated.

Figures 5.16 to 18 show the quadrupole splitting, center shift, and relative area of Sn-Si component of Libraries 1 to 3, respectively. Figure 5.16 shows a decrease in the quadrupole splitting and an increase in the center shift as a function of Sn content in the library which gives evidence of changes to the short-range ordering within the amorphous Sn-Si. This can be explained as the following: If there is a replacement of Sn-Si neighbor pairs by Sn-Sn neighbor pairs, a more positive center shift would be observed, where the center shift of Sn in Si (+1.88 mm/s) is less positive than the center shift of Sn in Sn(+2.54 mm/s). The replacement of Sn-Si bonds with Sn-Sn bonds would result in a more symmetric Sn environment and would correspond to decrease in the quadrupole splitting. A symmetric Sn environment corresponds to zero quadrupole splitting. This observation is consistent with what was observed for the other two libraries as illustrated in Figures 5.17 and 5.18.

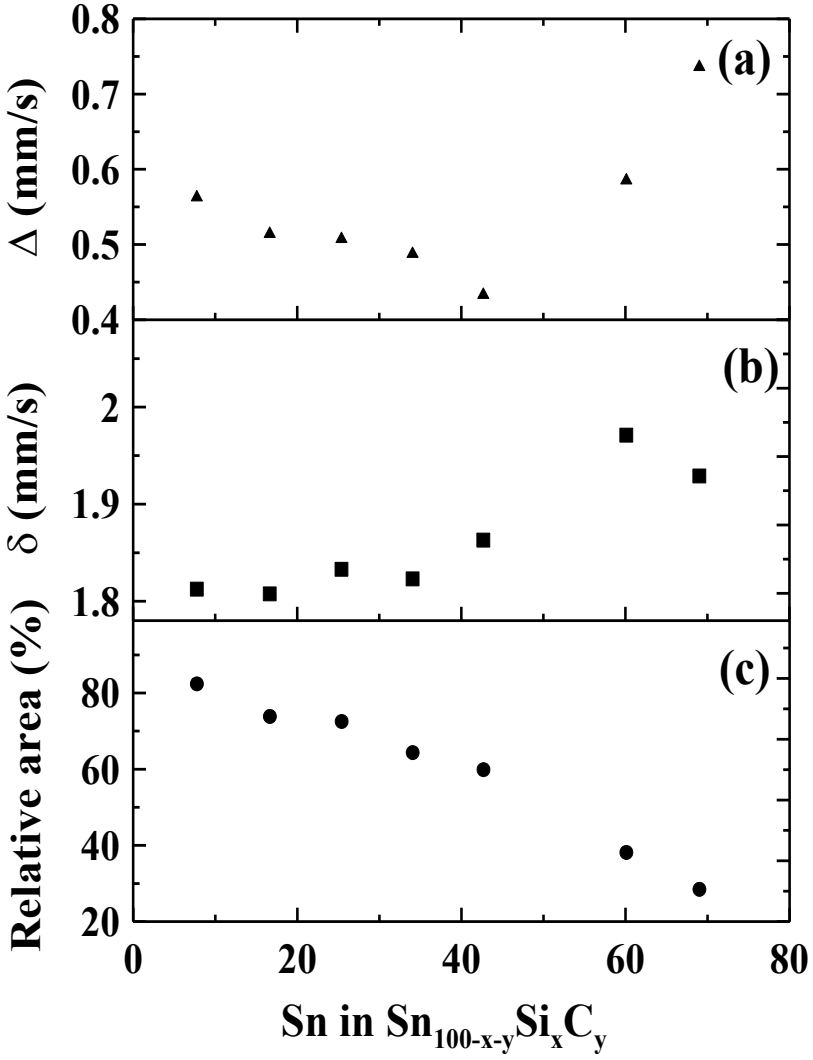

Figure 5.16: Room temperature ^{119}Sn Mössbauer effect parameters of the doublet component for $Sn_{100-x-y}Si_xC_y$ combinatorial Library 1 ($10 < x < 65$ and $y \sim 20$) (a) quadrupole splitting (Δ), (b) center shift (δ),and (c), relative area versus Sn content of the Sn-Si component.

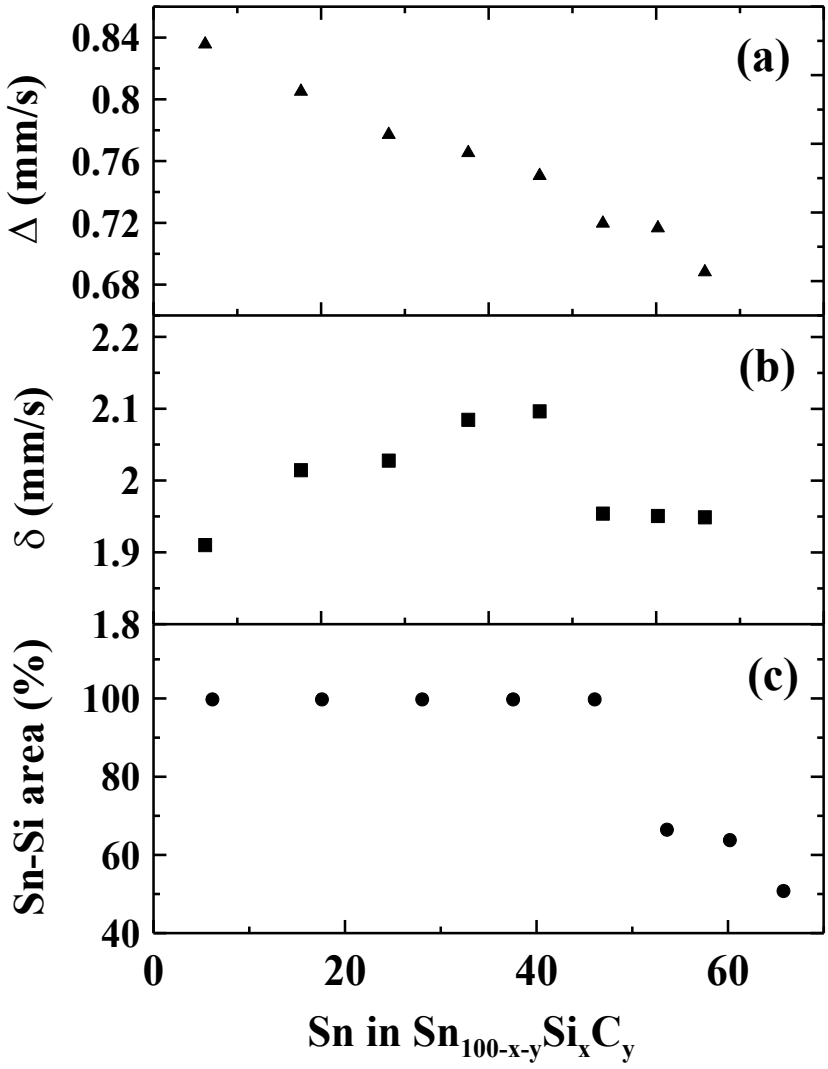

Figure 5.17: Room temperature ^{119}Sn Mössbauer effect parameters of the doublet component for $Sn_{100-x-y}Si_xC_y$ combinatorial Library 2 ($2 < x < 60$ and $y \sim 35$). (a) quadrupole splitting (Δ), (b) center shift (δ) and (c) relative area versus Sn content of the Sn-Si component.

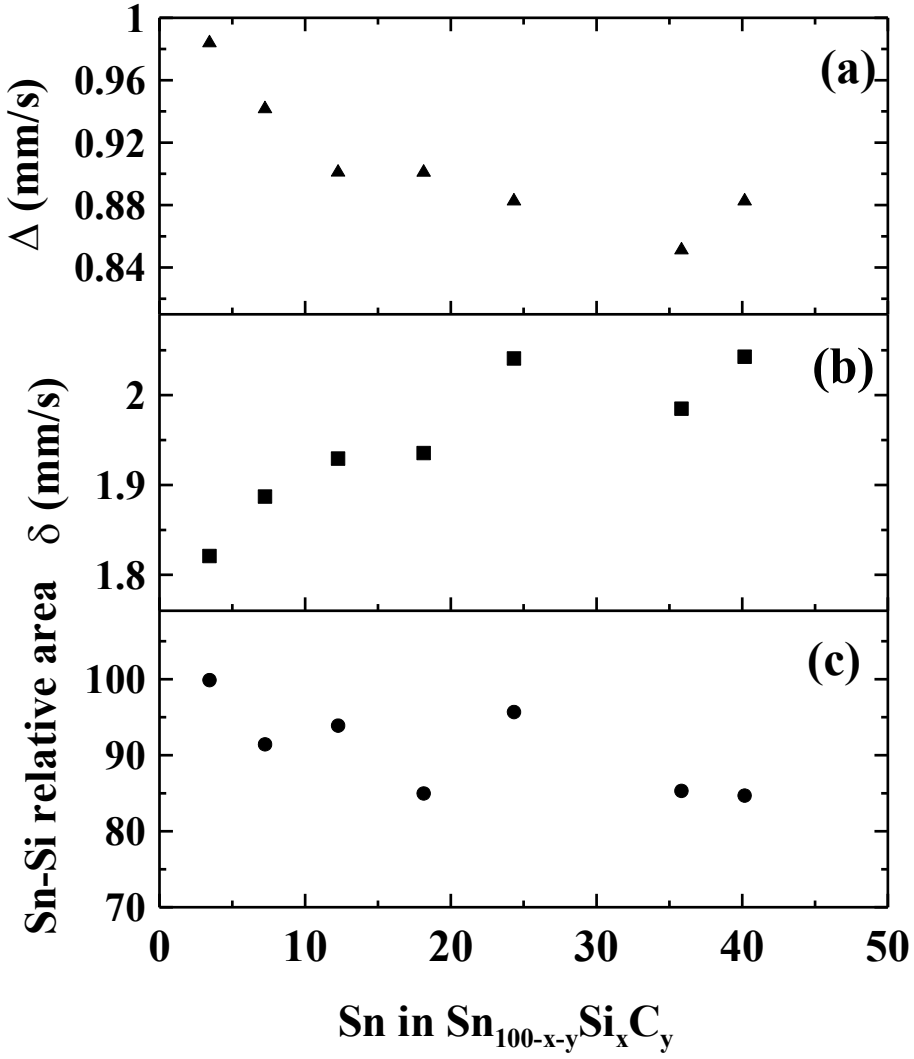

Figure 5.18: Room temperature ^{119}Sn Mössbauer effect parameters of the doublet component for $Sn_{100-x-y}Si_xC_y$ combinatorial Library 3 ($5 < x < 45$ and $y \sim 45$). (a) quadrupole splitting (Δ), (b) center shift (δ),and (c) relative area versus Sn content of Sn-Si component.

5.5 Conclusions

The combination of microprobe, X-ray diffraction, electrochemistry and Mössbauer effect spectroscopy has allowed for a consistent picture of the microstructure and resulting properties of Sn-Si-C alloys. The effects of increasing C content on the behavior as a function of Sn:Si ratio are clearly seen in both electrochemical studies and Mössbauer effect spectroscopy investigations. The addition of C is shown to inhibit the aggregation of Sn grains. When large amounts of C and Si are present, the capacity is lower than that expected based on full reaction of Si, Sn and C with Li, suggesting the formation of nanoscale SiC. A range of compositions with amorphous or nanostructured compositions display promising capacity retention during extended cycling. These studies demonstrate that Sn-Si-C alloys show promise as negative electrode materials for Li-ion cells and that the microstructure of the sputtered films can be refined by the choice of appropriate stoichiometry in order to select the appropriate capacity and corresponding overall volume change.

5.6 Anowledgment

M.A.A. acknowledges the financial support of the Royal Commission for Jubail and Yanbu in Kingdom of Saudi Arabia (Yanbu Industrial College).

5.7 References

[1] B. Scrosati and J. Garche, “Lithium batteries: Status, prospects and future”, *J. Power Sources* **195** (2010) 2419-2430.

[2] R. Dell and D. Rand, “Understanding batteries”, Royal Society of Chemistry, Cambridge (2001).

[3] T. Reddy and D. Linden, “Linden's Handbook of Batteries”, McGraw-Hill, New York (2011).

[4] W. van Schalkwijk and B. Scrosati, “Advances in lithium-ion batteries”, Kluwer Academic/Plenum Publishers, New York (2002).

[5] J. Besenhard, “Handbook of Battery Materials”, Wiley-VCH, New York (1999).

[6] M. Al-Maghrabi, N. van der Bosch, R. Sanderson, D. Stevens, R. Dunlap, and J. Dahn, “A new design for a combinatorial electrochemical cell plate and the inherent irreversible capacity of lithiated silicon”, *Electrochemical and Solid-State Letters* **14** (2011) A42-A44.

[7] L. Beaulieu, K. Hewitt, R. Turner, A. Bonakdarpour, A. Abdo, L. Christensen, K. Eberman, L. Krause, and J. Dahn, “The electrochemical reaction of Li with amorphous Si-Sn alloys”, *J. Electrochem. Soc*. **150** (2003) A149-A156.

[8] M. Obrovac and L. Christensen, “Structural changes in silicon anodes during lithium insertion/extraction”, *Electrochemical and Solid-State Letters* **7** (2004) A93-A96.

[9] U. Kasavajjula, C. Wang, and A. Appleby, “Nano-and bulk-silicon-based insertion anodes for lithium-ion secondary cells”, *J. Power Sources* **163** (2007) 1003-1039.

[10] J. Wolfenstine, “Critical grain size for microcracking during lithium insertion”, *J. Power Sources* **79** (1999) 111-113.

[11] M. Winter, and J. Besenhard, “Electrochemical lithiation of tin and tin-based intermetallics and composites”, *Electrochim. Acta*. **45** (1999) 31-50.

[12] M. Obrovac and L. Krause. “Reversible cycling of crystalline silicon powder”, *J. Electrochem. Soc.* **154** (2007) A103-A108.

[13] O. Mao, R. Turner, I. Courtney, B. Fredericksen, M. Buckett, L. Krause, and J. Dahn, “Active/Inactive nanocomposites as anodes for Li−Ion batteries”, *Electrochemical and Solid-State Letters* **2** (1999) 3-5.

[14] T. Hatchard, J. Dahn, S. Trussler, M. Fleischauer, A. Bonakdarpour, J. Mueller-Neuhaus, and K. Hewitt, “The amorphous range in sputtered Si-Al-Sn films”, *Thin Solid Films* **443** (2003) 144-150.

[15] J. Dahn, S. Trussler, T. Hatchard, A. Bonakdarpour, J. Mueller-Neuhaus, K. Hewitt, and M. Fleischauer, “Economical sputtering system to produce large-size composition-spread libraries having linear and orthogonal stoichiometry variations”, *Chemistry of Materials* **14** (2002) 3519-3523.

[16] H. Ahn, Y. Kim, K. Park, and T. Seong, “Use of Sn–Si nanocomposite electrodes for Li rechargeable batteries”, *Chem. Commun*. (2005) 43-45.

[17] L. Beaulieu, T. Hatchard, A. Bonakdarpour, M. Fleischauer, and J. Dahn, “Reaction of Li with alloy thin films studied by in situ AFM”, *J. Electrochem. Soc.* **150** (2003) A1457-A1464.

[18] M. Suzuki, J. Suzuki, K. Sekine, and T. Takamura, “Li insertion/extraction characteristics of a vacuum-deposited Si–Sn two-component film”, *J. Power Sources* **146** (2005) 452-456.

[19] J. Dahn, R. Mar, M. Fleischauer, and M. Obrovac, “The impact of the addition of rare earth elements to $Si_{1-x}Sn_x$ negative electrode materials for Li-ion batteries”, *J. Electrochem. Soc*. **153** (2006) A1211-A1220.

[20] T. Hatchard, M. Obrovac, and J. Dahn, “A comparison of the reactions of the SiSn, SiAg, and SiZn binary systems with Li”, *J. Electrochem. Soc*. **153** (2006) A282-A287.

[21] A. Timmons and J. Dahn, “*In situ* optical observations of particle motion in alloy negative electrodes for Li-ion batteries”, *J. Electrochem. Soc*. **153** (2006) A1206-A1210.

[22] N. Rock and P. Kumta, "Synthesis and characterization of electrochemically active graphite–silicon–tin composite anodes for Li-ion applications", *J. Power Sources* **164** (2007) 829-838.

[23] A. Timmons, A. Todd, S. Mead, G. Carey, R. Sanderson, R. Mar, and J. Dahn, "Studies of Si_{1-x} C_x electrode materials prepared by high-energy mechanical milling and combinatorial sputter deposition", *J. Electrochem. Soc*. **154** (2007) A865-A874.

[24] J. Thorne, R. Sanderson, J. Dahn, R. Dunlap, "Combinatorial study of the Sn–Cu–C system for Li-ion battery negative electrode materials", *J. Electrochem. Soc.* **157** (2010) A1085-A1091.

[25] J. McGraw, M. Fleischauer, J. Dahn, and R. Dunlap, "Mössbauer effect and x-ray diffraction investigation of Si–Fe thin films", *Philos. Mag.* **86** (2006) 5017-5030.

[26] M. Fleischauer, T. Hatchard, G. Rockwell, J. Topple, S. Trussler, S. Jericho, M. Jericho, and J. Dahn, "Design and testing of a 64-channel combinatorial electrochemical cell", *J. Electrochem. Soc*. **150** (2003) A1465-A1469.

[27] V. Cumyn, M. Fleischauer, T. Hatchard, and J. Dahn, "Design and testing of a low-cost multichannel pseudopotentiostat for quantitative combinatorial electrochemical measurements on large electrode arrays", *Electrochemical and Solid-State Letters* **6** (2003) E15-E18.

[28] P. Liao, B. MacDonald, R. Dunlap, and J. Dahn, "Combinatorially prepared $[LiF]_{1-x}F_x$ nanocomposites for positive electrode materials in Li-ion batteries", *Chemistry of Materials* **20** (2007) 454-461.

[29] M. Birkholz, "Thin film analysis", Wiley, Hoboken (2006).

[30] T. Hatchard and J. Dahn, "Study of the electrochemical performance of sputtered Si_{1-x} Sn_x films", *J. Electrochem. Soc.* **151** (2004) A1628-A1635.

[31] I. Courtney, R. Dunlap, and J. Dahn, "*In-situ* ^{119}Sn Mössbauer effect studies of the reaction of lithium with SnO and SnO: 0.25 B_2O_3: 0.25 P_2O_5 glass", *Electrochim. Acta*. **45** (1999) 51-58.

[32] J. Li, A. Smith, R. Sanderson, T. Hatchard, R. Dunlap, and J. Dahn, "*In situ* ^{119}Sn Mossbauer effect study of the reaction of lithium with Si using a Sn probe*", J. Electrochem. Soc*. (2009) A283-290.

Chapter 6:

Mössbauer Effect Studies of Fe-C Combinatorially Sputtered Thin Films[1]

M. A. Al-Maghrabi, R. J. Sanderson and R. A. Dunlap

6.1 Abstract

Alloys of $Fe_{1-x}C_x$ were produced using combinatorial sputtering methods. The composition of the films as a function of position was determined using electron microprobe techniques and the results have shown that a composition range of about $0.35 < x < 0.75$ was obtained. X-ray diffraction methods were employed to study the structure of the thin films and showed that all portions of the films were amorphous or nanostructured. Room temperature ^{57}Fe Mössbauer spectroscopy was utilized to study the atomic environment around the Fe atoms. Hyperfine field distributions of ferromagnetic alloys as extracted from the Mössbauer analysis suggested the existence of two classes of Fe sites: (1) classes of Fe sites that have primarily Fe neighbors corresponding to a high-field component in the distribution and (2) classes of Fe sites that have a greater number of C neighbors, corresponding to a low-field component. The magnetic splitting decreased as a function of increasing C concentration and alloys with x greater than about 0.68 were primarily paramagnetic in nature. These spectra exhibited distributions of quadrupole splitting with mean splitting in excess of 1.0 mm/s. This indicates a higher degree of local asymmetry around the Fe sites than has typically been seen in other Fe-metalloid systems.

[1]This chapter was published in Philosophical Magazine 93 (2013) 3278-3290.

6.2 Introduction

A number of different ternary alloys that contain both Fe and C have been investigated [1-4] with the aim of developing improved materials for negative electrodes in lithium ion batteries. Studies have shown the best properties for practical battery applications are obtained for materials that are amorphous or nanocrystalline and this imposes some limitations on the ability of experimental techniques, such as x-ray diffraction, to fully characterize these materials. Mössbauer spectroscopy is a unique tool that can be used for identification of local atomic structure and has made important contributions to the understanding of battery electrode materials (e.g. [5]). We have recently undertaken a number of investigations of ternary Fe-C based systems for possible application as Li-ion anode materials. These investigations have included ^{57}Fe Mössbauer effect studies.

While the details of the Mössbauer spectra of a considerable number of sputtered Fe binary alloys have been reported over a wide range of compositions (e.g. see references [6,7] related to Fe-Si) there are far fewer detailed studies of the Fe-C system, particularly in the C-rich region. A study on a limited range of C concentration in $Fe_{1-x}C_x$ binary alloys was reported by Bauer-Grosse et al. [8] and the effect of heat treatment on the formation of some carbides was discussed in reference [9]. To our knowledge there have been no Mössbauer effect studies of Fe-C in the C-rich portion of the phase diagram. The present investigation has been motivated by the need for an understanding of the Mössbauer parameters of C-rich Fe-C alloys for the purpose of better interpreting results for Fe-C containing ternary alloy studies.

6.3 Experimental Methods

A binary combinatorial library of Fe-C binary was produced using a Corona Vacuum Coater model V-3T multi-target magnetron sputtering system described in [10]. A base pressure of 3.1×10^{-7} Torr was achieved and moisture was eliminated from the chamber using a Polycold PFC-400 cryopump. The chamber pressure was maintained at 1 mTorr of argon gas during the deposition. The angular velocity of the sputtering table was 14 rpm to ensure atomic level mixing. Continuous films on the 76 mm wide sputter track were deposited at room temperature on a variety of substrates: a Cu coated glass slide for composition analysis, a Si (100) wafer for x-ray diffraction measurement, and kapton foils for Mössbauer measurement. Two different targets were used: An Fe target was produced by stacking two 50 mm diameter disks cut from a grade 1008 low C steel and a 50.8 mm diameter C target (99.999% pure) obtained from Kurt J. Lesker Company. The desired deposition profile was achieved by using different stationary masks placed over the targets. The two masks were designed to obtain (1) a constant amount of C throughout the library, and (2) a linearly varying amount of Fe. The target composition range was the C-rich half of the phase diagram. The film thickness was determined using profilometer and was ranged from 500 to 600 nm.

Thin film library composition was determined using a JEOL-8200 Superprobe electron microprobe using wavelength dispersive spectroscopy (WDS). The microprobe was equipped with a translation stage, which allowed the composition measurements to be matched with the results of other measurements. A Bruker D-8 Discover diffractometer equipped with a Vantec-2000 area detector and a Cu target x-ray tube was used for the x-ray diffraction measurements.

Room temperature ^{57}Fe Mössbauer effect spectra were collected using resonant gamma-ray system spectrometer (Model W302 from SEE Co.) equipped with a $\underline{Rh}^{57}Co$ source. The spectrometer was calibrated relative to room temperature α-Fe. A Pb aperture was used to select the part of the film to be investigated. The width of

the aperture yielded an uncertainty in Fe and C composition of less than ±1.0 at% in the Fe-rich and about ± 3.0 at% in C-rich portion for the Mössbauer measurements.

6.4 Results and Discussion

6.4.1 Compositional and X-ray Diffraction Studies

Compositions as obtained from microprobe analysis were confirmed by "library closure" [11] as illustrated in Figure 6.1. In this figure the composition and mass per unit area of the sputtered library are plotted as a function of position along the sputtering track. Figure 6.1(a) shows calculated moles per unit area of C (open diamond), and Fe (solid triangle), as defined by “constant” and “linear in” sputtering masks, respectively. The geometry of the “constant” and “linear in” masks are shown in [10]. Figure 6.1(b) shows that the compositions as obtained from the molar ratios in Figure 1(a) agree with the compositions measured by wavelength dispersive spectroscopy. Figure 6.1(c) compares the measured mass of the sputtered films on each weigh disk (open circles) with the mass calculated from the sum of the molar curves in Figure 6.1(a) (solid line) for the composition $Fe_{1-x}C_x$. In general, the films were shiny, except for those parts with large C concentration. Microprobe analysis shows that the oxygen concentration was less than 3.0 at% across the film.

Figure 6.2 shows the x-ray diffraction patterns obtained from the sputtered film for selected compositions. Generally, these spectra are typical for an amorphous or nanostructured material and no sharp peaks indicative of any crystalline phases were observed. As the Fe concentration increased across the library, a small broad peak around 44^o is observed which may be attributed to an increase in regions with a large number of Fe-Fe correlated near neighbors.

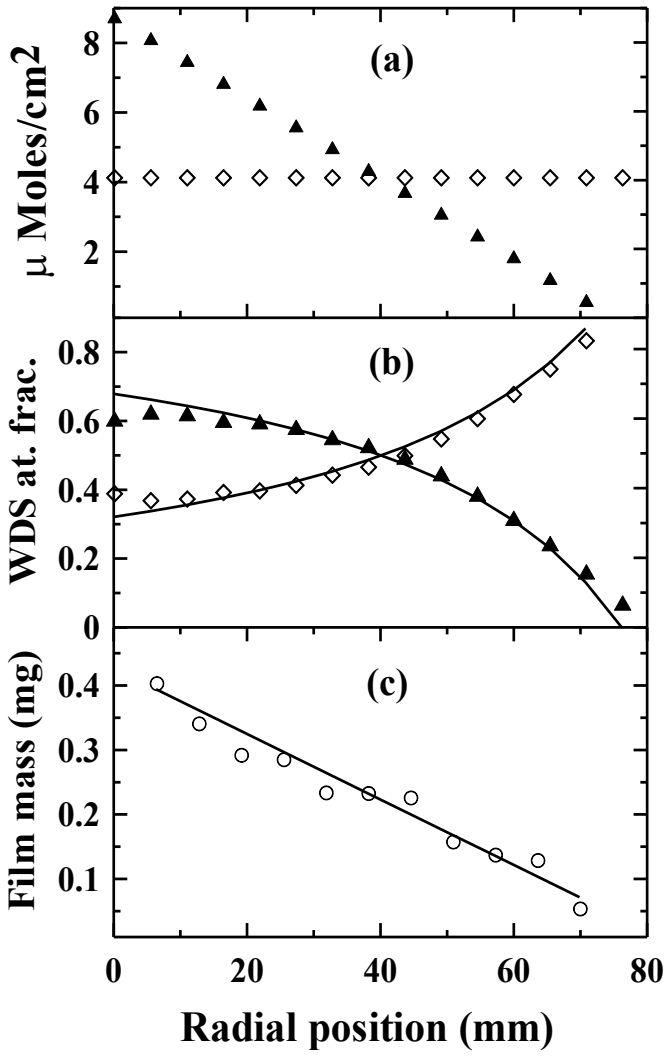

Figure 6.1: A typical "library closure". (a) The moles per unit area of C (open diamonds) and Fe (solid triangles) defined by "constant" and "linear in" sputtering masks, respectively, (b) Composition calculated from (a) (solid lines) are shown to agree well with and the measured compositions from wavelength dispersive spectroscopy (WDS) (data points as above), and (c) The measured mass of the sputtered films on each weighing disk (open circles) and that calculated from the curves in (a) (solid line) for the $Fe_{1-x}C_x$ library.

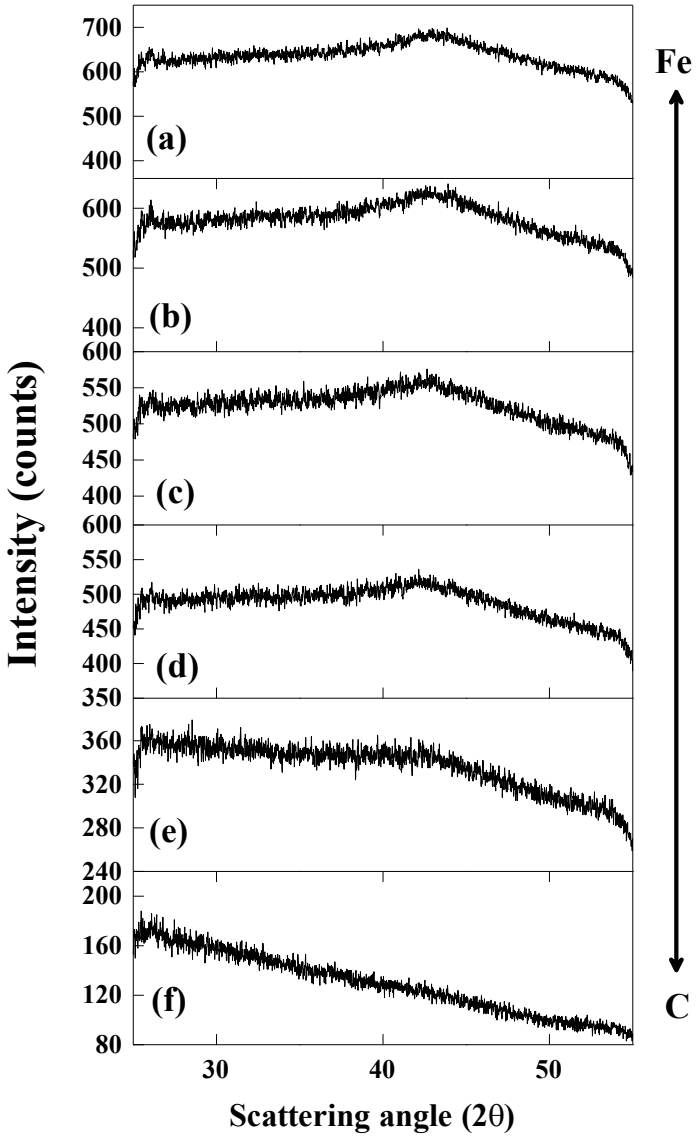

Figure 6.2: Room temperature Cu-K_α x-ray diffraction patterns of $Fe_{1-x}C_x$ with: (a) x = 0.37, (b) x = 0.41, (c) x = 0.46, (d) x = 0.59, (e) x = 0.67and (f) x = 0.75.

6.4.2 Mössbauer Studies

Figure 6.3 shows the Mössbauer spectra obtained for various compositions for the sputtered Fe-C film. As these samples were amorphous or nanostructured, (as evident by XRD patterns), the Mössbauer effect line width was observed to be broader than the intrinsic spectrometer line width of 0.12 mm/s (HWHM). Another reason could potentially lead to such broadening in the line width is the variation in composition of each sample; however these compositional variation was more remarkable in the C-rich samples. Thus, Mössbauer spectra were fit to a Voigt-based function (VBF), as described in [12]. Figure 6.3 shows the fitted components as discussed below for the various compositions, as well as the total fit. On the basis of an inspection of the spectral features, a goodness of fit analysis and expectations concerning the magnetic state of these alloys, spectra were fit to combinations of components as follows: in Figure 6.3, spectra (a) to (e) ($0.35 \leq x \leq 0.47$ in $Fe_{1-x}C_x$) were fit to a distribution of a sextets consisting of two Gaussian components, spectrum (f) ($x = 0.59$) was fit to a doublet and a sextet, both consisting of one Gaussian component, and spectra (g) and (h) ($0.68 \leq x \leq 0.75$) were fit to two distributions of symmetric doublets. In the case of magnetic components, the hyperfine field distribution was linearly correlated to a center shift distribution as is typically the case for amorphous ferromagnets in order to account for their small spectral asymmetry [6]. For all spectra the inclusion of additional magnetic components or quadrupole split components did not meaningfully improve the goodness of fit. Table 6.1 summarizes the fitted parameters obtained from the analysis of the spectra (a) to (e) from Figure 6.3.

The hyperfine field distributions as extracted from the Mössbauer for spectra (a) to (e) from Figure 6.3 are illustrated in Figure 6.4. These distributions illustrate that the field distribution is bimodal and the distinction between these components becomes more apparent with increasing C concentration. A comparison of these distributions clearly shows a decrease in the amplitude of the high field peak relative to the low field peak. As well, the low field peak becomes more clearly

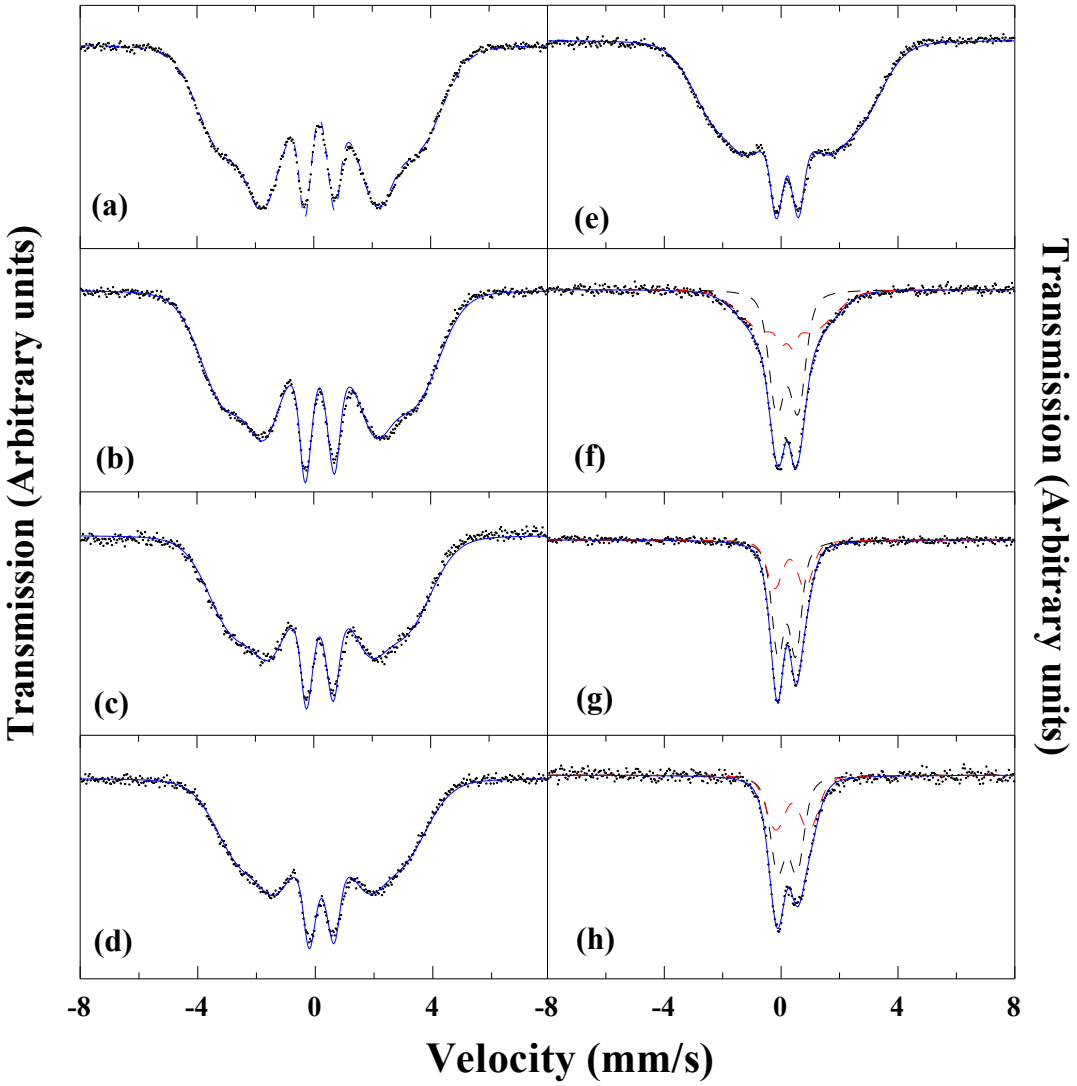

Figure 6.3: Room temperature ^{57}Fe Mössbauer effect spectra of $Fe_{1-x}C_x$ with: (a) x = 0.35, (b) x = 0.37, (c) x = 0.39, (d) x = 0.42, (e) x = 0.47, (f) x= 0.59, (g) x = 0.68, and (h) x = 0.75. Solid lines in spectra (a) to (e) are fits to a distribution of sextets, spectrum (f) is fit to a distribution of doublets and sextets, and spectra (g) and (h) are fit to a distribution of doublets, as discussed in the text.

Table 6.1: Summary of hyperfine parameters obtained from the analysis as described in the text of spectra (a) to (e) shown in Figure 6.3 of sputtered $Fe_{1-x}C_x$ alloys at room temperature. $\langle\delta\rangle$ and $\langle H\rangle$ are the mean center shift and hyperfine field, respectively, and $\langle H_i \rangle$ are the mean fields of the two individual components. Typical uncertainties in fitted parameters are ±0.005 mm/s for velocities and ± 2 T for hyperfine fields.

x	$\langle\delta\rangle$ (mm/s)	$\langle H_1\rangle$ (T)	$\langle H_2\rangle$ (T)	$\langle H\rangle$ (T)
0.35	+0.19	21.1	12.4	18.6
0.37	+0.19	20.1	9.8	17.8
0.39	+0.20	18	6.3	16.1
0.42	+0.21	16.5	5.3	14.5
0.47	+0.21	14.6	4.6	12.6

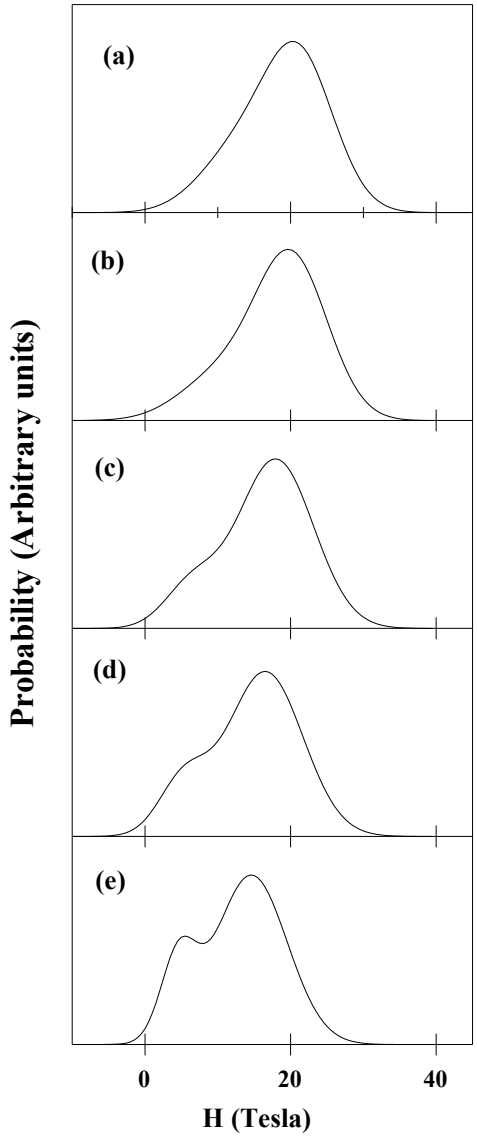

Figure 6.4: Room temperature hyperfine field distributions as obtained from a fit to two Gaussian components for $Fe_{1-x}C_x$ with: (a) $x = 0.35$, (b) $x = 0.37$, (c) $x = 0.39$, (d) $x = 0.42$, and (e) $x = 0.47$.

defined for C-rich compositions. These features suggest the existence of the Fe atoms in two reasonably distinct classes of sites corresponding to Fe atoms with more or fewer C near neighbors. This distinction between high-Fe neighbor sites and low-Fe neighbor sites and the corresponding bimodality of the resulting hyperfine field distribution has been observed in other ferromagnetic Fe-containing binary alloys prepared by non-equilibrium processing methods [6,9,13,14]. The mean hyperfine field for spectra (a) through (e) from Figure 6.3 as obtained from this Voigt-based analysis is shown as a function of C concentration in Figure 6.5. As the mean number of non-magnetic near neighbors (C) increases across the film, the transferred field at Fe sites will be reduced. Thus, the observed decrease in the mean room temperature Fe hyperfine field follows from dilution of the net Fe magnetic moments as the C concentration of the film increases. Observed hyperfine field distributions are in reasonable agreement with those reported by Bauer-Grosse and Le Caër [9] for the common range of compositions in $Fe_{1-x}C_x$. The agreement is within the uncertainties in the compositions and hyperfine field values and may be summarized as follows: (1) Qualitatively, the hyperfine field distributions as illustrated in Figure 6.4 show similar shapes and associated features, such as the growth, in amplitude, of the low-field components as a function of C concentration with those shown in Figure 6.6 of reference [9]. These similarities become more pronounced in the composition range of $0.40 \leq x \leq 0.50$. (2) The hyperfine fields distributions were shifted to lower field values as a function of C concentration although the hyperfine field values of [9] were systematically higher as their measurements were recorded at low temperature. Figure 6.5 also shows the mean center shift (mm/s) relative to α-Fe as a function of C concentration for the ferromagnetic alloys. These values, which are in the range of +0.2 mm/s, are consistent with those reported by Bauer-Grosse et al. [8] for similar compositions.

Spectrum (f) in Figure 6.3 includes both features of a magnetically ordered phase and a paramagnetic phase. This may be due to the distribution of compositions across the portion of film that is included in the Mössbauer spectrum

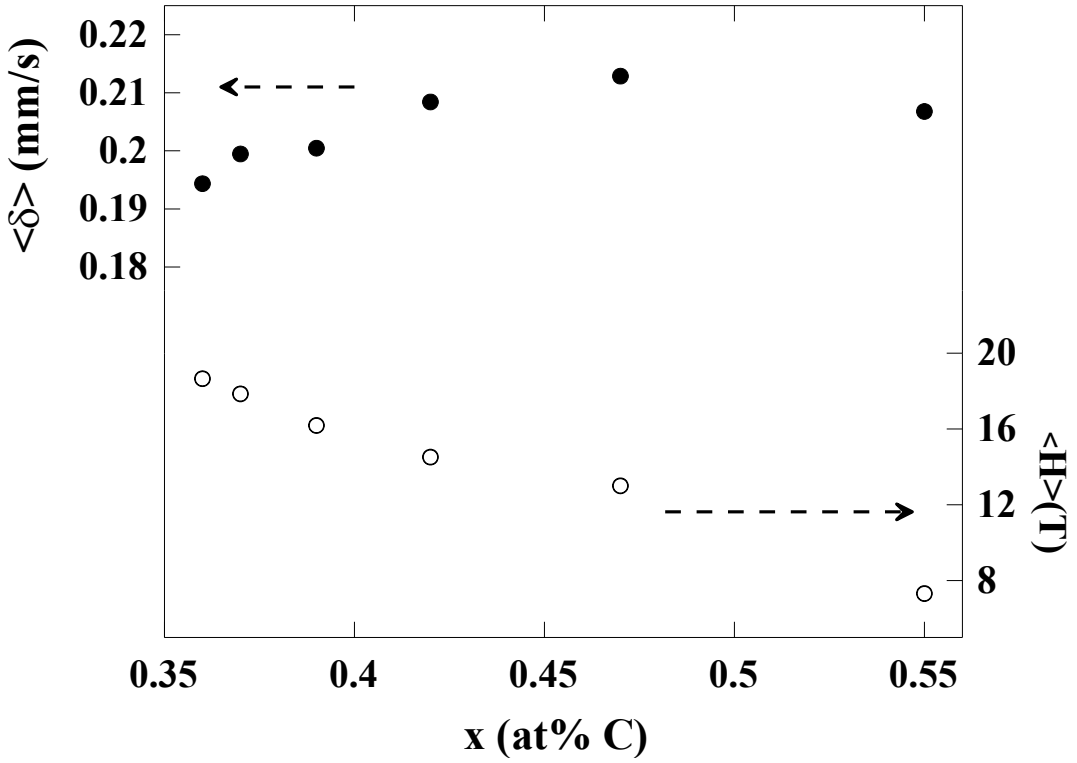

Figure 6.5: Mean center shifts relative to room temperature α-Fe for spectra (a) to (f) from Figure 3 (left) and mean hyperfine fields (right) as a function of x in $Fe_{1-x}C_x$.

or it may be due to a microscopic distribution of environments within the sample or, likely, a combination of both effects. The magnetic component of the spectrum is largely obscured by the paramagnetic component and does not contain enough clear features to extract any detailed information about the field distribution. Thus the ferromagnetic component of this sample was fit to a single Voigt-based distribution and yielded a mean field value of approximately 7 T. The paramagnetic component of this spectrum showed a mean center shift of +0.21 mm/s. The quadrupole distribution was well described by a single Gaussian component with a mean quadrupole splitting of 0.73 mm/s.

Spectra (g) and (h) of Figure 6.3 show no evidence of magnetic splitting and were, therefore, fit to combinations of quadrupole distributions. Reasonable fits require the inclusion of two doublet components as illustrated in Figure 6.3. The mean hyperfine parameters for these two components are summarized in Table 6.2 along with the ratios of the areas of the components.

Table 6.2: Summary of hyperfine parameters obtained from the analysis of spectra (g) and (h) shown in Figure 6.3 of amorphous $Fe_{1-x}C_x$ alloys at room temperature. $\langle\delta_i\rangle$ and $\langle\Delta_i\rangle$ are the mean center shift and mean quadrupole splitting, respectively, of the two sites. A_1/A_2 is the relative area of the two doublets and $\langle\delta\rangle$ and $\langle\Delta\rangle$, are the overall average center shift and quadrupole splitting, respectively. The uncertainties in the velocities are typically ±0.005 mm/s

x	doublet 1		doublet 2		A_1/A_2	$\langle\delta\rangle$ (mm/s)	$\langle\Delta\rangle$ (mm/s)
	$\langle\delta_1\rangle$ (mm/s)	$\langle\Delta_1\rangle$ (mm/s)	$\langle\delta_2\rangle$ (mm/s)	$\langle\Delta_2\rangle$ (mm/s)			
0.68	+0.19	0.61	+0.30	1.03	0.66	+0.23	0.75
0.75	+0.21	0.66	+0.39	1.15	0.58	+0.29	0.87

The presence of two doublets can be attributed to the existence of two classes of Fe sites that give rise to two different quadrupole splitting and the two corresponding values for the center shift. Those components with more positive center shifts correspond to those components which have larger quadrupole splitting. These may be analogous to the bimodal hyperfine field distributions as observed in the ferromagnetic alloys that result from the distribution of C neighbors. The identity of these two spectra components in the context of local C neighbor configurations is discussed in detail below. The value of the quadrupole splitting is larger than those observed in many paramagnetic binary Fe-based amorphous alloys (e.g. Fe-Si or Fe-Al) [6,7] but is similar to those observed in some Fe-Ge alloys [15] and in some C-containing ternary systems [16].

The center shift results obtained here may be understood in the context of a simple model introduced by Miedema and van der Woude [17]. This model considers three contributions to the center shift in amorphous Fe-X alloys; (1) an interatomic electron transfer resulting from the differences in the electronegativities of Fe and X, (2) an s → d electron transfer which tends to equalize electron densities between neighboring Wigner-Seitz cells and (3) a contribution due to differences between the atomic volumes of the two elements. Bauer-Gross and LeCaër [9] have suggested the inclusion of only the first two terms for a description of center shifts in Fe-C alloys. In this case the center shift is expressed as:

$$\delta(x_s) = (1 - x_s)\delta_{\max} \tag{6.1}$$

where the x_s is the surface concentration and is given by:

$$x_s = \frac{(1-x)(V_{Fe})^{2/3}}{(1-x)(V_{Fe})^{2/3} + x(V_C)^{2/3}} \tag{6.2}$$

here x is the C atomic percent and V_{Fe} and V_C are the molar volumes of Fe and C, respectively. This term accounts for differences between the atomic sizes of Fe and C and provides a measure of the effective concentration scaled by the relative areas

of the atomic species on the Wigner-Seitz cell boundary. The relationship between x (in $Fe_{1-x}C_x$) and x_s, as defined in Eq.6.2 is shown in Figure 6.6 for the compositions for which Mössbauer measurements are reported in the present work. δ_{max} in Eq. 6.1, is the center shift of an ^{57}Fe nucleus which is completely surrounded by C atoms and given by reference [17] as:

$$\delta_{\max} = P(\Phi_{Fe} - \Phi_C) + Q(n_{WS}^{Fe} - n_{WS}^{C}) \qquad (6.3)$$

where Φ is the electronegativity and n_{WS} is the electron density in the Wigner-Seitz cell for the two elements. The two terms on the right hand side of Eq. 6.3 correspond to the first two contributions to the center shift as listed above.

In the above, the values of P = - 0.66(7) mm/(smm/s) and Q = +0.26(3) mm/(smm/s) as obtained by Hoving et al. [18] have been used. Values of the electronegativities and the electron densities as tabulated by Miedema et al. [19] and as used here are given for Fe and C in Table 6.3. Calculated values from Eqs.6.1 through 6.3 for the Fe center shift as a function of x_s yields a value for $d\delta(x_s)/dx_s$ (i.e. the slope of the plot of $\delta(x_s)$ versus x_s) of - 0.52 mm/s. Center shift data as obtained here may be considered in the context of these predictions. Figure 6.7 shows a plot of mean center shift as a function of surface concentration x_s. Both data from the present study, as presented in Table 6.2, as well as room temperature data from Bauer-Gross and LeCaër [9], are plotted to display the results over an extended range of compositions. Data from Bauer-Gross and LeCaër [9] exhibit a fairly linear region for the Fe-rich compositions (large x_s values), followed by a relatively constant region for smaller Fe-concentrations. They have fit the high Fe linear region to obtain a slope, $d\delta(x_s)/dx_s$ = - 1.27 mm/s, that is not consistent with Miedema and van der Woude [17]. Our data show a fairly constant region corresponding to the constant region from reference [9] followed by an increase for low Fe-concentrations. This region for small x_s has been fit to a linear relationship for $\delta(x_s)$ yielding a value of $d\delta(x_s)/dx_s$= - 0.45 mm/s, in good agreement with the predicted value based on the Miedema and van der Woude model [17].

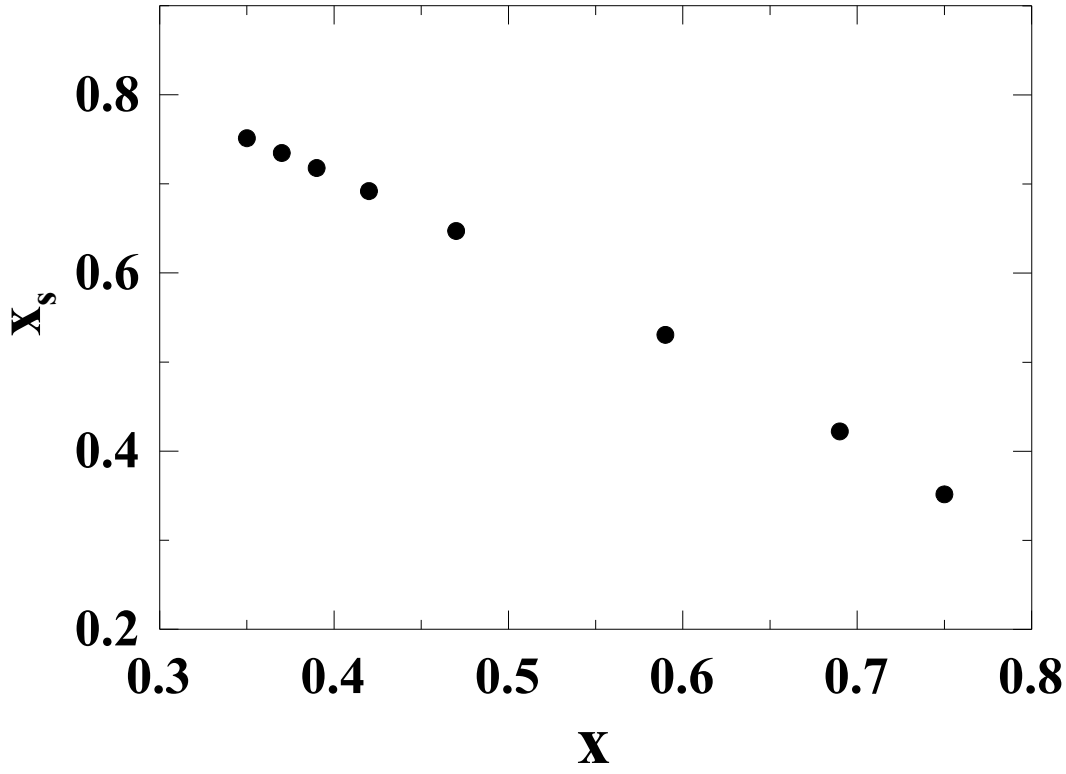

Figure 6.6: Relationship between the surface concentration, x_s, and the value of x from the composition $Fe_{1-x}C_x$ for the compositions studied by Mössbauer spectroscopy. Note that when the composition is written as $Fe_{1-x}C_x$, the higher values of x_s correspond to more Fe-rich compositions.

Table 6.3: Parameters for the mean center shift calculation from reference [17]. One density unit d.u. = 4.7×10^{22} electrons/cm^3.

element	Φ (V)	n_{ws} (d.u.)
Fe	4.93	5.55
C	6.2	6.86

It can be noted that the fitted line extrapolates to $\delta(x_s) = 0$ mm/s at $x_s = 1$, as appropriate for pure Fe at room temperature.

Hoving et al. [18] have applied this model with the inclusion of the volume mismatch factor to the center shift of $Fe_{1-x}B_x$ alloys as a function of Boron concentration ($0.1 \leq x \leq 0.9$). They observed a trend in the center shift as a function of B concentration that is consistent with the predictions of Miedema and van der Woude [17]. The present investigation shows that similar data for the Fe-C system in the C-rich region can be well described by Miedema and van der Woude [17]. This is the region in which dilute Fe probe atoms become largely surrounded by C atoms, and the region in which the Miedema and van der Woude model with exclusion of the volume mismatch term appears to provide a suitable description of the results.

On the basis of the mean center shift trends as illustrated in Figure 6.7 and the hyperfine parameters as shown in Table 6.2 for the paramagnetic alloys, some insight into the identity of the two components included in the Mössbauer analysis for spectra (g) and (h) of Figure 6.3 can be obtained. Figure 6.7 clearly shows that in the C-rich region the center shift becomes more positive with increasing C content. This suggests that the component listed in Table 7.2 (doublet 2) which has the more positive center shift corresponds to the class of Fe sites which have a greater concentration of C near neighbors. In this respect, the following observations are significant:

(1) Both components show center shifts that become more positive with increasing C content.
(2) The more positive center shift component increases more significantly than the less positive center shift component with increasing C content.
(3) The relative area of the component with the less positive center shift decreases with increasing C content.

These observations are consistent with a situation where both more and less C-rich environments exist giving rise to the existence of two doublet components and

as the overall C-content of the alloy increases both environments increase in average C near neighbor concentration but the more C-rich environments increase more significantly both in C-coordination and frequency of occurrence.

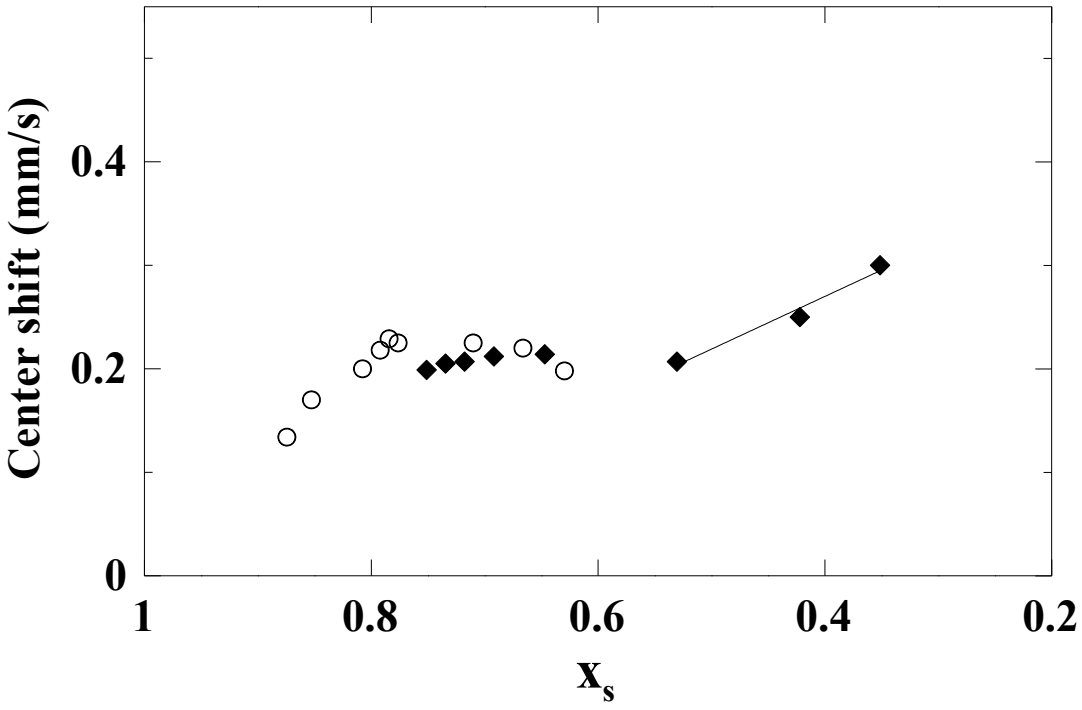

Figure 6.7: Mean center shift (mm/s) as a function of surface concentration x_s in $Fe_{1-x}C_x$. Solid diamonds represent experimental data from the current work, and circles correspond to the room temperature experimental data reported by Bauer-Grosse and LeCaër [9]. The solid line is a linear fit to the data in the high C region.

6.5 Conclusions

The current work presents room temperature ^{57}Fe Mössbauer effect studies of amorphous $Fe_{1-x}C_x$ alloys prepared by combinatorial sputtering. These measurements cover a wide range of compositions and extend the ranges reported in the literature to much more C-rich compositions. Alloys with larger Fe concentrations show ferromagnetic behavior with Mössbauer spectra that are consistent with previous results in the literature. These alloys exhibit mean hyperfine fields that decrease with increasing C content. Hyperfine field distributions show the existence of two distinct Fe environments corresponding to local Fe coordination with more or fewer C near neighbors. Alloys with a higher C-content show purely paramagnetic behavior at room temperature. Mean center shifts are well described by the model of Miedema and van der Woude [17] which describes the composition dependence of the center shift in terms of the electronegativity differences between Fe and C. This model agrees quantitatively with the experimental results reported here in the region of dilute Fe atoms in a C matrix. C-rich alloys show Mössbauer spectra with mean quadrupole splittings in excess of 1.0 mm/s. This is in contrast with results for similar systems such as Fe-Si [7] and indicates that the presence of C introduces local Fe environments with a more significant asymmetry.

The present results have extended the literature on Mössbauer studies in amorphous Fe-C alloys to the C-rich region. These studies have provided considerable insight into the interaction between Fe and C in dilute alloys and are highly beneficial for the analysis and interpretation of Fe Mössbauer investigations of multicomponent amorphous alloys containing Fe and C.

6.6 Acknowledgments

The authors acknowledge funding from NSERC and the support of the Canada Foundation for Innovation, the Atlantic Innovation Fund and other partners that fund the Facilities for Materials Characterization managed by the Institute for Research in Materials. M.A.A. acknowledges the financial support of the Royal Commission for Jubail and Yanbu in Kingdom of Saudi Arabia (Yanbu Industrial College).

Acknowledgment

6.7 References

[1] H. Lee and S. Lee, "Graphite–FeSi alloy composites as anode materials for rechargeable lithium batteries", *J. Power Sources* **112** (2002) 649-654.

[2] H. Dong, X. Ai, and H. Yang, "Carbon/Ba–Fe–Si alloy composite as high capacity anode materials for Li-ion batteries", *Electrochemistry Communications* **5** (2003) 952-957.

[3] H. Dong, R. Feng, X. Ai, Y. Cao, and H. Yang, "Structural and electrochemical characterization of Fe–Si/C composite anodes for Li-ion batteries synthesized by mechanical alloying", *Electrochim Acta.***49** (2004) 5217-5222.

[4] C. Doh, H. Shin, D. Kim, Y. Jeong, S. Moon, B. Jin, H. Kim, K. Kim, D. Oh, and A. Veluchamy, "A new composite anode, Fe–Cu–Si/C for lithium ion battery", *J. Alloys Compounds* **461** (2008) 321-325.

[5] R. Dunlap, O. Mao, and J. Dahn, "Application of *in situ* Mössbauer effect methods for the study of electrochemical reactions in lithium-ion battery electrode materials", *Physical Review B* **59** (1999) 3494-3500.

[6] R. Dunlap, G. Sibley, F. Sy, and T. Hatchard, "Combinatorial material science studies of Fe-rich Fe-Al and Fe-Si thin films", *J. Alloys Compounds* **470** (2009) 27-34.

[7] J. McGraw, M. Fleischauer, J. Dahn, and R. Dunlap, "Mössbauer effect and x-ray diffraction investigation of Si-Fe thin films", *Philos. Mag.* **86** (2006) 5017-5030.

[8] E. Bauer-Grosse, G. Le Caër, and L. Fournes, "Mössbauer study of amorphous and crystallized $Fe_{1-x}C_x$ alloys", *Hyperfine Interactions* **27** (1986) 297-300.

[9] E. Bauer-Grosse and G.l. Caër, "Structural evolution of sputtered amorphous $Fe_{1-x}C_x$ films for $0.19 \leq x \leq 0.49$", Philos. Mag. *B*. **56** (1987) 485-500.

[10] J. Dahn, S. Trussler, T. Hatchard, A. Bonakdarpour, J. Mueller-Neuhaus, K. Hewitt, and M. Fleischauer, "Economical sputtering system to produce large-

size composition-spread libraries having linear and orthogonal stoichiometry variations", *Chemistry of Materials* **14** (2002) 3519-3523.

[11] M. Al-Maghrabi, J. Thorne, R. Sanderson, J. Byers, J. Dahn, and R. Dunlap, "A combinatorial study of the Sn-Si-C system for Li-ion battery applications", *J. Electrochem. Soc*. **159** (2012) A711-A719.

[12] D. Rancourt and J. Ping,"Voigt-based methods for arbitrary-shape static hyperfine parameter distributions in Mössbauer spectroscopy", *Nuclear Instruments and Methods in Physics Research Section B* **58** (1991) 85-97.

[13] R. Dunlap, N. Deschamps, R. Mar, and S. Farrell, "Mössbauer effect studies of $Fe_{100-x}Ga_x$ films prepared by combinatorial methods", *Journal of Physics: Condensed Matter* **18** (2006) 4907.

[14] D. Read, T. Moyo, S. Jassim, R. Dunlap, and G. Hallam, "Hyperfine field distributions and magnetic properties of melt-spun and sputtered Fe-rich Fe-Zr amorphous alloys", *J. Magn Mater*. **82** (1989) 87-93.

[15] H. Hamdeh, M. Al-Hilali, N. Dixon, and L. Fritz, "Mössbauer-spectroscopy study of amorphous Fe-Ge alloys", *Physical Review B* **45** (1992) 2201-2206.

[16] M. Al-Maghrabi, J. Dahn and R. Dunlap, to be published.

[17] A. Miedema and F. Van der Woude, "A cellular atomic model for the Mössbauer isomer shift of ^{197}Au in alloys", *Physica B* **100** (1980) 145-156.

[18] W. Hoving, P. Scholte, P. Dorenbos, G. Fokkema, E. Weits, van der Woude, F, I. Vincze, and K. Buschow, "Packing and chemical effects in amorphous Fe-Zr and Fe-B alloys", *Physical Review B* **32** (1985) 8368-8371.

[19] A. Miedema, P. De Chatel, and F. De Boer, "Cohesion in alloys-fundamentals of a semi-empirical model", *Physica B* **100** (1980) 1-28.

Chapter 7:

Conclusions and Future Work

A large number of different compositions can be produced using the combinatorial sputtering system. The investigation of these samples requires a high throughput electrochemical testing procedure. The first objective of the present work was aimed at testing a durable substrate on which to deposit the electrode materials to be investigated. This goal was successfully accomplished as presented in Chapter 3. The electrochemical performance of sputtered Si was tested using this new design of the electrochemical cell plate and the theoretical capacity of silicon (3578 mAh/g) was achieved successfully. Interestingly, the irreversible capacity was less than 2% of the reversible capacity. These results show clearly that the high reported values of irreversible capacity of Si are not inherent in Si. In addition, the new design of electrochemical cell plates has other advantages, such as that it is economical because it can be produced in bulk and stored until needed, ease in handling during cell assembly being virtually unbreakable, and the possibility of reusability. This new electrochemical cell plate has become the standard experimental device for all such measurements at Dalhousie University and can be a convenient tool for research groups that working on combinatorial sputtering methods.

After successfully developing the new cell plate and testing it on pure Si, other more practical systems for Li-ion battery anodes were investigated. The $Si_{1-x}O_x$ system was considered and this investigation was motivated by the need to understand the role of oxygen on the electrochemical performance of the electrode materials as any large scale production of Si will incorporate some amount of oxygen during production process. The results of this study were presented in

Chapter 4. Samples with different Si:O ratios were amorphous or nanostructured. The electrochemical properties including the first lithiation capacity, reversible capacity (first charge), and irreversible capacity, were consistent with the assumption that as Li is inserted into the material, it ultimately forms Li_4SiO_4 and then reacts with the Si component to form $Li_{15}Si_4$. These interpretations are consistent with the structure of the computed Li-Si-O ternary phase diagram [$Li_{15}Si_4$ is not shown in the equilibrium phase diagram, however]. The irreversible capacities were found to increase as a function of oxygen content. The formation of Li_4SiO_4 may have two advantages (1) it facilitates the lithium diffusion into the nano Si and (2) it mitigates some of the volume expansion resulting from the expansion of Si particles. There was no evidence of structural changes of the materials as the differential capacity plots revealed. The major message of this work is that increasing the oxygen content in $Si_{1-x}O_x$ leads to an increase in irreversible capacity, but the creation of the Li_4SiO_4 inactive phase may help improve cycling by buffering volume change. Thus it is important to optimize the oxygen content in such materials.

As a future approach to more fully understanding the properties of this system, it is suggested that the role of sputtering rate on the structural and electrochemical properties of $Si_{1-x}O_x$ could be investigated. By varying the sputtering rate and the rotational speed of the substrate table, the microstructural properties could be altered, in particular the way in which Si and O mix, hence leading to different grain sizes, and compositions of the phases present in the sputtered film. Another possible approach that might affect the microstructure and consequently the electrochemical performance of these materials is to incorporate C. The incorporation of C will enhance the conductivity, contribute to the overall capacity and result in *in situ* production of inactive matrix that might accommodate some of the induced stress due to lithium insertion.

The high theoretical capacities of Si and Sn are very attractive and producing a negative electrode that contains both elements could yield superior performance.

The addition of C to other active components has been successful in improving electrode performance in the past [1] as it is electrically conductive and provides a suitable matrix for nanostructured active grains to undergo lithiation and de-lithiation with minimal capacity loss. This approach has been applied to the Si-Sn system as presented in Chapter 5. Our study has shown clearly the effect of adding carbon on the structural and electrochemical performance of the Sn-Si system. The formation of SiC in systems that contain both Si and C can adversely affect capacity and there is a clear need to optimize compositions in order to acheive the ideal balance between capacity and capacity retention. This situation is obvious, for example, in Sn containing materials where the formation of a buffer matrix can be beneficial in inhibiting elemental Sn aggregation and consequently increase the amorphous range of these materials. On the other hand, the presence of larger amounts of C simultaneously with Si motivates the formation of inactive nanoscale SiC as evident by the measured capacities. A range of compositions that show an amorphous or nanostructured nature display promising capacity retention during extended cycling. This study demonstrates clearly that Sn-Si-C alloys show promise as negative electrode materials for Li-ion cells and that the microstructure of the sputtered films can be refined by the choice of appropriate stoichiometry in order to select the appropriate capacity and corresponding overall volume change. As alloys of certain compositions show promise for potential commercial cell production, it is suggested that future work could deal with this range of compositions and investigate the possibility of utilizing methods for scaled-up sample production. The aggregation of Sn was evident from the results presented in Chapter 5 and it is well known that fade in such slloys is a result of formation of two-phase regions. Another approach for future work on this system would be to introduce small amounts of Fe. The Si-Fe-Sn-C system is of interest from at least two perspectives; the abundannce of the component elements and the possibility of probing the microstructure using two different Mössbauer probbe elements as has been done for the Fe-Sn system [2].

In Chapter 6, we presented structural studies of $Fe_{1-x}C_x$ alloys using x-ray diffraction method and room temperature ^{57}Fe Mössbauer effect. Our studies extended the literature on Mössbauer studies in amorphous Fe-C alloys to the C-rich region. The x-ray patterns of all samples were amorphous or nanostructured. As expected, samples with larger Fe content show ferromagnetic behavior with Mössbauer results agreeing with the literature. These alloys exhibit mean hyperfine fields that decrease with increasing C content. Hyperfine field distributions show the existence of two distinct Fe environments corresponding to local Fe coordination with more or fewer C near neighbors. Alloys with higher C-content show pure paramagnetic behavior at room temperature. Mean center shifts are well described by the model of Miedema and van der Woude [3] with a composition dependence that is related to the electronegativity differences between Fe and C. This model agrees quantitatively with the experimental results reported here in the region of dilute Fe atoms in a C matrix. C-rich alloys show Mössbauer spectra with mean quadrupole splittings in excess of 1.0 mm/s. This is in contrast with results of similar systems such as Fe-Si [4] which typically show smaller quadrupole splittings and indicates that the presence of C introduces local Fe environments with a more significant asymmetry. Mössbauer study of $Fe_{1-x}C_x$ alloys have provided considerable insight into the interaction between Fe and C in dilute alloys and are highly beneficial for the analysis and interpretation of Fe Mössbauer investigations of multi-component amorphous alloys containing Fe and C.

Future work on the Fe-C system should include detailed electrochemical studies. Now that the microstructure is well understood from Mössbauer spectroscopy, this information will allow for a consistent model of electrochemical capacity on the basis of the formation of active and inactive phases. Preliminary results of electrochemical studies of Fe-C alloys show clear evidence that inclusion of Fe in amorphous C, which has a specific capacity of ~ 900 mAh/g, improved the Coulombic efficiency of the Fe-C alloys and resulted in improved cycleability.

Incorporation of Fe or other transition metals in C may help to improve the cycleability by refining the microstructure with a corresponding improvement in capacity retention. As carbon, iron and a number of other transition elements are cost effective materials, their potential commercial application is of interest. Such measurements are underway here at Dalhousie University [5].

As the possibility of scaling-up production methods is always a consideration, the preparation and characterization of samples in the Fe-C system by high energy ball milling methods (for example) will provide insight into the effects of sample preparation techniques on microstructure and electrochemical properties. This also forms part of the ongoing work at Dalhousie University.

A comprehensive combinatorial study of Si-Fe-C (not included in this thesis) was also performed by the present author. Figure 7.1 presents the range of compositions covered in this study. X-ray diffraction methods were employed to study the structure of the thin films and showed that all portions of the films were amorphous or nanostructured. Room temperature ^{57}Fe Mössbauer spectroscopy was utilized to study the atomic environment around the Fe atoms. Analysis of these results benefits greatly from the Fe-C results presented in this thesis and allow for the detailed understanding of the role of carbon in determining the microstructure and capacity of these materials. Cyclic voltammetry measurements were performed to study the behavior of these materials as negative electrodes for Li-ion batteries. Some of these electrodes show a very high specific capacity of 1500 mAh/g and good capacity retention of 1200 mAh/g after 25 cycles.

Through a combined consideration of Mössbauer effect measurements and electrochemical data, it is suggested that alloys are a combination of an inactive Si-Fe and Si-C phases and active Si and C grains. Currently, this work is in the writing stage and is expected to be published in the near future. Si-Fe-C is a promising system for different reasons: (1) from structural point it is an attractive system the entire range of compositions that was studied was amorphous or nanostructured,

which reduces the drawbacks of crystalline negative electrode alloys, (2) the differential capacity plots did not reveal any major structural changes upon cycling, which is an indicator of the stability of the material, and (3) from commercial standpoint, it is a promising system as their components are relatively inexpensive and readily available. Promising compositions, which have good electrochemical performance, were identified through our study and these warrant further investigation using commercial scale production techniques such as ball-milling

Other possible work, which bridges the gap between the work on Si-O and work on Fe-based systems could include an investigation of the Si-O-Fe system. Preliminary investigations along these lines conducted by the author include the preparation of Si-O-Fe thin films by combinatorial sputtering. Figure 7.2 presents the Gibbs triangle showing 64 compositions of the Si-O-Fe system that have been successfully produced. Electrochemical studies and Mössbauer effect measurements on these thin films will clarify the details of the microstructure and phase formation on the existence of active and inactive regions in this system.

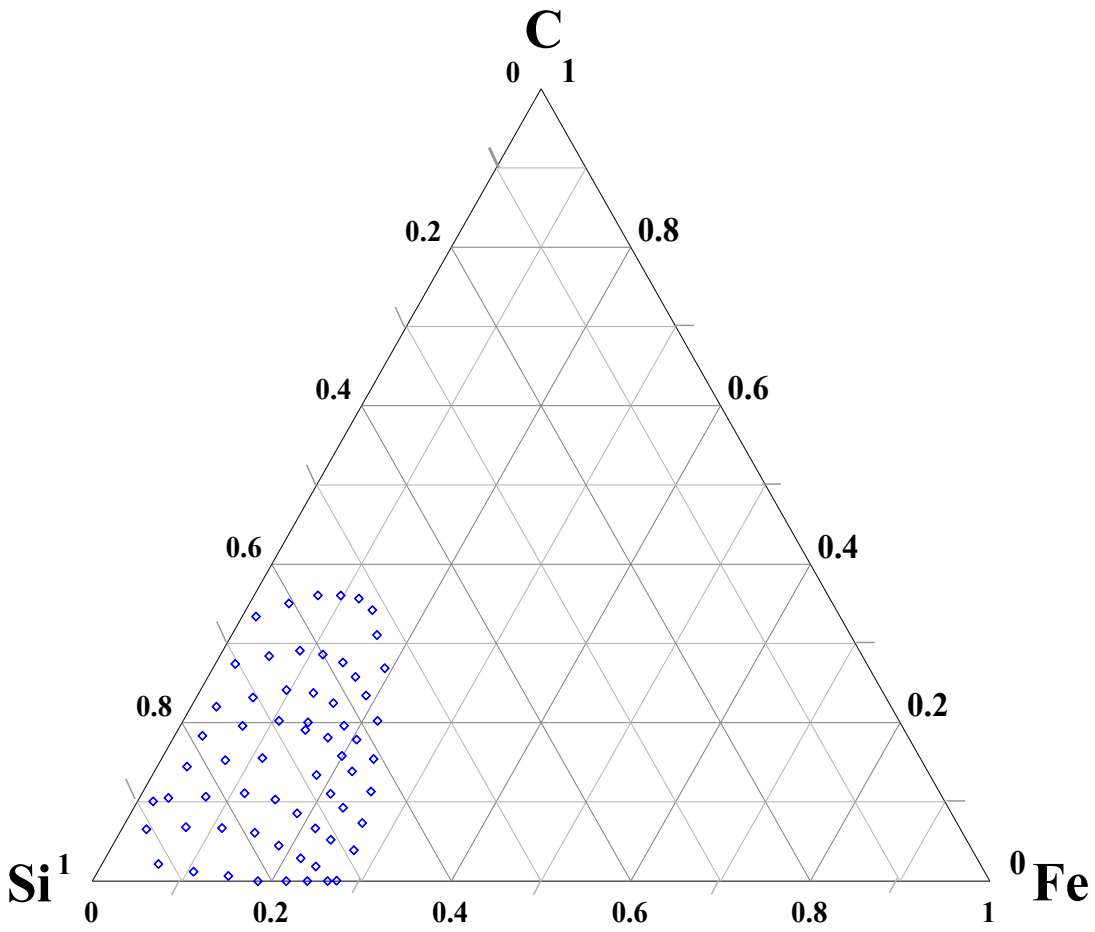

Figure 7.1: Gibbs triangle for the Si-Fe-C system showing range of sputtered compositions as determined by electron microprobe analysis.

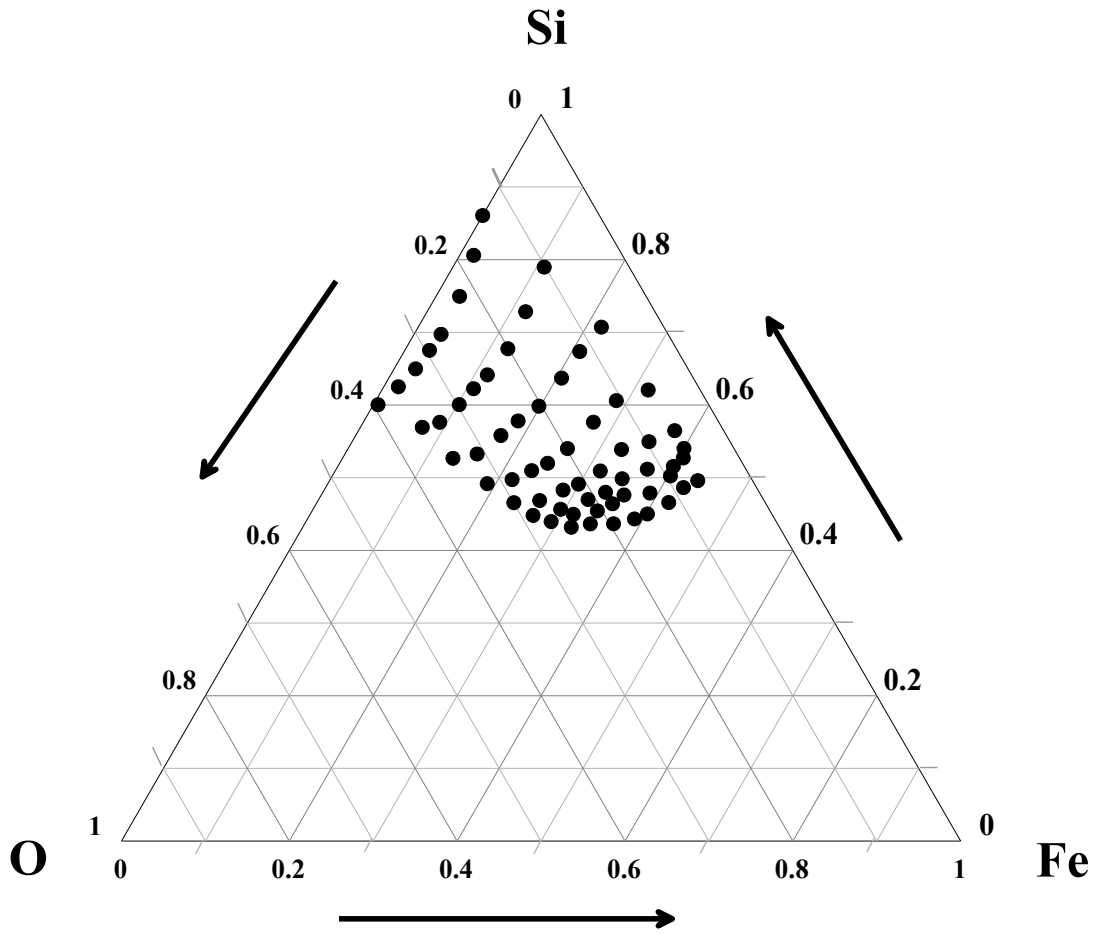

Figure 7.2: Gibbs triangle for the Si-Fe-O system showing range of sputtered compositions as determined by electron microprobe analysis.

7.1 References

[1] J. Thorne, R. Sanderson, J. Dahn, and R. Dunlap, “Combinatorial study of the Sn-Cu-C system for Li-ion battery negative electrode materials”, *J. Electrochem. Soc*. **157** (2010) A1085-A1091.

[2] R.A. Dunlap, O. Mao and J.R. Dahn"Application of in situ Mössbauer effect methods for the study of electrochemical reactions in lithium ion battery electrode materials", Phys. Rev. B **59** (1999) 3494-3500.

[3] A. Miedema and F. Van der Woude, “A cellular atomic model for the Mössbauer isomer shift of ^{197}Au in alloys”, *Physica B* **100** (1980) 145-156.

[4] J. McGraw, M. Fleischauer, J. Dahn, and R. Dunlap, “Mössbauer effect and x-ray diffraction investigation of Si-Fe thin films”, *Philos. Mag.* **86** (2006) 5017-5030.

[5] X. Zhao, Y. Yao, M. Obrovac and R. Dunlap, to be published

References

H. Ahn, Y. Kim, K. Park, and T. Seong, "Use of Sn–Si nanocomposite electrodes for Li rechargeable batteries", *Chem. Commun*. (2005) 43-45.

M. Al-Maghrabi, J. Thorne, R. Sanderson, J. Byers, J. Dahn, and R. Dunlap,"A combinatorial study of the Sn-Si-C system for Li-ion battery applications", *J. Electrochem. Soc.* **159** (2012) A711-A719.

M. Al-Maghrabi, N. van der Bosch, R. Sanderson, D. Stevens, R. Dunlap, and J. Dahn, "A new design for a combinatorial electrochemical cell plate and the inherent irreversible capacity of lithiated silicon", *Electrochemical and Solid-State Letters* **14** (2011) A42-A44.

M. Al-Maghrabi, J. Dahn and R. Dunlap, to be published.

M. Al-Maghrabi, R. Sanderson, and R. Dunlap, "Mössbauer effect studies of Fe–C combinatorially sputtered thin films", *Philos. Mag.* **93** (2013) 3278-3290.

J. Antula and B.F. Becker, "Investigation of the cathodic reduction of lithium and arsenic ions on monocrystalline silicon by cyclic voltammetry", *J. Phys. Chem*. **79** (1975) 2470-2473.

J. Ballon, V. Comparat, and J. Pouxe, "The blade chamber: A solution for curved gaseous detectors", *Nuclear Instruments and Methods in Physics Research* **217** (1983) 213-216.

E. Bauer-Grosse and G. Le Caër, "Structural evolution of sputtered amorphous $Fe_{1-x}C_x$ films for $0.19 \leq x \leq 0.49$", *Philos. Mag. B* **56** (1987) 485-500.

E. Bauer-Grosse, G. Le Caër, and L. Fournes, "Mössbauer study of amorphous and crystallized $Fe_{1-x}C_x$ alloys", *Hyperfine Interactions* **27** (1986) 297-300.

S. Beattie and J. Dahn, "Combinatorial electrodeposition of ternary Cu-Sn-Zn alloys", *J. Electrochem. Soc.* **152** (2005) C542-C548.

L. Beaulieu, K. Eberman, R. Turner, L. Krause, and J. Dahn, "Colossal reversible volume changes in lithium alloys", *Electrochemical and Solid-State Letters* **4** (2001) A137-A140.

L. Beaulieu, T. Hatchard, A. Bonakdarpour, M. Fleischauer, and J. Dahn, "Reaction of Li with alloy thin films studied by *in situ* AFM", *J. Electrochem. Soc*. **150** (2003) A1457-A1464.

L. Beaulieu, K. Hewitt, R. Turner, A. Bonakdarpour, A. Abdo, L. Christensen, K. Eberman, L. Krause, and J. Dahn, "The electrochemical reaction of Li with amorphous Si-Sn alloys", *J. Electrochem. Soc.* **150** (2003) A149-A156.

J. Besenhard and H. Fritz, "Cathodic reduction of graphite in organic solutions of alkali and NR_4 salts", *Journal of Electroanalytical Chemistry and Interfacial Electrochemistry* **53** (1974) 329-333.

J. Besenhard, M. Winter, J. Yang, and W. Biberacher, "Filming mechanism of lithium-carbon anodes in organic and inorganic electrolytes", *J. Power Sources* **54** (1995) 228-231.

J. Besenhard, J. Yang, and M. Winter, "Will advanced lithium-alloy anodes have a chance in lithium-ion batteries?", *J. Power Sources* **68** (1997) 87-90.

J. Besenhard, "Handbook of Battery Materials", Wiley-VCH, New York (1999).

M. Birkholz, "Thin film analysis", Wiley-VCH, Hoboken 2006.

B. Boukamp, G. Lesh, and R. Huggins, "All-solid lithium electrodes with mixed-conductor matrix", *J. Electrochem Soc*. **128** (1981) 725-729.

K. Brandt, "A 65 Ah rechargeable lithium molybdenum disulfide battery", *J. Power Sources* **18** (1986) 117-125.

L. Chen, J. Xie, H. Yu, and T. Wang, "An amorphous Si thin film anode with high capacity and long cycling life for lithium ion batteries", *J. Appl. Electrochem*. **39** (2009) 1157-1162.

M. Cheng and B. Hwang, "Mesoporous carbon-encapsulated NiO nanocomposite negative electrode materials for high-rate Li-ion battery", *J. Power Sources* **195** (2010) 4977-4983.

K. Chopra, "Thin film phenomena", McGraw-Hill, New York (1969).

I. Courtney and J. Dahn, "Electrochemical and *in situ* x-ray diffraction studies of the reaction of lithium with tin oxide composites", *J. Electrochem. Soc*. **144** (1997) 2045-2052.

I. Courtney, R. Dunlap, and J. Dahn, "*In-situ*^{119}Sn Mössbauer effect studies of the reaction of lithium with SnO and SnO: 0.25 B_2O_3: 0.25 P_2O_5 glass", *Electrochim. Acta.* **45** (1999) 51-58.

V. Cumyn, M. Fleischauer, T. Hatchard, and J. Dahn, "Design and testing of a low-cost multichannel pseudopotentiostat for quantitative combinatorial electrochemical measurements on large electrode arrays", *Electrochemical and Solid-State Letters* **6** (2003) E15-E18.

J. Dahn, "Phase diagram of Li_xC_6", *Physical Review B* **44** (1991) 9170-9177.

J. Dahn, R. Mar, M. Fleischauer, and M. Obrovac, "The impact of the addition of rare earth elements to $Si_{1-x}Sn_x$ negative electrode materials for Li-ion batteries", *J. Electrochem. Soc.* **153** (2006) A1211-A1220.

J. Dahn, A. Sleigh, H. Shi, J. Reimers, Q. Zhong, and B. Way, "Dependence of the electrochemical intercalation of lithium in carbons on the crystal structure of the carbon", *Electrochim. Acta.* **38** (1993) 1179-1191.

J. Dahn, S. Trussler, T. Hatchard, A. Bonakdarpour, J. Mueller-Neuhaus, K. Hewitt, and M. Fleischauer, "Economical sputtering system to produce large-size composition-spread libraries having linear and orthogonal stoichiometry variations", *Chemistry of Materials* **14** (2002) 3519-3523.

J. Dahn, T. Zheng, Y. Liu, and J. Xue, "Mechanisms for lithium insertion in carbonaceous materials", *Science* 270 (1995) 590-593.

R. Dell and D. Rand, "Understanding Batteries", Royal Society of Chemistry, Cambridge (2001).

A. Dey, "Electrochemical alloying of lithium in organic electrolytes", *J. Electrochem. Soc.***118** (1971) 1547-1549.

C. Doh, H. Shin, D. Kim, Y. Jeong, S. Moon, B. Jin, H. Kim, K. Kim, D. Oh, and A. Veluchamy, "A new composite anode Fe–Cu–Si/C for lithium ion battery", *J. Alloys Compounds* **461** (2008) 321-325.

H. Dong, X. Ai, and H. Yang, "Carbon/Ba–Fe–Si alloy composite as high capacity anode materials for Li-ion batteries", *Electrochemistry Communications* **5** (2003) 952-957.

H. Dong, R. Feng, X. Ai, Y. Cao, and H. Yang, "Structural and electrochemical characterization of Fe–Si/C composite anodes for Li-ion batteries synthesized by mechanical alloying", *Electrochim. Acta.* **49** (2004) 5217-5222.

R. Dunlap, N. Deschamps, R. Mar, and S. Farrell, "Mössbauer effect studies of $Fe_{100-x}Ga_x$ films prepared by combinatorial methods", *Journal of Physics: Condensed Matter* **18** (2006) 4907-4920.

R. Dunlap, O. Mao, and J. Dahn, "Application of *in situ* Mössbauer effect methods for the study of electrochemical reactions in lithium-ion battery electrode materials", *Physical Review B* **59** (1999) 3494-3500.

R. Dunlap, G. Sibley, F. Sy, and T. Hatchard, "Combinatorial material science studies of Fe-rich Fe-Al and Fe-Si thin films", *J. Alloys Compounds* **470** (2009) 27-34.

M. Fleischauer and J. Dahn, "Combinatorial investigations of the Si-Al-Mn system for Li-ion battery applications", *J. Electrochem. Soc*. **151** (2004) A1216-A1221.

M. Fleischauer, T. Hatchard, A. Bonakdarpour, and J. Dahn, "Combinatorial investigations of advanced L-ion rechargeable battery electrode materials", *Measurement Science and Technology* **16** (2005) 212-220.

M. Fleischauer, T. Hatchard, G. Rockwell, J. Topple, S. Trussler, S. Jericho, M. Jericho, and J. Dahn, "Design and testing of a 64-channel combinatorial electrochemical cell", *J. Electrochem. Soc.* **150** (2003) A1465-A1469.

M. Fleischauer, M. Obrovac, and J. Dahn, "Al-Si thin-film negative electrodes for Li-ion batteries", *J. Electrochem. Soc.* **155** (2008) A851-A854.

M. Fleischauer, M. Obrovac, J. McGraw, R. Dunlap, J. Topple, and J. Dahn, "Al-M (M= Cr, Fe, Mn, Ni) thin-film negative electrode materials", *J. Electrochem. Soc.* **153** (2006) A484-A491.

M. Fleischauer, J. Topple, and J. Dahn, "Combinatorial investigations of Si-M (M= Cr Ni, Fe, Mn) thin film negative electrode materials", *Electrochemical and Solid-State Letters* **8** (2005) A137-A140.

D. Fouchard and J. Taylor, "The molicell rechargeable lithium system: Multicell aspects", *J. Power Sources* **21** (1987) 195-205.

N. Goldenfeld, "Dynamics of dendritic growth", *J. Power Sources* **26** (1989) 121-128.

J. Goldstein, "Scanning Electron Microscopy and X-ray Microanalysis: A text for biologists, materials scientists, and geologists", Plenum Press, New York (1992).

E. Gordon, M. Gallop, and D. Patel, "Strategy and tactics in combinatorial organic synthesis applications to drug discovery", *Acc. Chem. Res*. **29** (1996) 144-154.

J. Graetz, C. Ahn, R. Yazami, and B. Fultz, "Highly reversible lithium storage in nanostructured silicon", *Electrochemical and Solid-State Letters* **6** (2003) A194-A197.

N. Greenwood and T. Gibb, "Mössbauer spectroscopy", Chapman and Hall, London (1971).

A. Guerfi, P. Charest, M. Dontigny, J. Trottier, M. Lagace, P. Hovington, A. Vijh, and K. Zaghib, "SiO_x-graphite as negative for high energy Li-ion batteries", *J. Power Sources* **196** (2011) 5667-5673.

C. Guo, D. Wang, Q. Wang, B. Wang, and T. Liu, "A SiO/graphene nanocomposite as a high stability anode material for lithium-ion batteries", *Int. J. Electrochem. Sci.* **7** (2012) 8745-8752.

H. Hamdeh, M. Al-Hilali, N. Dixon, and L. Fritz, "Mössbauer-spectroscopy study of amorphous Fe-Ge alloys", *Physical Review B* **45** (1992) 2201-2206.

J. Hanak, "The "multiple-sample concept" in materials research: Synthesis, compositional analysis and testing of entire multi-component systems", *J. Mater. Sci.* **5** (1970) 964-971.

T. Hatchard and J. Dahn, "Study of the electrochemical performance of sputtered $Si_{1-x}Sn_x$ films", *J. Electrochem. Soc.* **151** (2004) A1628-A1635.

T. Hatchard and J. Dahn, "*In situ* XRD and electrochemical study of the reaction of lithium with amorphous silicon", *J. Electrochem. Soc*. **151** (2004) A838-A842.

T. Hatchard, J. Dahn, S. Trussler, M. Fleischauer, A. Bonakdarpour, J. Mueller-Neuhaus, and K. Hewitt, "The amorphous range in sputtered Si-Al-Sn films", *Thin Solid Films* **443** (2003) 144-150.

T. Hatchard, M. Obrovac, and J. Dahn, "A comparison of the reactions of the SiSn, SiAg, and SiZn binary systems with Li", *J. Electrochem. Soc*. **153** (2006) A282-A287.

T. Hatchard, M. Obrovac, and J. Dahn, "Electrochemical reaction of the $Si_{1-x}Zn_x$ binary system with Li", *J. Electrochem. Soc*. **152** (2005) A2335-A2344.

T. Hatchard, J. Topple, M. Fleischauer, and J. Dahn, "Electrochemical performance of SiAlSn films prepared by combinatorial sputtering", *Electrochemical and Solid-State Letters* **6** (2003) A129-A132.

A. Hohl, T. Wieder, P. Van Aken, T. Weirich, G. Denninger, M. Vidal, S. Oswald, C. Deneke, J. Mayer, and H. Fuess, "An interface clusters mixture model for the structure of amorphous silicon monoxide (SiO)", *J. Non-Cryst. Solids* **320** (2003) 255-280.

W. Hoving, P. Scholte, P. Dorenbos, G. Fokkema, E. Weits, van der Woude, F, I. Vincze, and K. Buschow, "Packing and chemical effects in amorphous Fe-Zr and Fe-B alloys", *Physical Review B* **32** (1985) 8368-8371.

X. Huang, J. Tu, X. Xia, X. Wang, J. Xiang, L. Zhang, and Y. Zhou, "Morphology effect on the electrochemical performance of NiO films as anodes for lithium ion batteries", *J. Power Sources* **188** (2009) 588-591.

R. Huggins, "Lithium alloy negative electrodes", *J. Power Sources* **81** (1999) 13-19.

R. Huggins, "Materials science principles related to alloys of potential use in rechargeable lithium cells", *J. Power Sources* **26** (1989) 109-120.

R. Huggins, "Symposium on Lithium Batteries", San Diego, CA, (1987).

Y. Hwa, C. Park, and H. Sohn, "Modified SiO as a high performance anode for Li-ion batteries", *J. Power Sources* (2012).

Y. Idota, T. Kubota, A. Matsufuji, Y. Maekawa, and T. Miyasaka, "Tin-based amorphous oxide: A high-capacity lithium-ion-storage material", *Science* **276** (1997) 1395-1397.

A. Jain, G. Hautier, C. Moore, S. Ong, C. Fischer, T. Mueller, K. Persson, and G. Ceder, "A high-throughput infrastructure for density functional theory calculations", *Computational Materials Science* **50** (2011) 2295-2310.

A. Jain, G. Hautier, S. Ong, C. Moore, C. Fischer, K. Persson, and G. Ceder, "Formation enthalpies by mixing GGA and GGA U calculations", *Physical Review B* **84** (2011) 1-10.

R. Jenkins and R. Snyder, "Introduction to x-ray powder diffractometry", Wiley, Hoboken (2012).

G. Jeong, J. Kim, Y. Kim, and Y. Kim, "Multifunctional TiO_2 coating for a SiO anode in Li-ion batteries", *Journal of Materials Chemistry* **22** (2012) 7999-8004.

H. Jung, M. Park, Y. Yoon, G. Kim, and S. Joo, "Amorphous silicon anode for lithium-ion rechargeable batteries", *J. Power Sources* **115** (2003) 346-351.

U. Kasavajjula, C. Wang, and A. Appleby, "Nano-and bulk-silicon-based insertion anodes for lithium-ion secondary cells", *J. Power Sources* **163** (2007) 1003-1039.

K. Kennedy, T. Stefansky, G. Davy, V. Zackay, and E. Parker, "Rapid method for determining Ternary-Alloy phase diagrams", *J. Appl. Phys.* **36** (1965) 3808-3810.

I. Kim, G. Blomgren, and P. Kumta, "Nanostructured Si/TiB_2 composite anodes for Li-ion batteries", *Electrochemical and Solid-State Letters* **6** (2003) A157-A161.

I. Kim, P. Kumta, and G. Blomgren, "Si/TiN nanocomposites novel anode materials for Li-Ion batteries", *Electrochemical and Solid-State Letters* **3** (2000) 493-496.

J. Kim, W. Yoon, K. Yoo, G. Park, C. Lee, Y. Murakami, and D. Shindo, "Charge-discharge properties of surface-modified carbon by resin coating in Li-ion battery", *J. Power Sources* **104** (2002) 175-180.

K. Kim, J. Park, S. Doo, and T. Kim, "Effect of oxidation on Li-ion secondary battery with non-stoichiometric silicon oxide (SiO_x) nanoparticles generated in cold plasma", *Thin Solid Films* **518** (2010) 6547-6549.

K. Lagarec and D. Rancourt, "Recoil-Mössbauer spectral analysis software for windows", University of Ottawa, Ottawa (1998).

F. Laman and K. Brandt, "Effect of discharge current on cycle life of a rechargeable lithium battery", *J. Power Sources* **24** (1988) 195-206.

M. Lazzari and B. Scrosati, "A cyclable lithium organic electrolyte cell based on two intercalation electrodes", *J. Electrochem Soc*. **127** (1980) 773-774.

H. Lee, Y. Kim, M. Hong, and S. Lee, "Carbon-coated $Ni_{20}Si_{80}$ alloy-graphite composite as an anode material for lithium-ion batteries", *J. Power Sources* **141** (2005) 159-162.

H. Lee and S. Lee, "Graphite-FeSi alloy composites as anode materials for rechargeable lithium batteries", *J. Power Sources* **112** (2002) 649-654.

J. Lee and S. Park, "High-performance porous silicon monoxide anodes synthesized via metal-assisted chemical etching", *Nano Energy* **2** (2013) 146-152.

J. Li and J. Dahn, "An *in situ* x-ray diffraction study of the reaction of Li with crystalline Si", *J. Electrochem. Soc*. **154** (2007) A156-A161.

J. Li, A. Smith, R. Sanderson, T. Hatchard, R. Dunlap and J. Dahn, "*In situ* ^{119}Sn Mossbauer effect study of the reaction of lithium with Si using a Sn probe", *J. Electrochem. Soc*. (2009) A283-A287.

T. Li, Y. Cao, X. Ai, and H. Yang, "Cycleable graphite/$FeSi_6$ alloy composite as a high capacity anode material for Li-ion batteries", *J. Power Sources* **184** (2008) 473-476.

P. Liao, B. MacDonald, R. Dunlap, and J. Dahn, "Combinatorially prepared $[LiF]_{1-x}$ Fe_x nanocomposites for positive electrode materials in Li-ion batteries", *Chemistry of Materials* **20** (2007) 454-461.

P. Limthongkul, Y. Jang, N. Dudney, and Y. Chiang, "Electrochemically-driven solid-state amorphization in lithium-silicon alloys and implications for lithium storage", *Acta. Mater.* **51** (2003) 1103-1113.

J. Liu, Y. Li, H. Fan, Z. Zhu, J. Jiang, R. Ding, Y. Hu, and X. Huang, "Iron oxide-based nanotube arrays derived from sacrificial template-accelerated hydrolysis: Large-area design and reversible lithium storage", *Chemistry of Materials* **22** (2009) 212-217.

Y. Liu, Z. Wen, X. Wang, X. Yang, A. Hirano, N. Imanishi, and Y. Takeda, "Improvement of cycling stability of Si anode by mechanochemcial reduction and carbon coating", *J. Power Sources* **189** (2009) 480-484.

X. Lou, D. Deng, J. Lee, and L. Archer, "Thermal formation of mesoporous single-crystal Co_3O_4 nano-needles and their lithium storage properties", *Journal of Materials Chemistry* **18** (2008) 4397-4401.

W. Lu, C. López, N. Liu, J. Vaughey, and A. Jansen, "Overcharge effect on morphology and structure of carbon electrodes for lithium-ion batteries", *J. Electrochem. Soc*. **159** (2012) A566-A570.

M. Mamiya, H. Takei, M. Kikuchi, and C. Uyeda, "Preparation of fine silicon particles from amorphous silicon monoxide by the disproportionation reaction" *J. Cryst Growth* **229** (2001) 457-461.

O. Mao, R. Dunlap, and J. Dahn, "Mechanically alloyed Sn-Fe (-C) powders as anode materials for Li-Ion batteries: I. the Sn_2Fe-C system", *J. Electrochem. Soc.* **146** (1999) 405-413.

O. Mao, R. Turner, I. Courtney, B. Fredericksen, M. Buckett, L. Krause, and J. Dahn, "Active/Inactive nanocomposites as anodes for Li-Ion batteries", *Electrochemical and Solid-State Letters* **2** (1999) 3-5.

J. Maranchi, A. Hepp, and P. Kumta, "High capacity, reversible silicon thin-film anodes for lithium-ion batteries", *Electrochemical and Solid-State Letters* **6** (2003) A198-A201.

T. Massalski, H. Okamoto, P. Subramanian, and L. Kacprzak, "Binary alloy phase diagrams", ASM International, 1990.

J. McGraw, M. Fleischauer, J. Dahn, and R. Dunlap, "Mössbauer effect and x-ray diffraction investigation of Si-Fe thin films", *Philos. Mag.***86** (2006) 5017-5030.

A. Miedema, P. De Chatel, and F. De Boer, "Cohesion in alloys-fundamentals of a semi-empirical model", *Physica B* **100** (1980) 1-28.

A. Miedema, F. Van der Woude, "A cellular atomic model for the Mössbauer isomer shift of ^{197}Au in alloys", *Physica B* **100** (1980) 145-156.

M. Miyachi, H. Yamamoto, and H. Kawai, "Electrochemical properties and chemical structures of metal-doped SiO anodes for Li-ion rechargeable batteries", *J. Electrochem. Soc.* **154** (2007) A376-A380.

D. Murphy, F. Di Salvo, J. Carides, and J. Waszczak, "Topochemical reactions of rutile related structures with lithium", *Mater. Res. Bull*. **13** (1978) 1395-1402.

J. Murray and J. Alderson, "Precision cycling and coulombic efficiency measurements on Li/MoS_2 and Li, Al/FeS cells", *J. Power Sources* **26** (1989) 293-299.

R. Nagai, F. Kita, and M. Yamada, "Development of highly reliable high-capacity batteries for mobile devices and small-to medium-sized batteries for industrial applications", *Energy* **450** (2003) 350-358.

Y. Nagao, H. Sakaguchi, H. Honda, T. Fukunaga, and T. Esaka, "Structural analysis of pure and electrochemically lithiated SiO using neutron elastic scattering", *J. Electrochem. Soc*. **151** (2004) A1572-A1575.

T. Nagaura and K. Tozawa, "Lithium ion rechargeable battery", *Prog. Batteries Solar Cells* **9** (1990) 209-214.

M. Obrovac and L. Christensen, "Structural changes in silicon anodes during lithium insertion/extraction", *Electrochemical and Solid-State Letters* **7** (2004) A93-A96.

M. Obrovac and L. Krause, "Reversible cycling of crystalline silicon powder", *J. Electrochem. Soc.* **154** (2007) A103-A108.

C. Park, W. Choi, Y. Hwa, J. Kim, G. Jeong, and H. Sohn, "Characterizations and electrochemical behaviors of disproportionated SiO and its composite for rechargeable Li-ion batteries", *Journal of Materials Chemistry* **20** (2010) 4854-4860.

Y. Park, H. Bang, S. Oh, Y. Sun, and S. Lee, "Effect of carbon coating on thermal stability of natural graphite spheres used as anode materials in lithium-ion batteries", *J. Power Sources* **190** (2009) 553-557.

P. Patel, I. Kim, and P. Kumta, "Nanocomposites of silicon/titanium carbide synthesized using high-energy mechanical milling for use as anodes in lithium-ion batteries", *Materials Science and Engineering: B* **116** (2005) 347-352.

S. Ping Ong, L. Wang, B. Kang, and G. Ceder, "Li− Fe− P− O_2 phase diagram from first principles calculations", *Chemistry of Materials* **20** (2008) 1798-1807.

P. Poizot, S. Laruelle, S. Grugeon, L. Dupont, and J. Tarascon, "Nano-sized transition-metal oxides as negative-electrode materials for lithium-ion batteries", *Nature* **407** (2000) 496-499.

D. Rancourt and J. Ping, "Voigt-based methods for arbitrary-shape static hyperfine parameter distributions in Mössbauer spectroscopy", *Nuclear Instruments and Methods in Physics* **58** (1991) 85-97.

D. Read, T. Moyo, S. Jassim, R. Dunlap, and G. Hallam, "Hyperfine field distributions and magnetic properties of melt-spun and sputtered Fe-rich Fe-Zr amorphous alloys", *J. Magn. Mater*. **82** (1989) 87-93.

E. Reddington, A. Sapienza, B. Gurau, R. Viswanathan, S. Sarangapani, E. Smotkin, and T. Mallouk, "Combinatorial electrochemistry: A highly parallel, optical screening method for discovery of better electrocatalysts", *Science* **280** (1998) 1735-1737.

T. Reddy, "Linden's Handbook of Batteries", McGraw-Hill, New York (2011).

M. Roberts, A. Spong, G. Vitins, and J. Owen, "High throughput screening of the effect of carbon coating in $LiFePO_4$ electrodes", *J. Electrochem. Soc*. **154** (2007) A921-A928.

N. Rock and P. Kumta, "Synthesis and characterization of electrochemically active graphite-silicon-tin composite anodes for Li-ion applications", *J. Power Sources* **164** (2007) 829-838.

J. Saint, M. Morcrette, D. Larcher, L. Laffont, S. Beattie, J. Pérès, D. Talaga, M. Couzi, and J. Tarascon, "Towards a fundamental understanding of the improved

electrochemical performance of silicon-carbon composites", *Advanced Functional Materials* **17** (2007) 1765-1774.

B. Scrosati and J. Garche, "Lithium batteries: Status, prospects and future", *J. Power Sources* **195** (2010) 2419-2430.

R. Sharma and R. Seefurth, "Thermodynamic properties of the Lithium-Silicon system", *J. Electrochem. Soc*. **123** (1976) 1763-1768.

Q. Si, K. Hanai, N. Imanishi, M. Kubo, A. Hirano, Y. Takeda, and O. Yamamoto, "Highly reversible carbon–nano-silicon composite anodes for lithium rechargeable batteries", *J. Power Sources* **189** (2009) 761-765.

V. Subramanian, T. Karabacak, C. Masarapu, R. Teki, T. Lu, and B. Wei, "Low hydrogen containing amorphous carbon films-Growth and electrochemical properties as lithium battery anodes", *J. Power Sources* **195** (2010) 2044-2049.

M. Suzuki, J. Suzuki, K. Sekine, and T. Takamura, "Li insertion/extraction characteristics of a vacuum-deposited Si-Sn two-component film", *J. Power Sources* **146** (2005) 452-456.

P. Taberna, S. Mitra, P. Poizot, P. Simon, and J. Tarascon, "High rate capabilities Fe_3O_4-based Cu nano-architectured electrodes for lithium-ion battery applications", *Nature Materials* **5** (2006) 567-573.

H. Takezawa, K. Iwamoto, S. Ito, and H. Yoshizawa, "Electrochemical behaviors of nonstoichiometric silicon suboxides (SiO_x) film prepared by reactive evaporation for lithium rechargeable batteries", *J. Power Sources* (2013).

Y. Tang, L. Yang, Z. Qiu, and J. Huang, "Template-free synthesis of mesoporous spinel lithium titanate microspheres and their application in high-rate lithium ion batteries*", Journal of Materials Chemistry* **19** (2009) 5980-5984.

L. Thompson and J. Ellman, "Synthesis and applications of small molecule libraries", *Chem. Rev*. **96** (1996) 555-600.

J. Thorne, R. Sanderson, J. Dahn, and R. Dunlap, "Combinatorial study of the Sn-Cu-C system for Li-ion battery negative electrode materials", *J. Electrochem. Soc.***157** (2010) A1085-A1091.

A. Timmons and J. Dahn, "*In situ* optical observations of particle motion in alloy negative electrodes for Li-ion batteries", *J. Electrochem. Soc*. **153** (2006) A1206-A1210.

A. Timmons, A. Todd, S. Mead, G. Carey, R. Sanderson, R. Mar, and J. Dahn, "Studies of Si_{1-x} C_x electrode materials prepared by high-energy mechanical milling and combinatorial sputter deposition", *J. Electrochem. Soc.***154** (2007) A865-A874.

A. Todd, R. Mar, and J. Dahn, "Tin–transition metal-carbon systems for lithium-ion battery negative electrodes", *J. Electrochem. Soc.***154** (2007) A597-A604.

W. van Schalkwijkand and B. Scrosati, "Advances in Lithium-ion Batteries", Kluwer Academic/Plenum Publishers, New York (2002).

U. von Sacken, E. Nodwell, A. Sundher, and J. Dahn, "Comparative thermal stability of carbon intercalation anodes and lithium metal anodes for rechargeable lithium batteries", *J. Power Sources* **54** (1995) 240-245.

J. Vossen and W. Kern, "Thin Film Processes", Academic Press, New York (1978).

M. Wakihara and O. Yamamoto, "Lithium Ion Batteries", John Wiley & Sons, New York (2008).

J. Wang, H. Zhao, J. He, C. Wang, and J. Wang, "Nano-sized SiO_x/C composite anode for lithium ion batteries", *J. Power Sources* **196** (2011) 4811-4815.

C. Wen and R. Huggins, "Chemical diffusion in intermediate phases in the lithium-silicon system", *Journal of Solid State Chemistry* **37** (1981) 271-278.

M. Whittingham, "Electrical energy storage and intercalation chemistry", *Science* **192** (1976) 1126-1127.

D. Wilkinson, H. Blom, K. Brandt, and D. Wainwright, "Effects of physical constraints on Li cycleability", *J. Power Sources* **36** (1991) 517-527.

M. Winter and J. Besenhard, "Electrochemical lithiation of tin and tin-based intermetallics and composites", *Electrochim. Acta*. **45** (1999) 31-50.

J. Wolfenstine, "Critical grain size for microcracking during lithium insertion", *J. Power Sources* **79** (1999) 111-113.

M. Wu and Y. Lin, "Monodispersed macroporous architecture of nickel-oxide film as an anode material for thin-film lithium-ion batteries", *Electrochim. Acta*. **56** (2011) 2068-2073.

X. Xiang, "Combinatorial materials synthesis and screening: An integrated materials chip approach to discovery and optimization of functional materials", *Annual Review of Materials Science* **29** (1999) 149-171.

X. Xiang, X. Sun, G. Briceno, Y. Lou, K. Wang, H. Chang, W. Walla Cefreedman, S. Chen, and P. Schultz, "A combinatorial approach to materials discovery", *Science* **268** (1995) 1738-1740.

M. Yamada, A. Inaba, A. Ueda, K. Matsumoto, T. Iwasaki, and T. Ohzuku, "Reaction mechanism of "SiO"-carbon composite-negative electrode for high-capacity lithium-ion batteries", *J. Electrochem. Soc.* **159** (2012) A1630-A1635.

I. Yanase, T. Ohtaki, and M. Watanabe, "Application of combinatorial process to $LiCo_{1-x}Mn_xO_2$ powder synthesis", *Solid State Ionics* **151** (2002) 189-196.

J. Yang, M. Winter, and J. Besenhard, "Small particle size multiphase-alloy anodes for lithium-ion batteries", *Solid State Ionics* **90** (1996) 281-287.

M. Yoshio, R.J. Brodd, and A. Kozawa, "Lithium-ion Batteries: Science and Technologies", Springer, New York (2009).

B. Yu, J. Lee, J. Song, C. Park, C. Lee, and H. Sohn, "Nanostructured cobalt oxide-based composites for rechargeable Li-ion batteries", *Journal of Solid State Electrochemistry* **16** (2012) 2631-2638.

K. Zaghib, M. Dontigny, A. Guerfi, P. Charest, I. Rodrigues, A. Mauger, and C. Julien, "Safe and fast-charging Li-ion battery with long shelf life for power applications", *J. Power Sources* **196** (2011) 3949-3954.

K. Zaghib, A. Mauger, H. Groult, J. Goodenough, and C. Julien, "Advanced electrodes for high power Li-ion batteries", *Materials* **6** (2013) 1028-1049.

M. Zhang, D. Lei, X. Yin, L. Chen, Q. Li, Y. Wang, and T. Wang, "Magnetite/graphene composites: Microwave irradiation synthesis and enhanced cycling and rate performances for lithium ion batteries", *J.Mater. Chem*. **20** (2010) 5538-5543.

Z. Zhang and P. Ramadass, “Lithium-ion Battery Systems and Technology.Batteries for Sustainability”, Springer, Hoboken (2013).

X. Zhao, Y. Yao, M. Obrovac and R. Dunlap, to be published.

Appendix A: Copyright Releases

The Journal of Electrochemical Society

Request for Permission to Reproduce or Re-Publish ECS Material

Please fax this form to: The Electrochemical Society (ECS), Attn: Permissions Requests, 1.609.730.0629. You may also e-mail your request to: copyright@electrochem.org. Include all the information as required on this form. Please allow 3-7 days for your request to be processed.

I am preparing a (choose one): ☐ paper ☐ chapter ☐ book ☒ thesis
entitled: Structural and Electrochemical Studies on Si-based Materials for Li-ion Batteries Applications

to be published by: Mahdi Al-Maghrabi
in an upcoming publication entitled: Thesis entitled as above

I request permission to use the following material in the publication noted above, and request nonexclusive rights for all subsequent editions and in all foreign language translations for distribution throughout the world.
Description of material to be used—Indicate what material you wish to use (figures, tables, text, etc.) and give the full bibliographic reference for the source publication. You may attach a separate list, organized by ECS title.

1. M. A. Al-Maghrabi et al, *Electrochemical and Solid-State Letters*, 14 (4) A42-A44 (2011).
2. M. A. Al-Maghrabi et al, *Journal of The Electrochemical Society*, 159 (6) A711-A719 (2012)
3. M. A. Al-Maghrabi et al, *Journal of The Electrochemical Society*, 160 (9) A1587-A1593 (2013)

Signature: _____ Date: 17/07/2013

Name: Mahdi Al-Maghrabi
Address:
Department of Physics and Atmospheric Science
Dalhousie University
6310 Coburg Road
Halifax, NS B3H 2J3
CANADA

Telephone: (902) 494-2394 Fax: (902) 494-5191
E-mail: mh297177@dal.ca

Permission is granted to reproduce the above-referenced material. Please acknowledge the author (s) and publication data of the original material, and include the words: "Reproduced by permission of The Electrochemical Society."

July 25, 2013
Date

Ann F. Goedkoop, Director of Publications

Philosophical Magazine